Nonlinear elastic and electrical behaviour in some (II-VI) and (IV-VI) semiconductors

Walker, Nicholas J.

Award date:
1986

Awarding institution:
University of Bath

NONLINEAR ELASTIC AND ELECTRICAL BEHAVIOUR IN SOME (II-VI) AND (IV-VI) SEMICONDUCTORS

submitted by

Nicholas J. Walker

for the degree of PhD
of the University of Bath
1986

Nicholas J Walker

ProQuest LLC
789 East Eisenhower Parkway
P.O. Box 1346
Ann Arbor, MI 48106-1346

ACKNOWLEDGEMENTS

I would like to extend my sincere thanks to my supervisor, Professor G.A. Saunders, for his helpful advice, encouragement, and, on occasions, patience. I would also like to thank all those in the MIRDL division of the GEC Hirst Research Centre, especially M. Hyliandes and G. Jenkin, for their interest and support (both technical and financial) throughout this project.

I am indebted to all the technical staff in the School of Physics, especially Mrs. W.A. Lambson, Mr E.F. Lambson and Mr. Bob (the main man) Draper. I'd also like to thank all my fellow postgrads for many useful discussions and even more useful cups of coffee. I'd like to acknowledge Acorn Computers ltd., Epsom and Computer Concepts Ltd. for their assistance in producing this thesis. Thanks also to Dr. N.J. Cronin, not least for giving me somewhere to live, and to the Ford Motor Co., for providing the transport.

Finally, I'd like to thank my Sister and Brother-in-law, for their enormous support, and occasionally, a slight push in the right direction.

I acknowledge the SERC for the financial support of this project.

For my Mother and Father

ABSTRACT

Linear elasticity and electrical conductivity are, in general, only observed at vanishingly small values of strain and electric field respectively. When dealing with finite values of strain (or large values of electric field), higher terms in the expansion of the stress (conductivity) with respect to the strain (electric field) must then be included.

Nonlinear elasticity is directly related to the *vibrational anharmonicity* in the long wavelength limit. Measurement of the second order elastic constants (SOEC) and third order elastic constants (TOEC) therefore give an insight into the degree of vibrational anharmonicity of the zone centre acoustic phonons (chapter 2). Measurements of the SOEC and TOEC are made using high pressure pulse echo techniques described in chapter 3. The results for the (II-VI) semiconductor cadmium telluride are reported in chapter 4, and are compared with other tetrahedrally coordinated zincblende compounds. A reduction in the two shear moduli, C_{44} and $(C_{11}-C_{12})/2$, with hydrostatic pressure, similar to that seen in other zincblende compounds, is observed in CdTe. Discussion of this *mode softening*, with respect to stability of the zincblende structure is made, and trends in the elastic properties of these materials with Phillips ionicity reported. Use of the elastic and thermal *Gruneisen parameters* are made to further quantify the anharmonicity. The stability of the zincblende structure is also discussed in terms of bond stretching and bond bending force constants, calculated using a

valence force field model.

Similar measurements for the rocksalt structured (IV-VI) semiconductor lead selenide are reported in chapter 5. The soft mode behaviour observed and anharmonicity are quantified in terms of Gruneisen parameters, and are compared with other (IV-VI) compounds. Use of the Born-Meyor potential model is made to estimate the contributions of the nearest neighbour repulsive forces to the Gruneisen parameters.

Chapters 6-8 deal with the measurement of nonlinear current-voltage characteristics in the alloy $Cd_xHg_{1-x}Te$ (CMT), as a function of temperature in the range 2-20K, and alloy composition (x). The nonlinear conductivity observed is due to *hot electron* effects (chapter 6). Chapter 7 describes an automated computer controlled I-V measurement system. Chapter 8 reports the results for three alloys of CMT (x=0.228, 0.245, 0.286). The nonlinear conductivity is discussed in terms of the electron temperature model, and energy relaxation time. Possible application of these alloys to sub-millimetre and far-infrared detection is discussed, and values of the detector voltage responsivity and time response are made using the theory of hot electron bolometers due to Kogan (1963b). These results indicate that CMT may have responsivities comparable to the normally used material, InSb, but with an increased bandwidth.

CONTENTS

"He can compress the most words
into the smallest idea of any
man I've ever met."

- Abraham Lincoln (1809-1865)

CHAPTER 1

GENERAL INTRODUCTION

CHAPTER 1

GENERAL INTRODUCTION.

The work described in this thesis falls into three main areas: nonlinear elastic behaviour in cadmium telluride and other zincblende structured compounds (chapter 4), nonlinear elastic behaviour in lead selenide and other (IV-VI) compounds (chapter 5), and finally nonlinear electrical conductivity in cadmium mercury telluride alloys (chapter 8). Each section of work forms a complete subset of the thesis, and because of this, the respective chapters are so written to enable them to be read seperately. Consequently, they each draw their own conclusions at the end of the chapter. For this reason, no overall conclusion to the thesis is given, and as their is an indepth introduction to each chapter, only a very basic general introduction is now given.

On a macroscopic scale, all physical properties of solids are nonlinear. Linear behaviour tends to exhibit itself only in limiting cases, such as, for example, when dealing with small electric fields or elastic strains. In the case of elasticity, Hooke's law (stress proportional to strain) describes the familiar linear behaviour. However, this is only true in the limit of infinitesimal strains; at finite values of strain, the elastic behaviour deviates from the linear Hooke's law, and the stress is no longer proportional to strain. A similar phenomenon occurs with electrical conductivity; Ohm's law is only strictly valid at low values of electric field

strength. At higher fields, the conductivity becomes field dependent, and the current density is no longer proportional to the electric field. In both these cases, the predicted linear behaviour is due to retaining only the first term of an expansion, and this has important physical consequences for both the elastic and electrical behaviour in solids.

Nonlinear elasticity can be thought of as a change in the elastic constants of a material due to an applied stress. This change is a direct consequence of *vibrational anharmonicity* in the crystal. On a microscopic level, anharmonicity is due to the nonparabolicity of the interatomic potential, and gives rise to such phenomena as thermal expansion. The interatomic force constants (i.e. the coefficients of the expansion of the interatomic potential in terms of distance r about the equilibrium spacing $r=a_o$) are directly related to the elastic constants, which are similarly defined as the coefficients of the expansion of the stress in terms of the strain. More precisely, the elastic constants are defined as the coefficients of the expansion of the strain energy density in terms of the Lagrangian strain parameters (Brugger 1964).

Vibrational anharmonicity and elasticity are dealt with in chapter 2: the definition of the Gruneisen parameter in the quasiharmonic approximation is described, and the link between nonlinear elasticity and vibrational anharmonicity in the long wavelength limit discussed. A brief review of the theory of elasticity is also given, leading to the thermodynamic definition, due to Brugger (1964), of the second order (linear) and third order

(nonlinear) elastic constants (referred to as SOEC and TOEC respectively).

Chapter 3 is concerned with the experimental determination of SOEC and TOEC using high pressure ultrasonic techniques. As well as a description of the techniques used to measure ultrasonic wave velocities as a function of hydrostatic pressure and uniaxial stress, a review of the theory of small amplitude waves in both stressed and unstressed media, leading to the expressions for the pressure derivatives of the velocities in terms of SOEC and TOEC (Thurston and Brugger 1964), is given.

Chapters 4 and 5 are concerned with nonlinear elastic behaviour and the corresponding long wavelength anharmonicity in (II-VI) and (IV-VI) semiconductors respectively. Chapter 4 reports the experimental results for the (II-VI) compound cadmium telluride, and discusses the *soft mode* behaviour and structural stability of this and other tetrahedrally coordinated semiconductors in terms of vibrational anharmonicity. Specifically, trends in these materials with the ionicity as defined by Phillips (1973) are reported, and the mechanism by which they undergo structural phase transitions to the denser, NaCl structure is discussed. A valence force field model (VFF) is used to discuss the stability of the zincblende structure in terms of a bond bend and bond stretch force constants (Keating 1966a,b, Martin 1970 and Gerlich 1973). The anharmonicity is further quantified using the elastic Gruneisen parameters and, together with those Gruneisen parameters calculated from available thermal data, inferences are made concerning the contribution to the low temperature thermal expansion of the transverse

acoustic phonons, close to the Brillouin zone centre, which exhibit mode softening under pressure. Finally, the relevance of these soft modes to the driving mechanism of the first order densification phase transition, which occurs in zinceblende structures, is discussed.

Similar work is reported in chapter 5 for the (IV-VI) semiconductors, with particular relevance to novel data for lead selenide and tin telluride. Again, particular emphasis is placed on the structural stability of these (IV-VI) compounds, and the Gruneisen parameters are used to give a greater insight into their structural stability. The shape of the curves of the mode Gruneisen parameters as a function of crystal orientation of these chalcogenides is compared to that of NaCl, and discussed in terms of the contribution of the nearest neighbour repulsive forces to the long wavelength anharmonicity.

The last three chapters (6-8) are concerned with nonlinear electrical behaviour. In analogy with the elastic constants, it is possible to define the nonlinear conductivity in terms of coefficients in an expansion. These coefficients can be obtained directly from the Boltzmann transport equation (see Seeger 1982). Inclusion of the higher terms in the expansion gives rise to a nonlinear current-voltage characteristic. However, in chapter 6, nonlinear conductivity is discussed in terms of *hot electrons*, and deals qualitatively with the theoretical backround of nonlinear conductivity in semiconductors at liquid helium temperatures. Hot electron effects are due to the electrons gaining energy from the electric field in excess of their mean thermal energy. The degree of nonlinearity is determined by the

dependence on electron energy of the momentum relaxation time (τ_m) and the electron energy loss rate; these dependencies are in turn governed by the electron scattering mechanisms that occur in the semiconductor. A brief summary of the types of scattering that are likely to be of importance are given. The concept and validity of the single electron temperature model is discussed, and using the energy balance equation, the electron energy relaxation time is defined. Finally, chapter 6 deals with the application of hot electron effects to sub-millimetre and far infrared detection, outlining the theory due to Kogan (1963b), in which expressions for the voltage responsivity (R) and time response (τ) based on free carrier absorption are obtained, which are directly related to the nonlinearity of the I-V curve.

Chapter 7 describes the apparatus used to measure the nonlinear current-voltage characteristics in mercury cadmium telluride alloys, as a function of temperature between 2K and 20K, and alloy composition. The results are then presented in chapter 8, and discussed in terms of the single electron temperature model and energy relaxation time. The use of the specific alloy compositions reported as hot electron bolometers for sub-mm and far infrared wavelengths is then discussed, and estimates of the voltage responsivity and time response of such detectors are made using the theory of Kogan (1963b). Finally, a summary of the present work and an outline of possible further work is given.

Although the work presented in this thesis is concerned with many (II-VI), (III-V) and (IV-VI) compounds (especially in the case of the chapters 4 and 5), the

experimental work performed is primarily concerned with CdTe, PbSe and $Cd_xHg_{1-x}Te$. These materials are all technologically important from a point of view of devices for the infrared. In view of this, a brief review of each of these materials is now given.

CdTe, as well as all the (III-VI) and other (II-VI) compounds discussed in chapter 4, has the zincblende structure, and the bonds are consequently tetrahedrally coordinated (sp^3 hybridised). It has a large direct bandgap of 1.605eV, and thus is unsuitable as an intrinsic photoconductor for the infrared, unlike PbSe and $Cd_xHg_{1-x}Te$ (CMT). It is important, however, as a source material for the preparation of CMT, and as a substrate for epitaxially grown CMT devices, as well as many other applications (such as gamma-ray and X-ray spectrometers, electrooptical modulators and solar cells). A review of CdTe is given by Zanio (1978). From a point of view of nonlinear elastic behaviour, it is of interest due to a very high Phillips ionicity (0.717). Phiillips (1973) has pointed out that this puts CdTe very close to the border line between covalent tetrahedrally coordinated structures, and ionic NaCl structure compounds. Thus, examination of the structural stability and vibrational anharmonicity of this material, as compared to other zincblende structured compounds, is well worthwhile.

PbSe, PbTe and PbS are all very closely related (IV-VI) semiconductors, all of which have been used as infrared detectors (Cashman 1959). PbSe and PbTe, with absorption edges near 5um at 77K, were found particular useful in the late 1940s for 3-5μm thermal imaging. More recently,

they have found greater importance when alloyed with tin chalcogenides to give $Pb_xSn_{1-x}Te$ and $Pb_xSn_{1-x}Se$ (referred to as LTT and LTS respectively), both of which have been extensively used as detectors and lasers for the infrared. PbSe has a bandgap of 0.286eV at 4K compared to 0.190eV and 0.165eV for PbTe and PbS respectively (Mitchell *et al* 1964). Even though these compounds have the NaCl structure, work by Littlewood (1980) and Enders (1983, 1984a, 1984b) have shown that they are still predominantly covalent in nature. For this reason, the anharmonicity and corresponding nonlinear elasticity in PbSe and other (II-VI) compounds is of interest.

Of all the semiconductors investigated here, $Cd_xHg_{1-x}Te$ is by far the most technologically important. Two major reviews have been written on the subject (Willardson and Beer 1981, Dornhaus and Nimtz 1976). The alloy was first proposed for an intrinsic infrared detector for the 8-12μm region to work at 77K, to replace the already used InSb, which required cooling to 30K. The main advantage of CMT is that the bandgap can be tailored to any value between that of CdTe (1.6eV) and HgTe (band overlap of -0.2eV) by varying the alloy composition. Because HgTe is a semimetal, a semimetallic to semiconductor transition takes place as the mole fraction of CdTe (x) is increased. The crossover occurs at about x=0.16 at 4.2K. The variation of bandgap with temperature and composition has been measured by many authors (Hanson *et al* 1982, Stankiewicz and Giriat 1972, Scott 1969, Finkman and Nemirovski 1979), all of which report various empirical relationships for the dependence of the gap on T and x; this is mainly due to the various difficulties in experimental techniques used, and the availability of

good consistent material. In this thesis, the relationship due to Hanson *et al* (1982) will be taken, this being the most recent form.

In those alloys having a narrow or near zero gap ($x \sim 0.2$), the band structure is similar to that of InSb. Because of the k.p interaction (Kane 1966), the conduction band is nonparabolic. This gives rise to a very small effective mass, and consequently, very high mobilities ($\sim 10^6 cm^2 V^{-1} s^{-1}$) have been seen in good n-type material at low temperatures, where the conductivity is thought to be dominated by singly ionised impurity scattering (Scott 1972, Long and Schmitt 1970). As the bandgap increases, this nonparabolicity reduces until, at high x values, it vanishes. Hence the mobility also decreases with increasing x.

The measurement of the nonlinear conductivity in CMT alloys was primarily to evaluate their possible use as hot electron bolometers. Putley (1966) has suggested that CMT could be used for detectors for the sub-millimetre and far infrared since it is similar to InSb, the normally used material. Hot electrons have already been observed in CMT at 4.2K (Nimtz *et al* 1974), and hence CMT is considered a good candidate for a more thorough investigation of nonlinear conductivity as a function of temperature and, in this case, alloy composition.

CHAPTER 2

VIBRATIONAL ANHARMONICITY AND ELASTICITY

CHAPTER 2

VIBRATIONAL ANHARMONICITY AND ELASTICITY.

2.1 INTRODUCTION.

All elastic and thermal properties of solids are governed by the nature of the interatomic potential and the crystal structure, since these dictate the vibrational characteristics of the atoms. In a simple lattice dynamical model, the restoring forces between the atoms are generally considered to be proportional to the displacement from their equilibrium positions, which gives rise to harmonic vibrations. By making such an assumption, only the quadratic term in the expansion of the interatomic potential about the equilibrium spacing is considered. This is the harmonic approximation. The most important consequences of the harmonic approximation are:

a) there is no thermal expansion,
b) the elastic constants are independent of temperature and pressure,
c) the heat capacity becomes constant at high temperatures,
d) the specific heats measured at constant volume and constant pressure are equal,
e) their are no phonon-phonon interactions.

Obviously, none of the above features are characteristic of real crystals. Only by inclusion of cubic and higher

terms in the interatomic potential can these phenomena be explained. In other words, they are all due to *anharmonic* effects.

On a more microscopic scale, anharmonicity can be directly related to a change in the phonon spectrum of the crystal, that is a shift in the phonon density of states with a change in temperature and pressure. To quantify exactly the anharmonicity of a solid requires a knowledge of the phonon dispersion curves and the effect of temperature and pressure upon them. It is possible, however, to gain information about the anharmonicity of the long wavelength acoustic modes by studying the elastic properties as a function of applied stress. In this chapter, anharmonicity will be discussed in detail, first by introducing the important concept of the *Gruneisen parameter* via the *quasiharmonic approximation*, and finally by considering nonlinear thermoelastic behaviour which will eventually lead to the definition of second and third order elastic constants.

2.2 THE QUASIHARMONIC APPROXIMATION.

To calculate the dynamical properties of atoms in a crystal, a knowledge of the restoring forces between the atoms is required to obtain the equations of motion. In the harmonic approximation, the expansion of the interatomic potential is terminated in the quadratic term, retaining only the harmonic force constants; this causes the atoms to be treated as a set of independent harmonic oscillators. In this form, it is possible to

obtain exact solutions to the equations of motion, the so-called normal modes of vibration. If cubic and higher terms are included, it becomes impossible to uncouple the motion of the atoms - this is the mathematical basis of phonon-phonon interactions (see Ziman, 1962). The inclusion of the higher terms makes exact solutions to the equations of motion impossible, and approximations have to be employed. For a system that is only slightly anharmonic the *quasiharmonic approximation* is often used. Different definitions of the quasiharmonic approximation have appeared in the literature. Here the definition of Leibfried and Ludwig (1961) will be adopted.

In the quasiharmonic approximation, the frequencies of the phonon modes are considered to depend on temperature and pressure only via a volume change, i.e. through a change in lattice spacing. The interatomic potential is still terminated in the quadratic term, allowing the definition of normal modes as with the harmonic approximation, but now the interatomic force constants are allowed to change with a change in interatomic distance. Hence the phonon density of states will shift with a change in volume, be it due to thermal expansion or an externally applied stress.

2.2.1 The Gruneisen parameter.

The relative change in mode frequency is taken to be directly proportional to the relative change in volume expressible by

$$\frac{\delta\omega(p,q)}{\omega(p,q)} = -\gamma(p,q)\frac{\delta V}{V} \qquad (2.1)$$

where $\gamma(p,q)$ is the constant of proportionality for the mode defined by the branch index p and wave vector q, and is referred to as the *mode Gruneisen parameter*. By rearranging (2.1) the Gruneisen parameter can be defined by the more familiar expression

$$\gamma(p,q) = -\left[\frac{\partial \ln\, \omega(p,q)}{\partial \ln\, V}\right] \quad . \qquad (2.2)$$

A tensorial Gruneisen parameter can be defined by using the strain derivatives of the phonon frequencies:

$$\gamma_{ij}(p,q) = -\left[\frac{\partial \ln\, \omega(p,q)}{\partial \ln\, \eta_{ij}}\right]_{\eta'} \qquad (2.2)$$

where η_{ij} are the Lagrangian strain parameters (see section 2.3.1) and η' refers to keeping all other η_{ij} constant.

The Gruneisen parameter serves to quantify the vibrational anharmonicity. The negative sign in (2.1-3) indicates that a positive Gruneisen parameter infers that the phonon frequencies should normally increase with a

decrease in volume (increase in pressure); this suggests a positive thermal expansion coefficient. A negative $\gamma(p,q)$ is an indication of *soft mode* behaviour, since the mode frequency is becoming smaller with increasing pressure, and may eventually reduce to zero at sufficiently high stress. At this point, the atoms undergo a finite displacement from their original lattice sites, and a phase transition occurs. The relevance of negative Gruneisen parameters and soft modes to structural stability will be discussed in more detail in chapter IV.

Another consequence of a negative Gruneisen parameter is the possibility of negative thermal expansion. In order to see how the Gruneisen parameter relates to thermal expansion, the quasiharmonic equation of state must first be obtained.

2.2.2. The Quasiharmonic Equation of State.

Any equation of state is derived from the thermodynamic relation $P=-(\partial F/\partial V)_T$, where F is the Helmholtz free energy. The free energy of an anharmonic system can be divided into three parts;

$$F = \Phi_{el}(a_0) + F_{vib}(\omega) + F_{anh} \qquad (2.4)$$

where $\Phi_{el}(a_0)$ is the contribution from the static strain; $F_{vib}(\omega)$ contains the kinetic and potential energy terms of the vibrational motion and F_{anh} contains all the terms

which accrue from the cubic and higher terms of the interatomic potential. It should be pointed out that the first two 'harmonic' terms also contain anharmonic contributions through the volume dependencies of the harmonic force constants. In the quasiharmonic approximation F_{anh} is generally ignored and substituting (2.4) into $P=-(\partial F/\partial V)_T$ gives

$$F = -\frac{\partial \Phi_{el}}{\partial V} - \frac{\partial F_{vib}}{\partial V} \quad . \qquad (2.5)$$

From (2.5) the quasiharmonic equation of state can be derived as

$$PV_o = \frac{V-V_o}{\kappa_o} + \sum \gamma(p,q)\bar{E}[\omega_o(p,q)] \qquad (2.6)$$

where κ_o is the bulk compressibility. $\bar{E}[\omega_o(p,q)]$ is the mean energy of the mode $\omega(p,q)$, and $\gamma(p,q)$ is the mode Gruneisen parameter defined by (2.1). The subscript 0 refers to those values at T=0. The first term of (2.6) relates directly to the volume derivative of the static strain contribution, while the second term follows directly from $(\partial F_{vib}/\partial V)$ (see Bruesch 1982).

Apart from employing the quasiharmonic approximation itself, the equation of state (2.6) is further approximated by the assumption that the change in volume $(V-V_o)$ is small. However (2.6) can be simplified still

further by assuming that the mode Gruniesen parameters are equivalent for all modes, i.e. $\gamma(p,q) = \gamma$. (2.6) then becomes

$$PV_o = \frac{V-V_o}{K_o} + \gamma E_{vib}(V_o) \qquad (2.7)$$

where $E_{vib}(V_o)$ is the total vibrational energy at V_o. (2.7) is known as the *Mie-Gruneisen equation of state.* This last assumption is generally not justified, since the mode gammas show marked dispersion with wave vector q.

2.2.3 Thermal Expansion.

The relationship between the Gruneisen parameter and the thermal expansion coefficient can be obtained directly from the equation of state (2.6). To calculate the relative change in volume, $\epsilon = (V-V_o)/V_o$ due to temperature only, the pressure P is set to zero. Hence from (2.6) the thermal expansion is obtained as

$$\epsilon = \frac{K_o}{V_o}\sum\gamma(p,q)\bar{E}[\omega_o(p,q)] \quad . \qquad (2.8)$$

The coefficient of thermal expansion (α) is given by

$(\partial\epsilon/\partial T)_P$. Hence by differentiating (2.8) with respect to T, an expression for α is obtained:

$$\alpha = \frac{\kappa_0}{V_0}\sum\gamma(p,q)C_v(p,q) \qquad (2.9)$$

where $C_v(p,q)$ is the mode heat capacity at constant volume, which itself is a function of temperature. At this point it is convenient to define an average Gruneisen parameter thus:

$$\bar{\gamma} = \frac{\sum\gamma(p,q)C_v(p,q)}{C_v} \qquad (2.10)$$

where C_v $(= \sum C_v(p,q))$ is the total heat capacity at constant volume. Substituting for $\bar{\gamma}$ into (2.9) gives

$$\alpha = \frac{\kappa\bar{\gamma}C_v}{V} \qquad (2.11)$$

(the subscripts 0 have been dropped). This leads to the definition of the thermal Gruneisen parameter γ^{th} by the more familiar equation

$$\gamma^{th} = \frac{\alpha B}{c_v} \qquad (2.12)$$

where B is the bulk modulus ($= \kappa^{-1}$) and c_v is the specific heat capacity at constant volume. It can be seen that the average Gruneisen parameter characterises the thermal expansion in the same manner as the Debye temperature characterises the specific heat, and as such can be considered to express the anharmonicity through a single parameter model.

2.3 CONNECTION BETWEEN LATTICE DYNAMICS AND ELASTICITY.

In the limit of infinitely long acoustic waves, all the atoms in the unit cell move in parallel with vanishingly small frequencies. This is also approximately true of very long wavelength modes which are very close to the centre of the Brillouin zone, and the frequencies associated with these modes are very small. These low frequency modes correspond to sound waves, and as such the frequencies are determined by the elastic constants and the density of the material. However the frequencies of all modes are governed by the interatomic force constants, and so there must be a close relationship between these and the elastic constants, and because of this the anharmonicity of the long wavelength modes will manifest itself as nonlinear elastic behaviour.

For infinitesimal strains, stress is directly proportional to strain and the elasticity is governed by the fourth rank elastic stiffness tensor (Hooke's law). The elastic constants are generally introduced via the relation $\sigma_{ij} = C_{ijkl}\epsilon_{kl}$, where σ_{ij} is the stress tensor, ϵ_{kl} the strain tensor and C_{ijkl} the elastic constants, which are referred to as second order (Nye, 1957). For finite strains, the elasticity becomes nonlinear, and the stress is no longer proportional to the strain; third and higher order elastic constants should now be considered. In order to define what is meant by second and third order constants, it is best to adopt a thermodynamic approach, as these constants are properties of the physical state of the crystal. Such an approach was first developed by Murnaghan (1951) and later extended by Wallace (1972). In the following sections, the fundamental theory of thermoelasticity will be briefly outlined, leading eventually to the thermodynamic definitions of elastic constants of any order as given by Brugger (1964).

2.3.1. Strain variables.

Since there are excellent treatments of the the theory of elasticity in several texts (see, for example Murnaghan 1951, Landau and Lifshitz 1970), only the important results need be summarised here in order to clarify the notation in preparation for the next chapter, when small amplitude elastic waves in crystals will be discussed. To this end, the notation of Thurston and Brugger (1964) will be adopted, and tensor notation will

be assumed throughout.

Consider a crystal in an initial (unstrained) configuration, and let the coordinates of a particle in this crystal be a_i (i=1,2,3). After a stress has been applied, the crystal reaches a final (strained) configuration, when the new coordinates of the particle can be denoted by X_i. For homogeneous strains, the two sets of coordinates are related by the *deformation gradients* $(\partial X_i / \partial a_j)$:

$$X_i = \left(\frac{\partial X_i}{\partial a_j}\right) a_j \quad . \tag{2.13}$$

The displacements $u_i (=X_i - a_i)$ can be related to the initial configuration by the *displacement gradients* $(\partial u_i / \partial a_j)$:

$$u_i = \left(\frac{\partial u_i}{\partial a_j}\right) a_j \quad . \tag{2.14}$$

Another way of describing the strained state of a crystal is by considering the change in the square of the distance between two adjacent points from the initial to the final configuration. This leads to the definition of the *Lagrangian strain parameters* η_{ij}:

$$\eta_{ij} = \frac{1}{2}\left[\frac{\partial u_i}{\partial a_j} + \frac{\partial u_j}{\partial a_i} + \left(\frac{\partial u_l}{\partial a_i}.\frac{\partial u_l}{\partial a_j}\right)\right]. \qquad (2.15)$$

(2.15) can be rewritten in a more usual form

$$\eta_{ij} = \frac{1}{2}\left[\frac{\partial u_l}{\partial a_i}.\frac{\partial u_l}{\partial a_j} - \delta_{ij}\right] \quad . \qquad (2.16)$$

From (2.15,16) it can be seen that the η_{ij} are symmetrical, and hence contain no rotational information, and since the choice of origin is arbitrary, they are also translationally invariant. The strained configuration can be completely defined by the initial configuration coordinates a_i together with the nine displacement or deformation gradients, but the Lagrangian strain parameters contain no information about the rotation of the crystal.

Another useful quantity is the Jacobian, defined by

$$J = \left|\frac{\partial u_i}{\partial a_j}\right| = \frac{\delta V_o}{V} = \frac{\rho_o}{\rho} \qquad (2.17)$$

that is the determinant of the displacement gradients is equal to the ratio of the volumes in the initial and final state.

2.3.2. Stress and Thermodynamic Tensions.

The stress tensor σ_{ij} is generally defined as the force per unit area of the deformed body, that is in the final configuration given by the coordinates X_i. This makes the kinematics of the stress-strain relationship difficult since the strains are defined in the initial configuration a_i. For this reason the differential of the work done by the stress is not equal to the stress components multiplied by the differentials of the corresponding strain components, i.e.

$$dW \neq \sigma_{ij} d\eta_{ij} \quad . \tag{2.18}$$

For convenience in calculating the thermodynamic state equations, Truesdell and Toupin (1961) defined *thermodynamic tensions* (t_{ij}) such that

$$dW = t_{ij} d\eta_{ij} \quad . \tag{2.19}$$

The thermodynamic tensions are related to the stresses by the nine deformation gradients:

$$\sigma_{ij} = J \frac{\partial X_i}{\partial a_s} \cdot \frac{\partial X_j}{\partial a_t} t_{st} \quad . \tag{2.20}$$

Now that the stress and strain variables have been introduced, the elastic constants can be defined.

2.3.3. Thermodynamic Definition of Elastic Constants.

From the combined first and second laws of thermodynamics, the two thermodynamic potentials, the internal energy U and the Helmholtz free energy F, can be written (Thurston, 1964):

$$dU = TdS + \frac{1}{\rho_o} t_{jk} d\eta_{jk} \qquad (2.21a)$$

$$dF = -SdT + \frac{1}{\rho_o} t_{jk} d\eta_{jk} \quad . \qquad (2.21b)$$

From (2.21a,b) the thermodynamic tensions are given by

$$t_{ij} = \rho_o \left(\frac{\partial U}{\partial \eta_{ij}}\right)_{T\eta'} = \rho_o \left(\frac{\partial F}{\partial \eta_{ij}}\right)_{S\eta'} \quad . \qquad (2.22)$$

These relations are directly analogous to the more general thermodynamic equation $P=(\partial U/\partial V)_S$. The thermodynamic state functions must be rotationally and translationally invariant, and so the only description of the strained state required is that given by the

Lagrangian strain parameters, since these are similarly invariant.

The definition of the second order adiabatic elastic constants follows directly from (2.22) since

$$C^{S}_{ijkl} = \left(\frac{\partial t_{ij}}{\partial \eta_{kl}}\right)_{S\eta'} = \rho_0 \left(\frac{\partial^2 U}{\partial \eta_{ij}\partial \eta_{kl}}\right)_{S\eta'} \qquad (2.23)$$

and similarly for the isothermal constants;

$$C^{T}_{ijkl} = \left(\frac{\partial t_{ij}}{\partial \eta_{kl}}\right)_{T\eta'} = \rho_0 \left(\frac{\partial^2 F}{\partial \eta_{ij}\partial \eta_{kl}}\right)_{T\eta'} . \qquad (2.24)$$

Now the use of the term second order becomes clear: the second order elastic constant is defined as the second partial differential of the internal or free energy with respect to strain. Extending this, the elastic constants of any order n (n>2) can now be defined as the n^{th} partial derivatives of U or F with respect to the Lagrangian strains. Hence the third order adiabatic constants are defined as

$$C^{S}_{ijklmn} = \rho_0 \left(\frac{\partial^3 U}{\partial \eta_{ij}\partial \eta_{kl}\partial \eta_{mn}}\right)_{S\eta'} . \qquad (2.25)$$

A similar expression is obtained for the isothermal constants. The elastic constants defined above are the coefficients of the Taylor expansion of either U or F in terms of the strain. Thus the strain energy density, $\rho_o U(\eta) = \rho_o U(S,\eta) - \rho_o U(S,0)$, can be written as

$$\rho_o U(\eta) = \frac{1}{2} C^S_{ijkl}\eta_{ij}\eta_{kl} + \frac{1}{6} C^S_{ijklmn}\eta_{ij}\eta_{kl}\eta_{mn} + \ldots \quad (2.26)$$

There is no first derivative since all the derivatives are evaluated at zero strain. Hence $t_{ij}=0$.

2.3.4. Elastic Constants of Cubic Materials.

Because of the rotational invariance of the elastic constants, the number of independent constants is reduced. In most cases the Voigt notation is adopted were by pairs of indices are replaced by a single index: 11→1, 22→2, 33→3, 23→4, 13→5, 12→6. So for example C_{1122} becomes C_{12}, while generally the second order constants are written as C_{ij} and the third order constants as C_{ijkl}.

The materials which are studied in this thesis all possess the cubic structure: zinc blende or rocksalt. The effect of the symmetry of the cubic structure on the elastic constants is to reduce the number of independent constants still further. For the second order constants,

there are only three independent values, namely C_{11}, C_{12} and C_{44}, all others being either equal to one of these or zero. For the third order constants, there are six independent elements: C_{111}, C_{112}, C_{123}, C_{144}, C_{155}, C_{456}. In all future discussions, only those constants relating to cubic symmetry will be dealt with.

2.4 THE ELASTIC GRUNEISEN PARAMETER.

Since there is a strong connection between the long wavelength modes and elasticity, it is not suprising that the Gruneisen parameters for these modes can be related directly to the elastic constants. Brugger (1965) has developed equations for the long wavelength Gruneisen parameters in terms of the second and third order elastic constants, and for cubic symmetry they are given by (Brugger and Fritz 1967)

$$\gamma(p,N) = -(1/6w)[3B+2w+k] \qquad (2.27)$$

where

$$w(p,N) = C_{11}K_1+C_{44}K_2+C_{12}K_3$$

$$k(p,N) = C_1K_1+C_2K_2+C_3K_3 \qquad (2.28)$$

with

$$K_1(p,N) = N_1^2U_1^2+N_2^2U_2^2+N_3^2U_3^2$$

$$K_2(p,N) = (N_1U_3+N_3U_1)^2+(N_3U_2+N_2U_3)^2 + (N_1U_2+N_2U_1)^2$$

$$K_3(p,N) = 2(N_2N_3U_2U_3+N_3N_1U_3U_1+N_1N_2U_1U_2) \qquad (2.29)$$

and

$$C_1 = C_{111}+2C_{112}$$
$$C_2 = C_{144}+2C_{155}$$
$$C_3 = C_{123}+2C_{112} \quad . \qquad (2.31)$$

The N_i and U_i are direction cosines for the direction of propagation and the direction of polarisation respectively, p is the branch index and B the bulk modulus.

In strict analogy to (2.10), a mean elastic Gruneisen parameter can be defined as a weighted average of all the $\gamma(p,N)$. In this instance, a low and high temperature limit can be defined (Brugger and Fritz 1967). In the low temperature limit, the mode gammas are weighted by the inverse of the cube of the mode velocity v(p,N);

$$\gamma_0^{el} = \int \frac{\gamma(p,N)v^{-3}(p,N)d\Omega}{v^{-3}(p,N)} \qquad (2.32)$$

where Ω is the solid angle. In the high temperature limit a spherical Debye surface can be assumed, and all the modes considered to be classically excited; the weighting factors become equal to Boltzmanns constant k, and γ_∞^{el}

can be calculated as a simple average over all directions:

$$\gamma_{\infty}^{el} = \frac{1}{3}\int \gamma(\mathbf{p},\mathbf{N})\frac{d\Omega}{4\pi} \quad . \tag{2.33}$$

The thermal Gruneisen parameter given by (2.12) contains contributions from all modes, including the optic branches. The elastic and thermal gammas are therefore not equivalent, although they can approach each other at very low temperatures where only the low energy zone centre acoustic modes are excited. Extensive use will be made of these Gruneisen parameters when discussing the importance of the long wavelength acoustic modes to structural stability in chapter IV.

CHAPTER 3

MEASUREMENT OF SOEC AND TOEC USING ULTRASONIC PULSE ECHO TECHNIQUES

CHAPTER 3

MEASUREMENT OF SOEC AND TOEC USING ULTRASONIC PULSE ECHO TECHNIQUES

3.1 INTRODUCTION.

In chapter 2, the SOEC and TOEC were defined thermodynamically. In this chapter, the methods by which they are determined experimentally will be dealt with. As was pointed out in chapter 2, the frequencies of the long wavelength phonon modes, corresponding to elastic (acoustic) waves are completely governed by the density and the elastic constants of the material. Hence measurement of the velocities of ultrasonic waves in crystals enables the direct measurement of the components of the SOEC tensor. The TOEC are related to the static stress derivatives of the SOEC (see chapter 2), and so they can be experimentally determined by measuring the change in ultrasonic wave velocity under hydrostatic pressure and uniaxial stress.

The use of ultrasonic experiments for the determination of elastic constants is now an established and accepted method. The experimental techniques used here, pulse echo overlap and pulse superposition, are well documented (Yogurtcu 1980, Brassington 1982), and so they will only be discussed briefly in section 3.3. Section 3.2 will concentrate more precisely on the fundamental theory of elastic wave propagation in crystals, following closely the treatment adopted in the definitive paper by Thurston and Brugger (1964), in which they derive expressions for

the stress derivatives of the velocities of ultrasonic wave modes in terms of the SOEC and TOEC.

3.2 ACOUSTIC WAVES IN CRYSTALS.

The subject of small amplitude elastic waves in crystals is treated in many texts (see for example Thurston 1964, 1965). The variation of the ultrasonic wave velocities with static stress (i.e. hydrostatic pressure or uniaxial stress), which enables the determination of the TOEC have been dealt with in detail by Thurston and Brugger (1964). Therefore in the next three subsections, only a brief outline of the theory will be given.

3.2.1 Small Amplitude Elastic Waves in Anisotropic Media.

When a small amplitude elastic wave propagates through a crystal, the coordinates of the final (strained) configuration (X) are no longer static, but are time dependent i.e. $X_i = X_i(t)$, the strains being due to the propagation of the wave. From continuum mechanics, the equation of motion of a solid is given by

$$\rho \ddot{x}_j = (\partial/\partial x_k)\sigma_{kj} \qquad (3.1)$$

where the notation used in chapter 2 has been retained. By employing (2.20) which relates the σ_{ij} to the

thermodynamic tensions t_{ij}, together with the definition of the Lagrangian strains η_{ij} (2.16, 2.23), the equations of motion (3.1) can be rewritten in the form (Thurston 1964)

$$\ddot{u}_i = C^s_{ijkl}\left(\frac{\partial^2 u_k}{\partial a_j \partial a_m}\right) \qquad (3.2)$$

where $u_i = x_i - a_i$, and a_i are the coordinates of the initial (unstrained) state. Since the propagation of the elastic wave can be considered to be adiabatic, the isentropic SOEC are required.

Seeking plane wave solutions of the form

$$u_i = u_i^0 \exp[j\omega(t-(\mathbf{n}.\mathbf{r}/v))] \qquad (3.3)$$

(where $\mathbf{n}$ is a unit vector in the direction of propagation) gives rise to a set of eigenvalue equations:

$$(C^s_{ijkm}n_j n_m - \rho v^2 \delta_{ik})u_{ik} = 0 \qquad (3.4)$$

where δ_{ij} is the Kronecker delta. These are known as Christoffels equations (Musgrave 1970). For non-trivial solutions, the determinant of the coefficients of (3.4) must vanish:

$$\left|C^{s}_{ijkm}n_j n_m - \rho v^2 \delta_{ik}\right| = 0 \qquad (3.5)$$

For each direction defined by n, there are three mutually perpendicular eigenvectors and three corresponding eigenvalues; the latter are the velocites of the three elastic waves that can be propagated in that direction, while the former are their polarisation directions. In certain crystallographic directions, these polarisations give rise to pure longitudinal and transverse (shear) waves; these directions are known as pure mode directions. In general however, in any given arbitrary direction the modes are neither purely longitudinal nor shear in nature. The pure mode directions which are experimentally important in cubic crystals are shown in figure 3.1.

3.2.2. Small Amplitude Waves in Homogeneously Strained Media.

To understand the effect of finite static strains on the velocities of ultrasonic waves in crystals, it is important to consider three states of the material. These are the natural or unstressed state, defined by the coordinates a, the coordinates of the initial or homogeneously stressed state X, and the time dependent coordinates x together with their corresponding displacement gradients $u_i = x_i - X_i$ due to the wave. Taking into account the finite stress applied to the crystal,

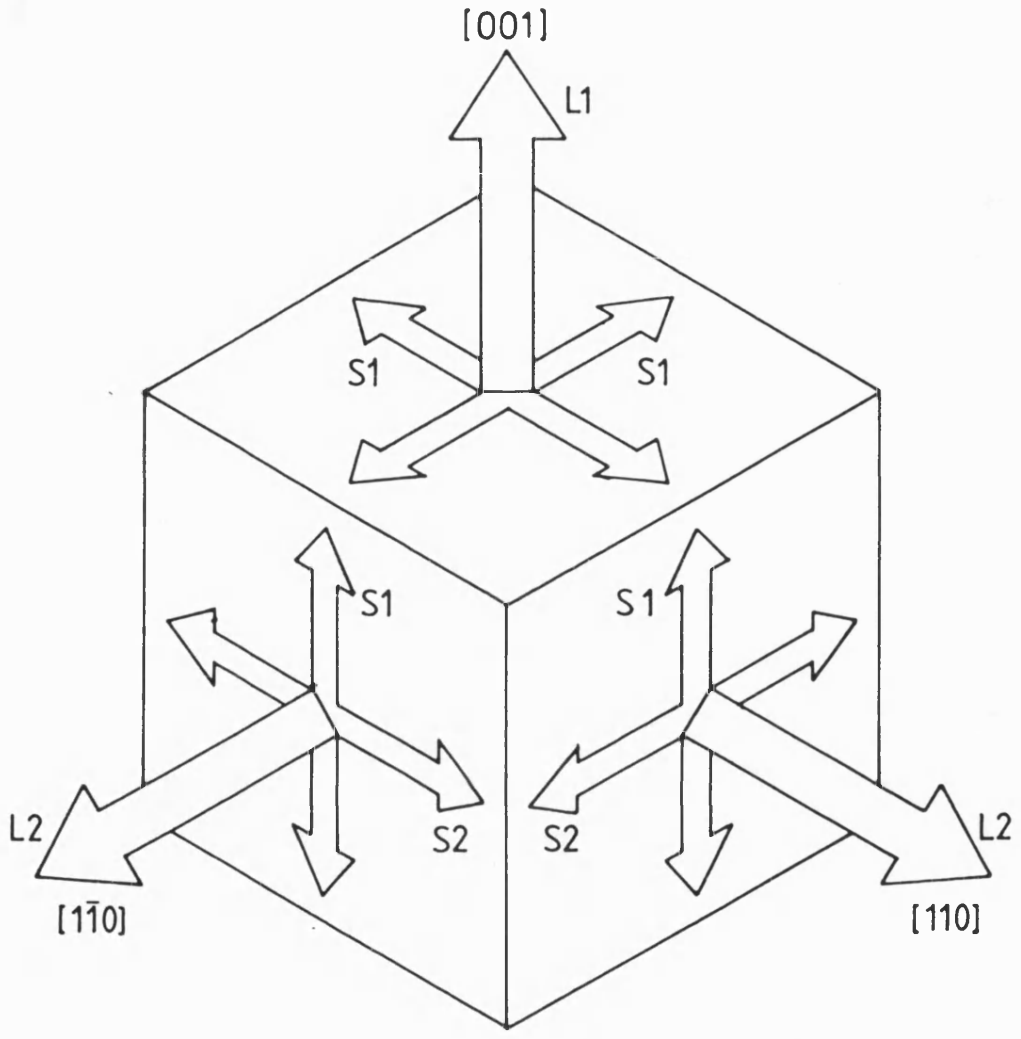

LONGITUDINAL L1 C_{11}

L2 $\frac{1}{2}(C_{11}+C_{12}+2C_{44})$

SHEAR S1 C_{44}

S2 $\frac{1}{2}(C_{11}-C_{12})$

FIGURE 3.1

Experimentally important pure mode directions in cubic crystals.

Thurston and Brugger (1964) have developed a set of linearised equations of motion:

$$\rho_0 u_j = \tilde{A}^s_{jkpm} \left(\frac{\partial^2 u_k}{\partial a_p \partial a_m} \right) \qquad (3.6)$$

Comparison of (3.6) with the equations of motion in an unstressed medium (3.2) show that the SOEC have now been replaced by another fourth rank tensor $\tilde{A}^s_{jkpm}$, the symbol $\tilde{}$ over the the A denoting that it is evaluated at the initial (unstressed) configuration X. The $\tilde{A}^s_{jkpm}$ can be considered to be modified SOECs, taking into account the effect of the static stress, and can be written as

$$\tilde{A}^s_{jkpm} = \delta_{jk} t_{pm} + \left(\frac{\partial X_j}{\partial a_q} . \frac{\partial X_k}{\partial a_i} \right) C^s_{pqms} \ . \qquad (3.7)$$

Thurston and Brugger (1964) now introduce the concept of *natural velocity* (W), by looking for plane wave solutions to (3.6) of the form

$$U_j = A_j \exp[j\omega(t-(N_i a_i / W))] \qquad (3.8)$$

where N and U are respectively unit vectors in the directions of propagation and polarisation referred to the unstressed configuration. The wave front is a

material plane which has a normal N in the natural (unstressed) state, and moves from the plane N.a=0 to N.a=L_o in the time L_o/W. Therefore W is the wave speed referred to the natural unstressed dimensions. Since it is this velocity that is generally measured in high pressure ultrasonic experiments and not the actual velocity v which is dependent on the stressed dimensions, it is of more use to express the theory in terms of W.

As with the unstressed case, substitution of the plane wave solutions (3.8) into the (3.6) give rise to a set of eigenvalue equations:

$$\rho_o W^2 U_j = \tilde{A}^s_{jkpm} N_p N_m U_k \qquad (3.9)$$

the non-trivial solutions of which are three mutually perpendicular eigenvectors, corresponding to the particle or polarisation direction, and the three eigenvalues are the corresponding values of $\rho_o W^2$. From the point of view of determining the TOEC, it is the variation of $\rho_o W^2$ with static stress that is of most interest, i.e. $[\rho_o W^2]'_{p=o,T} = (\partial/\partial p)(\rho_o W^2)|_{p=o,T}$, where the scalar quantity p represents either hydrostatic pressure or some uniaxial stress in a given direction M, which is again referred to the unstressed dimensions of the crystal. Analysis of $[\rho_o W^2]'_{p=o,T}$ lead to the following expressions for hydrostatic and uniaxial compression respectively (Thurston and Brugger 1964):

$$(\rho_0 W^2)'_{P=0,T} = -1 + 2wF_H + G_H$$

$$(\rho_0 W^2)'_{P=0,T} = -(\mathbf{N}.\mathbf{M})^2 + 2wF_U + G_U \qquad (3.10)$$

where

$$w = (\rho_0 W^2)_{P=0} = (\rho_0 v^2)_{P=0} = C^S_{prqs} N_p N_q U_r U_s$$

$$F_H = -S^T_{aars} U_r U_s$$

$$F_U = -S^T_{abrs} M_a M_b U_r U_s$$

$$G_H = -S^T_{auv} C_{uvpqrs} N_p N_q U_r U_s$$

and

$$G_U = -S^T_{abuv} C_{uvpqrs} M_a M_b N_p N_q U_r U_s$$

The S^T_{ijkl} are the isothermal elastic compliances. Table 3.1 gives the form of (3.9) for cubic crystals for certain experimentally important pure mode directions and uniaxial stress directions as well as hydrostatic pressure. The three independent elastic stiffness constants (SOEC) are related to the elastic compliances by the equations (Nye 1957)

$$C_{11} = \frac{S_{11} + S_{12}}{(S_{11}-S_{12})(S_{11}+2S_{12})}$$

$$C_{12} = \frac{-S_{12}}{(S_{11}-S_{12})(S_{11}+2S_{12})}$$

TABLE 3.1

N	U	M	$F_{U,H}$	$G_{U,H}$
[001]	[001]	H	1/3B	$\frac{1}{3B}(C_{111}+2C_{112})$
[001]	$\perp$[001]	H	1/3B	$\frac{1}{3B}(C_{144}+2C_{166})$
[110]	[110]	H	1/3B	$\frac{1}{3B}\left[(C_{111}+2C_{112})-\frac{1}{2}(C_{111}-C_{123})+(C_{144}+2C_{166})\right]$
[110]	[1$\bar{1}$0]	H	1/3B	$\frac{1}{3B}\left[\frac{1}{2}(C_{111}-C_{123})\right]$
[110]	[001]	H	1/3B	$\frac{1}{3B}(C_{144}+2C_{166})$
[110]	[110]	[001]	a	$\frac{1}{2}aC_{111}+\frac{1}{2}C_{112}(3a-b)-\frac{1}{2}bC_{123}-bC_{144}+2aC_{166}$
[110]	[1$\bar{1}$0]	[001]	a	$\frac{1}{2}aC_{111}-\frac{1}{2}C_{112}(a+b)+\frac{1}{2}bC_{123}$
[110]	[001]	[001]	-b	$aC_{144}+C_{166}(a-b)$
[001]	[001]	[110]	a	$aC_{111}+C_{112}(a-b)$
[001]	[1$\bar{1}$0]	[110]	$\frac{1}{2}(a-b+2c)$	$\frac{1}{2}C_{144}(a-b)+\frac{1}{2}C_{166}(3a-b)+2cC_{456}$
[001]	[110]	[110]	$\frac{1}{2}(a-b-2c)$	$\frac{1}{2}C_{144}(a-b)+\frac{1}{2}C_{166}(3a-b)-2cC_{456}$
[1$\bar{1}$0]	[1$\bar{1}$0]	[110]	$\frac{1}{2}(a-b+2c)$	$\frac{1}{4}C_{111}(a-b)+\frac{1}{4}C_{112}(5a-3b)+\frac{1}{2}aC_{123}+aC_{144}+C_{166}(a-b+4c)$
[1$\bar{1}$0]	[110]	[110]	$\frac{1}{2}(a-b-2c)$	$\frac{1}{4}C_{111}(a-b)+\frac{1}{4}C_{112}(a+b)-\frac{1}{2}aC_{123}$
[1$\bar{1}$0]	[001]	[110]	a	$\frac{1}{2}C_{144}(a-b)+\frac{1}{2}C_{166}(3a-b)-2cC_{456}$

$a = -S^T_{12}$, $b = -S^T_{11}$, $c = \frac{1}{4}S^T_{44}$, $3B = \frac{1}{(S^T_{11}+2S^T_{12})}$ = isothermal bulk modulus at P=0

The functions F and G for the pure mode directions used to determine the TOEC in cubic crystals. N, U and M are respectively the propagation, polarisation and stress directions, H stands for hydrostatic pressure.

$$C_{44} = \frac{1}{S_{44}} \tag{3.11}$$

and Nye (1957) also gives the relationship between the isothermal and isentropic compliances:

$$S^T_{11} = S^S_{11} + \frac{\alpha^2 T}{\rho_0 C_P}$$

$$S^T_{12} = S^S_{12} + \frac{\alpha^2 T}{\rho_0 C_P}$$

$$S^T_{44} = S^S_{44} \tag{3.12}$$

where α is the linear thermal expansion, C_P the specific heat capacity at constant pressure and T the absolute temperature.

It should be pointed out that the TOEC that appear in (3.9) and table 3.1 are not strictly those as defined by (2.25). This is because they are the isothermal strain derivatives of the isentropic SOEC, i.e. $(\partial C^S_{ijkl}/\partial \eta_{mn})_{T,P=0}$, and as such are neither isentropic nor isothermal , but instead are referred to as mixed. In general the mixed TOEC are not equivalent to the isentropic or isothermal constants. Thurston and Brugger (1964) have calculated the difference between the three types and the effect upon the experimentally determined values have been discussed in detail in the theses by Yogurtcu (1980) and Brassington (1982). They have shown that the differences are generally negligible when compared with experimental error, and can be ignored.

3.3 HIGH PRESSURE PULSE ECHO ULTRASONICS.

In order to determine experimentally the SOEC and TOEC it is necessary to measure accurately the transit time of ultrasonic waves in crystals and the variation of these transit times with hydrostatic and uniaxial stress. Measurement of ultrasonic velocities is usually invariably accomplished by the application of pulsed ultrasound techniques, which were originally developed in the late 1940s -early 1950s by such people as Huntingdon (1947), Mason and McSkimin (1947), Arenberg (1950) and Roderick and Truell (1952). The pulse echo method has remained basically unchanged and is now commercially available.

The basic principle is to introduce 10 MHz ultrasonic pulses of 1 to 2 μs duration into the crystal by means of a piezoelectric quartz transducer, X-cut for longitudinal waves, Y-cut for shear (transverse) waves, which is bonded to one face of the crystal using a suitable resin. For cubic crystals, the sample is normally cut in the form of a cube (ideally 1cm in length) whose faces are of the type [001], [110], and [1$\bar{1}$0]. This provides for all the crystallographic directions required for both hydrostatic and uniaxial stress experiments needed to determine all six independent TOEC from the one crystal. A single ultrasonic pulse travels down the specimen in the form of a plane wave, and is totally internally reflected at the opposite face. After a time $t=2l_o/v$, where l_o is the sample path length, v is the wave

velocity, the pulse arrives back at the the transducer, where it is detected and reflected back down the crystal. In this way, a set of multiple reflections is built up, and since there is a gradual attenuation of the ultrasound within the crystal, the detected reflections appear as a set of exponentially decaying echos.

The transit time can be measured from the time delay between adjacent echoes, and the velocity determined from $v=2l_o/t$ (see figure 3.2). When using this single ended configuration, it is necessary to have the two reflecting surfaces as parallel as possible, else wedging effects would eventually lead to side wall reflections which can lead to distortion of the echoes (see Truellet al 1969 for more details of wedging and diffraction effects). To avoid this, the samples are lapped flat and parallel to better than 1 part in 10^4 radians.

In order to resolve accurately the relatively small changes in ultrasonic velocities induced by the application of hydrostatic and uniaxial stress, special methods must be employed. The two systems used here, namely the pulse echo overlap and pulse superposition systems have been described in detail in the theses by Yogurtcu (1980) and Brassington (1982), and so it is the intention here to give only a brief outline of the the principles involved. For further detailed descriptions of the apparatus and possible sources of errors, the reader should refer to the literature cited.

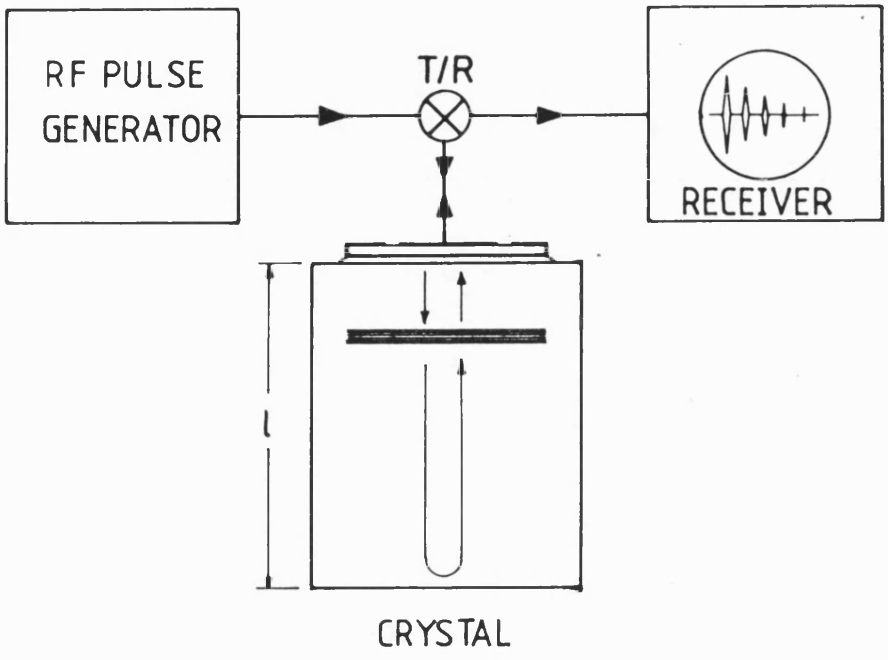

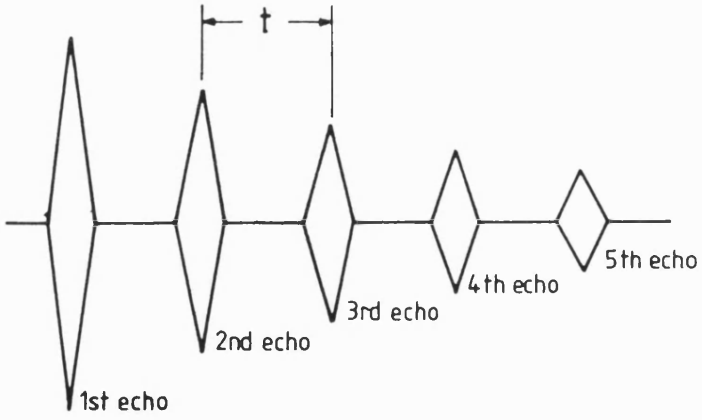

velocity $v = 2l/t$

FIGURE 3.2

Schematic diagram of the principles of ultrasonic velocity measurements using the pulse echo method.

3.3.1 Pulse Echo Overlap and Hydrostatic Pressure.

To resolve the small changes in ultrasonic wave velocities caused by the application of hydrostatic pressure, a pulse echo overlap method has been employed. The system used here is similar to that first described by May (1958) and later modified by Papadakis (1964, 1966, 1967). In essence, the transit times are measured by matching the phase of the 10 MHz signal within the echoes, rather than merely matching the envelope. In this way, changes of 1 part in 10^4 can be resolved. This is accomplished by triggering the oscilloscope from a high resolution frequency source at a frequency $f=1/t$, where t is the round trip transit time. This has the effect of overlapping all the successive echoes on top of each other. By use of a dual strobe which is also triggered by the frequency source, two echoes can be singled out in order to match their phases more easily. Figure 3.3 shows a block diagram of the entire apparatus. The R.F. pulse generator is triggered by a signal from the frequency source which has been divided down by a large number (1000-10000). This ensures that the echoes from one pulse have completely died away before the next pulse is generated.

The general experimental technique is to expand the oscilloscope trace of the two overlapped echoes so that the 10 MHz signals can be clearly seen. The high resolution frequency source is then adjusted to bring the two echoes into phase, and the overlap frequency f is then read directly from the frequency meter. In a typical hydrostatic pressure experiment, the pressure is increased by, for example, 100-200 bars, and the

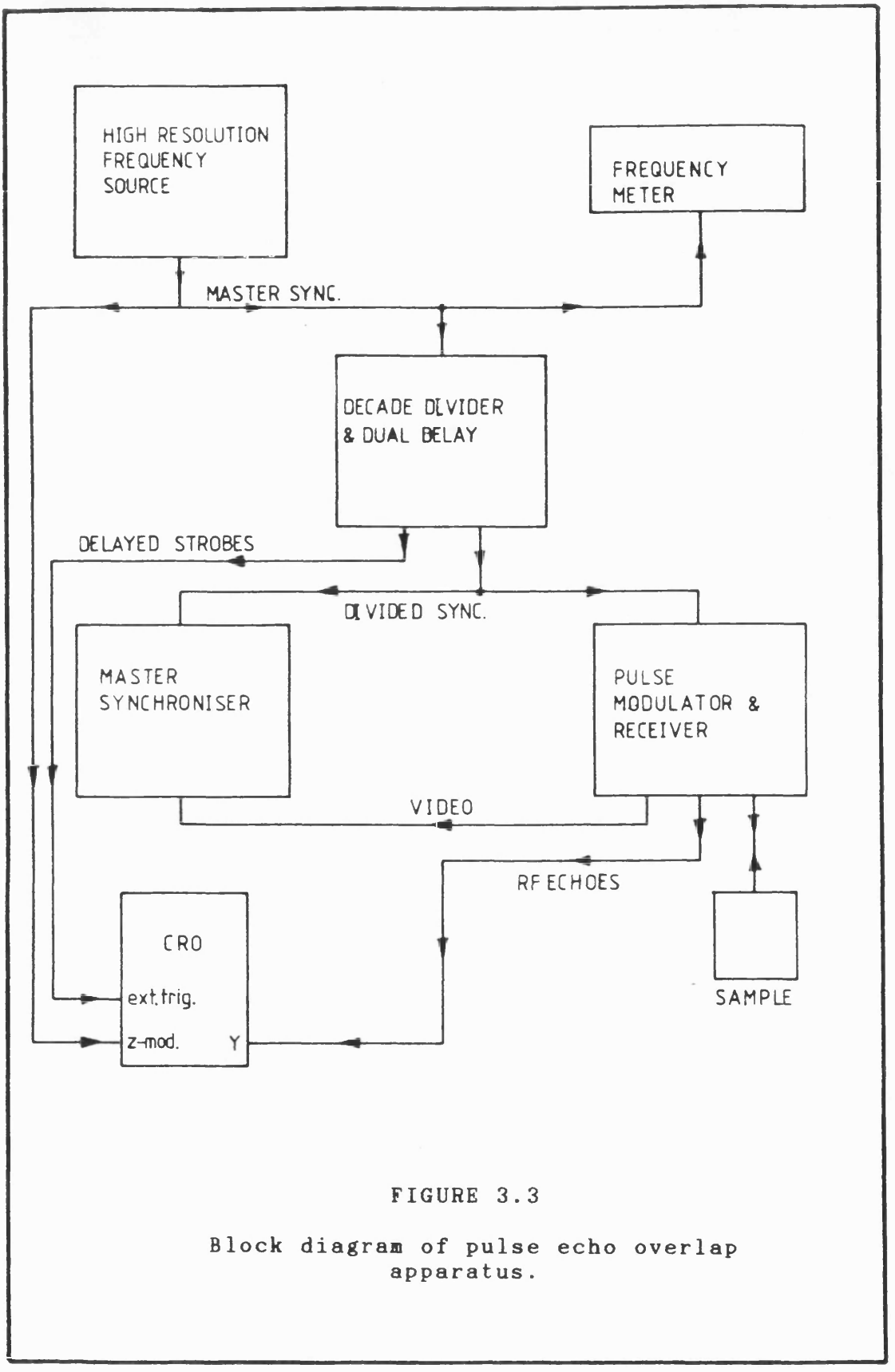

FIGURE 3.3

Block diagram of pulse echo overlap apparatus.

frequency source adjusted to bring the echoes back into phase. Thus a graph of overlap frequency against pressure is obtained. The natural velocity w is calculated directly from

$$W = 2l_0 f \qquad (3.13)$$

where l_0 is the unstressed dimensions of the crystal, and $(\rho_0 W^2)'_{P=0}$ is easily obtained from (3.13) as

$$(\rho_0 W^2)'_{P=0} = 8l_0^2 \rho_0 f_0 f' = 4\rho_0 l_0 W_0 f' \qquad (3.14)$$

where the subscript $_0$ refers those values at zero pressure. Hence it is the slope of the repetition frequency versus pressure graph that is primarily of interest.

The hydrostatic pressure system is basically a two piston and cylinder apparatus, castor oil being used as the transmitting medium. The sample is mounted on one of the pistons, and the pressure monitored by measuring the resistance of a small manganin coil also mounted on the piston (Brassington 1982), together with a thermocouple which is used to ensure that the temperature at which the measurements are taken is constant. The pressure bomb used in the experiments reported here is capable of pressures up to 10 kBars. However it was never found necessary to exceed 2 kBars.

3.3.2 Pulse Superposition System and Uniaxial Stress.

Because of the nature of hydrostatic pressure, relatively high pressures, typically of the order of 2-3 kBars can be applied to the crystal without causing damage. The changes in ultrasonic velocity associated with these pressures is such that the pulse echo overlap system proved to be more than sensitive enough. For uniaxial stress however, only small stresses could be applied (40 bars) to avoid producing damage. Clearly the changes in velocities produced by these relatively small stresses are orders of magnitude less than those observed with the high pressure experiments, and a more sensitive system is required to resolve them.

The system adopted here uses the pulse superposition technique (McSkimin 1961, 1965, McSkimin and Andreatch 1967) which can achieve sensitivities of one part in 10^7. It is basically an interference technique, whereby the pulse repetition frequency (PRF) is adjusted so that successive pulses fall on the p^{th} echo from the previous pulse. In this way the echos are made to sum up, and the PRF is adjusted to produce a constructive interference condition, at which point the summed echos have a maximum (see figure 3.4). The pulses in this case are generated by gating a continuous wave produced from a frequency synthesiser, which ensures that all the pulses are phase coherent. Because the echos are summed from a large

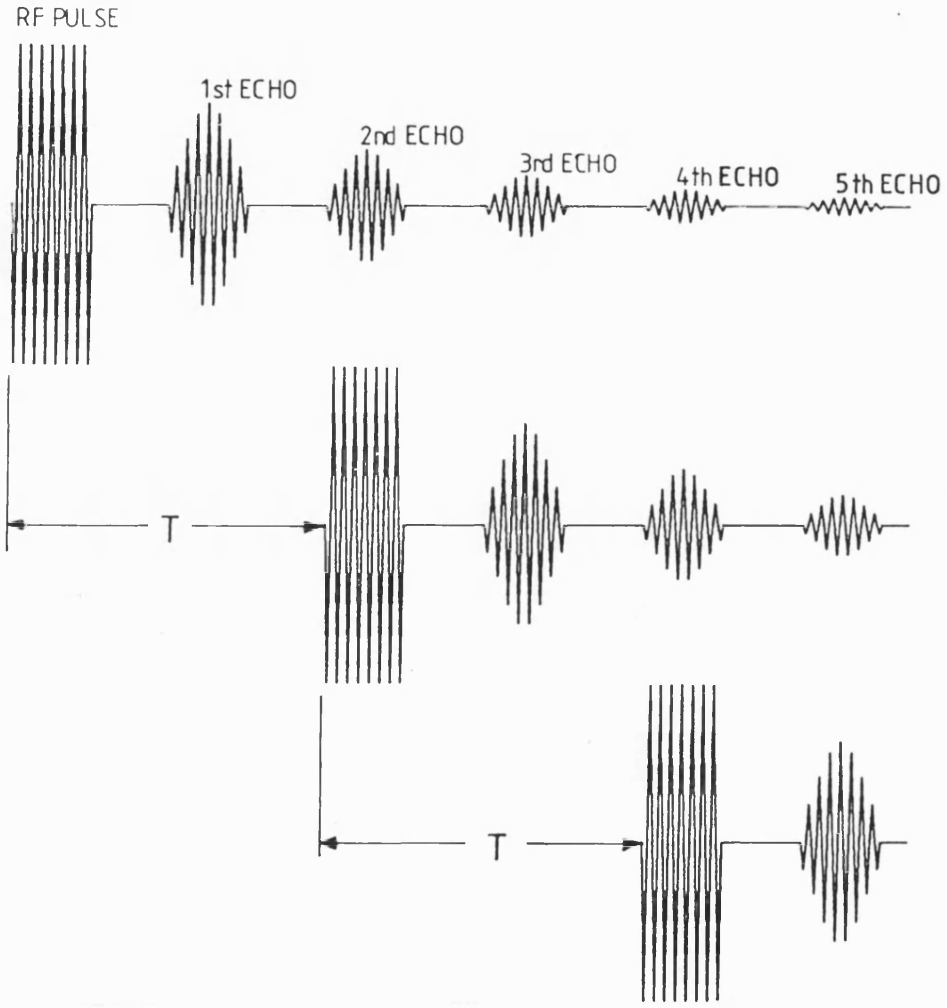

FIGURE 3.4

Diagram showing the superposition of wave packets in a crystal for p=2. When the 10 MHz signal is exactly in phase and there is no cycle mismatch, the pulse repetition frequency (PRF) is given by 1/T, where T is twice the round trip transit time.

number of pulses, the variation in amplitude of the summed echos as the PRF is moved away from the resonance condition is large, i.e. the resonance curve tends to be very narrow. It is this fact that allows such high sensitivity to be achieved.

The maximum resonance condition is detected via a method first proposed by Holder (1970). The PRF is frequency modulated by a small amount Δf, and this then appears as an amplitude modulation of the summed echos. (see figure 3.5). If the PRF is exactly at the resonance condition, an amplitude modulation of $2\Delta f$ will be observed owing to the symmetry of the resonance curve (figure 3.5a). However if the PRF is moved off resonance, this $2\Delta f$ amplitude modulation will vanish, leaving only a Δf modulation, the phase of which will be determined by the direction of the shift of the PRF from the resonance maximum (figure 3.5b). A phase sensitive detector is used to track the resonance maximum, and the error signal produced is used to adjust the frequency synthesiser so that the resonance condition is always maintained. Hence the system automatically tracks any change in the PRF. Figure 3.6 shows a block diagram of the system (Yogurtcu *et al* 1980), and a detailed description of the apparatus is given in the theses by Yogurtcu (1980) and Brassington (1982). The echo selector gate is used to single out the summed echos which are to be used, while the envelope detector and low pass filter strips the amplitude modulation from them, before sending the demodulated signal to the PSD.

The sensitivity of the system is dependent on the sharpness of the resonance peak. This inturn is affected

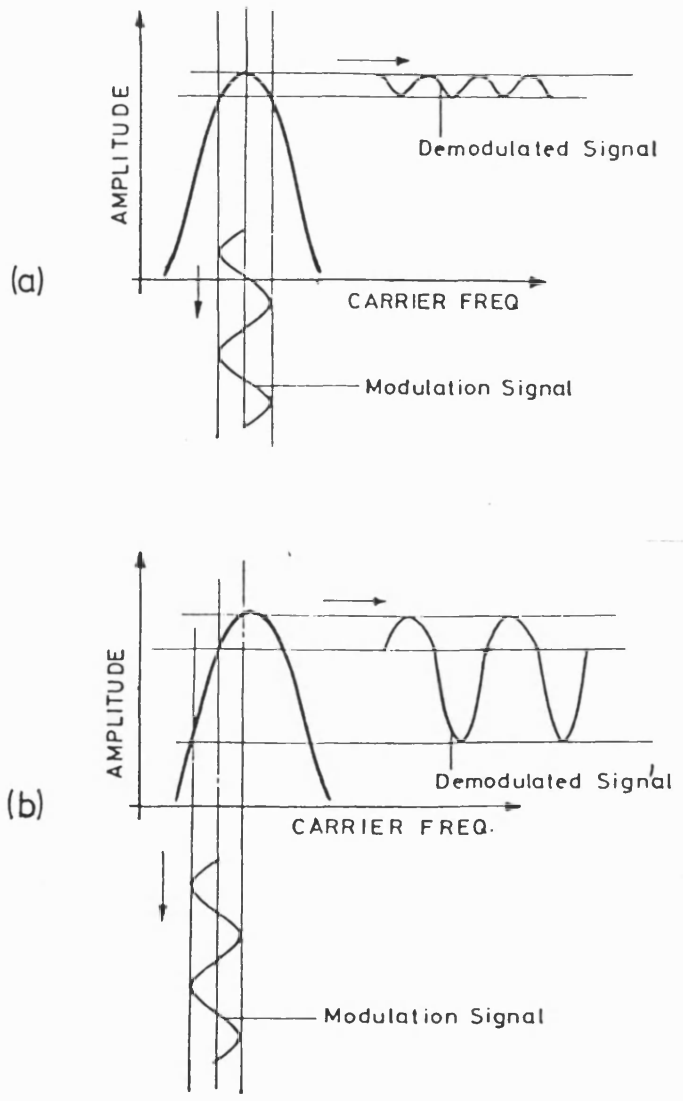

FIGURE 3.5

Diagram showing the frequency modulation of the PRF and corresponding demodulated signal for (a) the resonance and (b) the off resonance condition.

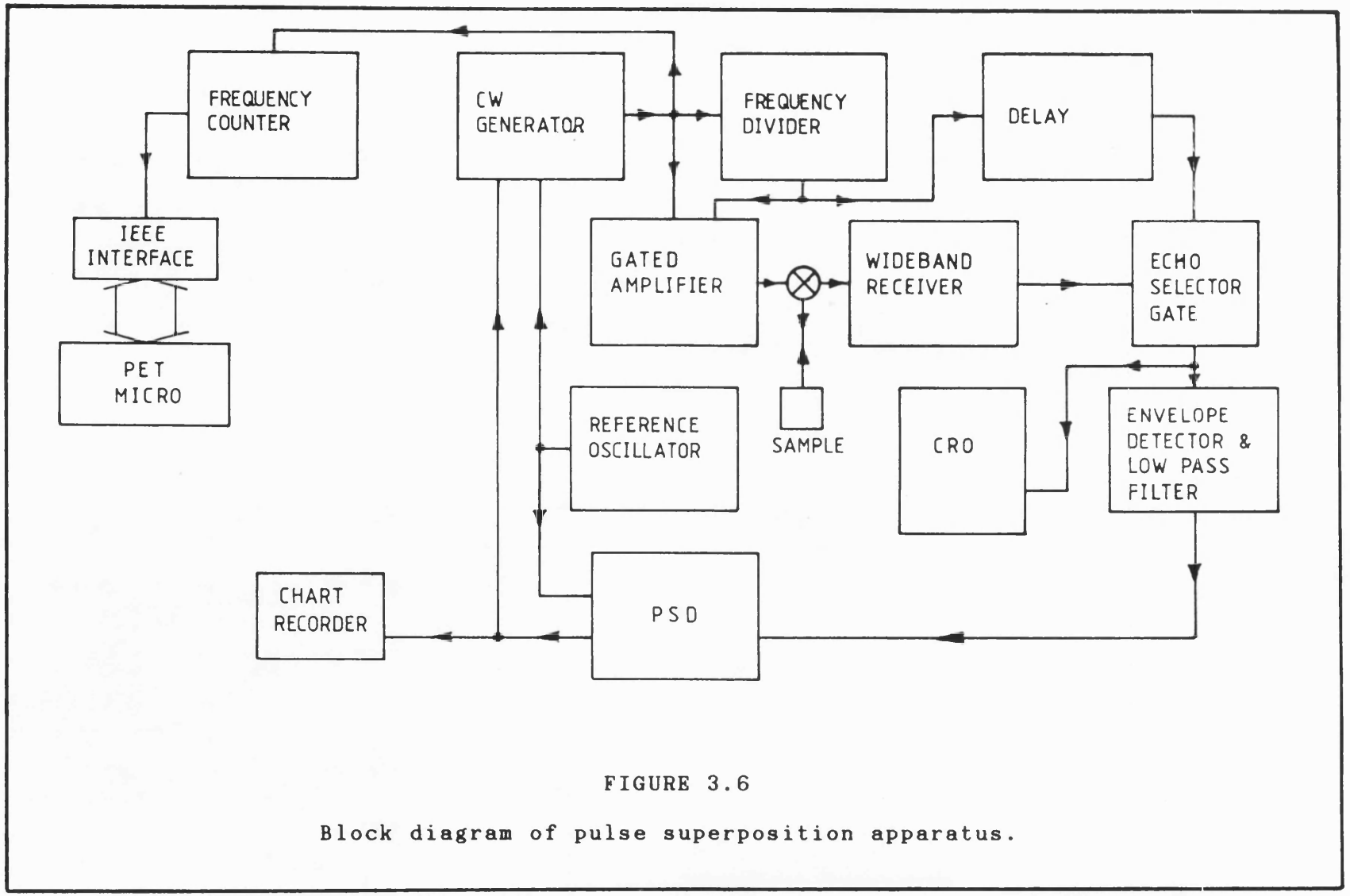

FIGURE 3.6

Block diagram of pulse superposition apparatus.

by the number of echoes summed, and the shape of the envelope of the echo train. The envelope should ideally be an exponential decay, due to the attenuation of the signal through the crystal. It was found that any other shape of envelope (which was quite often caused by wedging or diffraction effects, phase shifts at interfaces etc.) caused a severe degradation of the resonance peak, and resulted in loss of sensitivity. Again if for some reason only a few echos were produced per pulse, the quality of the resonance peak was impaired, and ideally the system required a large number of good echos to function at it's maximum capability.

The uniaxial stress was applied using a vice type press, which was so designed to give an even load across the faces of the crystal. The stress was measured via a proving ring and a micrometer. Because the pulse superposition system is so sensitive, the sample had to be shielded from drafts and thermally insulated to prevent temperature drifting, the effects of which could swamp the small changes in velocity caused by the stress. Again for a more detailed description of the uniaxial press, see the theses by Yogurtcu (1980) and Brassington (1982).

CHAPTER 4

SOFT TA MODES AND ANHARMONICITY IN CADMIUM TELLURIDE

CHAPTER 4

SOFT TA MODES AND ANHARMONICITY IN CADMIUM TELLURIDE

4.1 INTRODUCTION.

In this chapter, the relevance of vibrational anharmonicity to the structural stability of tetrahedrally coordinated zincblende compounds will be discussed, with particular emphasis on cadmium telluride. Using the experimental techniques described in chapter 3, the elastic behaviour of CdTe under pressure has been examined in order to extend and verify the trends noted for zincblende structure compounds (Miller *et al* 1981a, Ford *et al* 1982).

Under high pressure zincblende structure compounds transform to a denser phase. Some of the more ionic (II-VI) compounds transform at a pressure P_t accessible with the ultrasonic experiments described in chapter 3: Miller *et al* (1981) have measured the elastic constants of HgTe up to P_t (16×10^8 Pa) and Ford *et al* (1982) have done so for HgSe (P_t = 9.5×10^8 Pa). For CdTe P_t (=$30-35 \times 10^8$ Pa, Samara and Drickamer 1962, Borg and Smith 1967) is inaccessible with the present apparatus. However, following the ideas of Demerest *et al* (1977), extrapolation of the SOEC up to P_t, using data measured at more moderate pressures can be used to compare the elastic behaviour of zincblende compounds in the vicinity of P_t.

In section 4.2, the SOEC and their hydrostatic pressure derivatives, together with the TOECS of this (II-VI) semiconductor are calculated from the ultrasonic data, while in section 4.3, use is made of the hydrostatic pressure derivatives to extrapolate the SOEC up to P_t. Section 4.3 also deals with the application of a valence force field (VFF) model, which can provide further insight into elastic behaviour of CdTe in terms of short range directional and long range electrostatic interatomic forces. In particular correlations for zincblende compounds between the bond bending force constants β, P_t and the Phillips ionicity can be examined. The observed trends suggest that the more ionic compounds, like CdTe, have less stable tetrahedrally coordinated structures and hence lower values of P_t, which in turn are related to low values of β, since it is the bond bending forces that stabilize the sp^3 hybridised bond structure.

In section 4.4, the anharmonicities of the long wavelength acoustic phonon modes of CdTe are quantified using the generalised Gruneisen parameters which were introduced in chapter 2. The low and high temperature average acoustic Gruneisen parameters (see section 2.4) are calculated for CdTe, and these are compared with the thermal Gruneisen parameter. Finally in section 4.5, the soft TA modes, which are shown to occur in CdTe, and their particular relevance to the driving mechanism for structural phase transitions in zincblende structures are discussed.

4.2 EXPERIMENTAL RESULTS.

In the following sections, the data for CdTe obtained from the high pressure ultrasonic experiments described in chapter 3 will be presented. From these, the SOEC, together with their hydrostatic pressure derivatives, and the TOEC are calculated, and compared with other zincblende structure compounds.

The two samples of single crystal Bridgman grown CdTe used for the experiments were supplied ready cut and polished to the required specifications by the II-VI corporation, USA. The density and lattice parameter were taken as 5854 Kgm^{-3} and 6.4815 A respectively.

4.2.1 Ultrasonic velocities and SOEC.

Table 4.1 gives the ultrasonic wave velocities for the five modes obtainable in the [100] and [110] directions for CdTe. From these, the three SOEC were calculated, and these are given in table 4.2. C_{11}, C_{12} and C_{44} were calculated by linear regression of all the measured modes, and agree well with published data (table 4.2).

Zincblende structure compounds are piezoelectric, due to the fact that they do not possess a centre of inversion (Martin 1972). This can cause an effect known as piezoelectric stiffening, which can influence C_{44}. For CuCl for example, C_{44}^{ε} and C_{44}^{D} were found by Hanson *et al* (1974) to differ by about 12%;

TABLE 4.1

N	U	ρV^2	V (ms^{-1})
[001]	[001]	C_{11}	3019.2 ± 1.0
[001]	⊥[001]	C_{44}	1862.8 ± 0.8
[110]	[110]	$\frac{1}{2}(C_{11}+C_{12}+2C_{44})$	3350.2 ± 0.9
[110]	[$1\bar{1}0$]	$\frac{1}{2}(C_{11}-C_{12})$	1201.6 ± 0.5
[110]	[001]	C_{44}	1863.9 ± 0.9

Ultrasonic wave velocities measured in CdTe.

TABLE 4.2

C_{11}	C_{44}	C_{12}	T(K)	references
5.351	1.994	3.681	298	McSkimin and Thomas (1962)
5.33	2.044	3.65	300	Vekilov and Rusakov (1971)
5.57	2.095	3.84	77	
6.15	1.96	4.30	77	Berlincourt *et al* (1963)
5.38	2.018	3.74	298	Greenough and Palmer (1973)
5.62	2.061	3.93	77	
5.35±.01	2.033±.001	3.67±.02	292	present work

SOEC ($x10^{10}$ Nm^{-2}) of CdTe

piezoelectric effects were found to effect θ_D^{el} by about 1% and γ^{el} by about 10% (Barron *et al* 1977). However piezoelectric effects are expected to be considerably less in CdTe. The stiffened constant C_{44}^D is given by

$$C_{44}^D = C_{44}^E[1 + (k_{15}')^2] \qquad (4.1)$$

and the electromechanical coupling factor k_{15} is 0.026 at 77K (Berlincourt *et al*, 1963). Hence for CdTe C_{44}^D has been estimated as 2.032×10^{10} Nm^{-2} compared with 2.031×10^{10} Nm^{-2}, a stiffening of 0.07%. The [001] polarised shear mode propagated along the [110] direction and the degenerate shear mode propagated along the [001] direction give C_{44}^D and C_{44}^E respectively. To examine directly whether a significant difference exists for this particular crystal of CdTe, C_{44} was calculated from the ultrasonic wave velocities measured for both these modes, giving $C_{44}^D = 2.034 \pm 0.02 \times 10^{10}$ Nm^{-2} and $C_{44}^E = 2.031 \pm 0.002 \times 10^{10}$ Nm^{-2}. Piezoelectric stiffening is negligible for CdTe.

4.2.2 Effects of hydrostatic pressure and uniaxial stress; calculation of the TOEC.

Figures 4.1-3 show the effects of hydrostatic pressure and uniaxial stress on the *natural* wave velocity (see chapter 3) for all the modes listed in table 3.1, measured at a temperature of 20.0±0.2 degrees C. Using the temperature derivatives of the SOEC, measured by

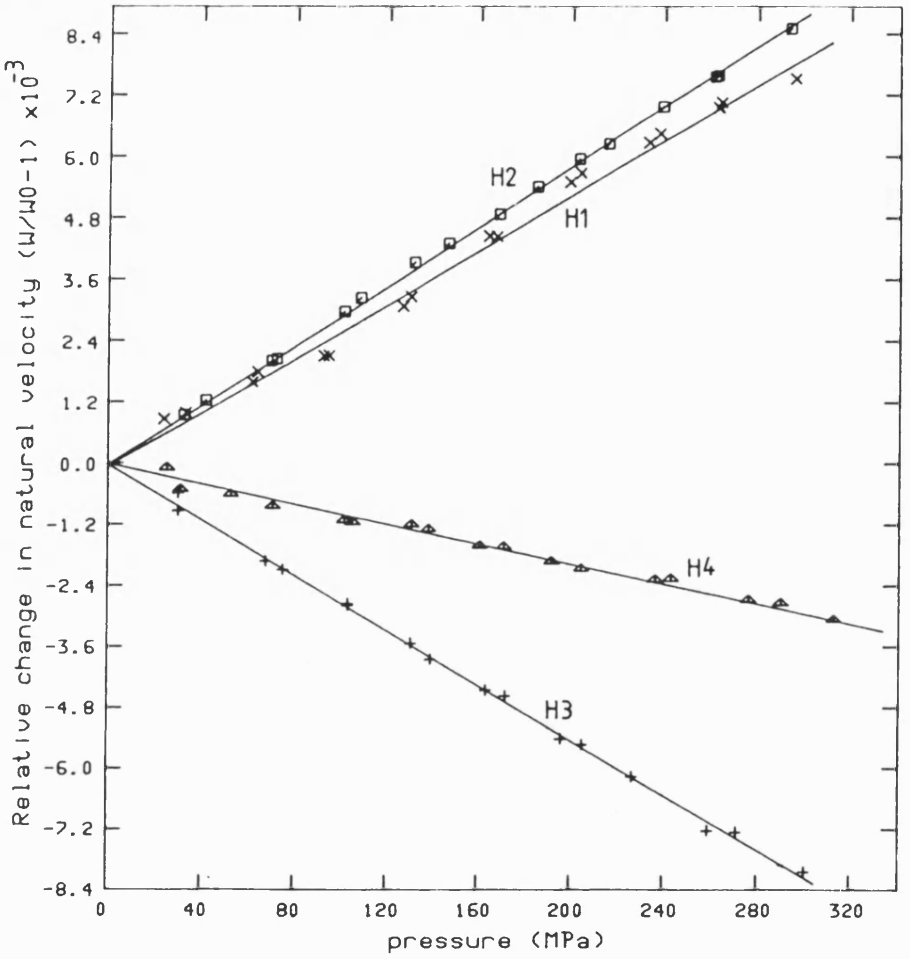

FIGURE 4.1

Relative change in natural wave velocity under hydrostatic pressure for CdTe. The modes are:

H1 **N**[001], **U**[001];
H2 **N**[110], **U**[1$\bar{1}$0];
H3 **N**[110], **U**[1$\bar{1}\bar{0}$];
H4 **N**[110], **U**[001];

where **N** and **U** are the propagation and polarisation vectors respectively.

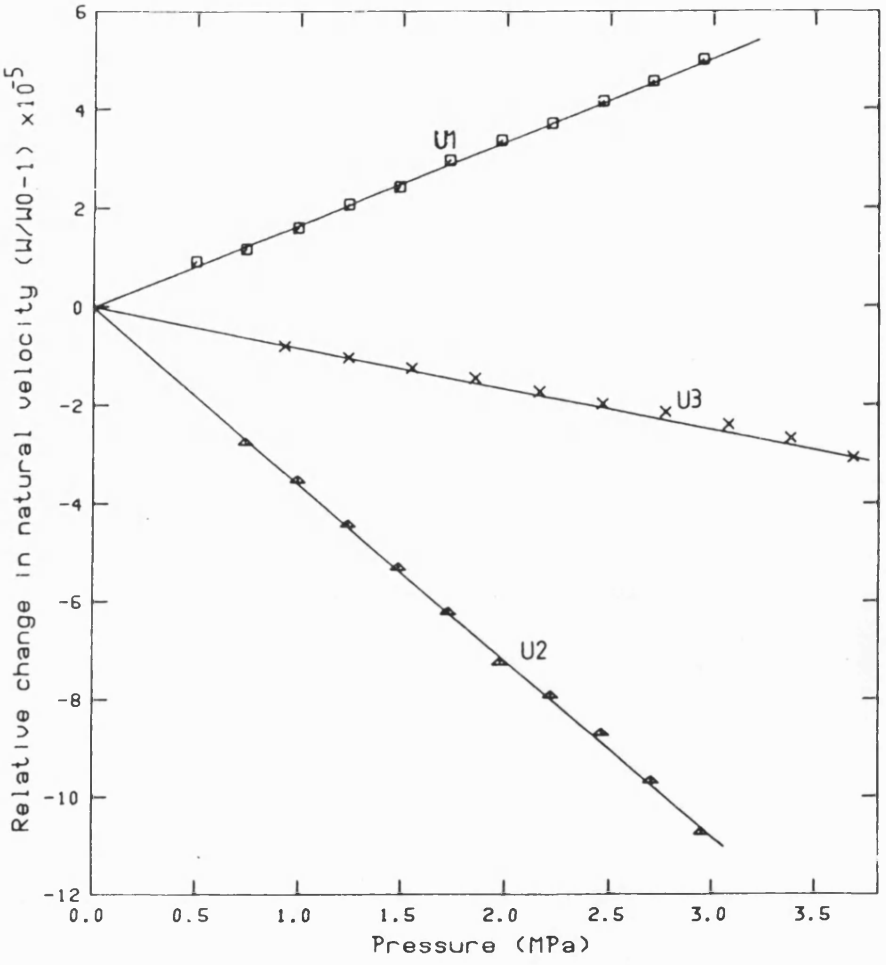

FIGURE 4.2

Relative change in natural velocity of ultrasonic waves propagated in the [001] direction under uniaxial stress in CdTe. The modes are:

U1 U[001], M[110];
U2 U[110], M[1$\bar{1}$0];
U3 U[110], M[1$\bar{1}$0];

where U is the polarisation vector and M is a vector in the direction of the applied uniaxial stress.

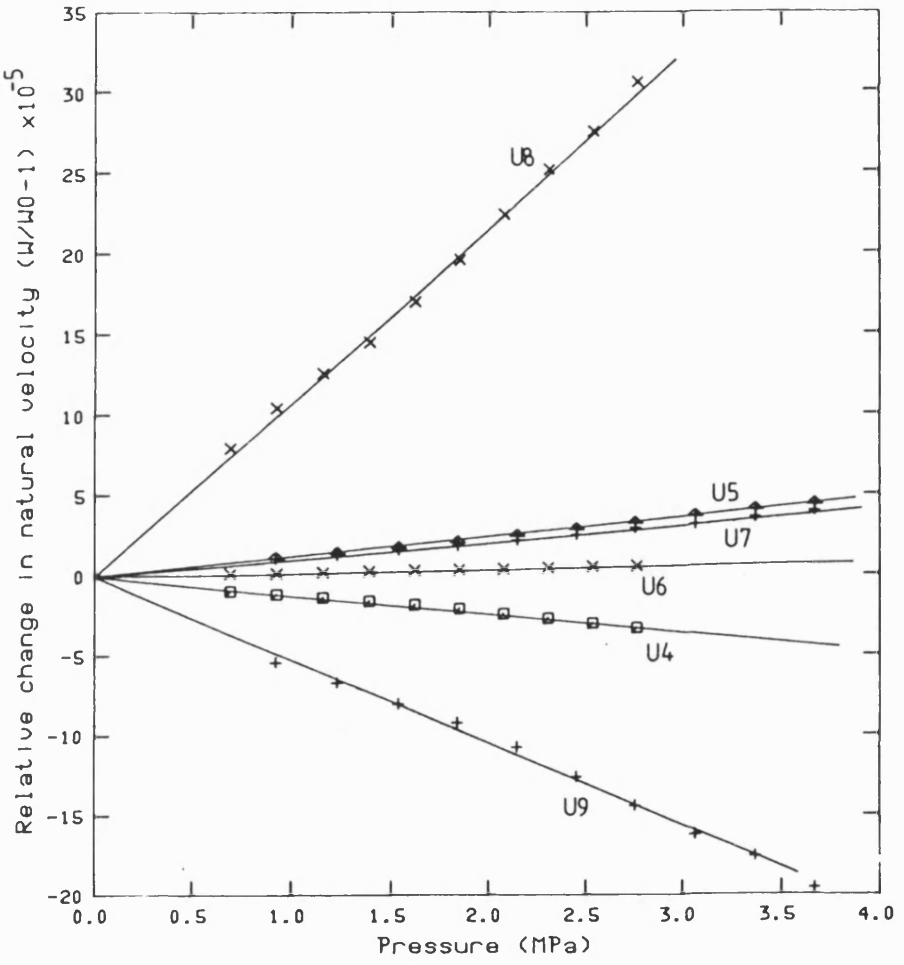

FIGURE 4.3

Relative change in natural velocity of ultrasonic waves propagated in the [110] direction under uniaxial stress in CdTe. The modes are:

U4 U[110], M[00$\bar{1}$];
U5 U[110], M[1$\bar{1}$0];
U6 U[001], M[00$\bar{1}$];
U7 U[00$\bar{1}$], M[1$\bar{1}$0];
U8 U[1$\bar{1}$0], M[001];
U9 U[1$\bar{1}$0], M[1$\bar{1}$0];

notation as in figures 4.1,2.

Greenough and Palmer (1973) as $\partial C_{11}/\partial T = -1.07$, $\partial C_{12}/\partial T = -0.84$, $\partial C_{44}/\partial T = -0.20 \times 10^{7}\ Nm^{-2}K^{-1}$, it was estimated that the small temperature variations caused an error of 0.004% in the overlap frequency measured in the pulse echo overlap experiments, substantially smaller than other experimental errors.

The hydrostatic pressure derivatives, calculated using

$$\left(\frac{\partial C_{IJ}}{\partial P}\right)_{T,P=0} = \frac{C_{IJ}}{C_{11}^{T}+2C_{12}^{T}} + \frac{d}{dP}\left[\rho_0 W^2\right]_{P=0} \qquad (4.2)$$

are compared with those of other zinc and diamond structure compounds in table 4.3. To find out if any measurable piezoelectric stiffening effects could be observed in $\partial C_{44}/\partial P$, the effects of hydrostatic pressure on the two modes giving C_{44}^{s} and C_{44}^{p} mentioned in section 4.2.1 were compared. No measurable effects were observed, $(\partial C_{44}^{s}/\partial P)_{P=0}$ and $(\partial C_{44}^{p}/\partial P)_{P=0}$ both being equal (-0.24 ± 0.02) within experimental error.

The uniaxial stress data, together with those for the hydrostatic modes, give a total of 13 independent pressure derivatives, from which the six independent TOEC were calculated by a weighted linear regression program using the relations of Thurston and Brugger (1964), which are given in table 3.1. Results are tabulated in table 4.4, again with those of other zincblende compounds and diamond type elements for comparison.

TABLE 4.3

	$\frac{dC_{11}}{dT}$	$\frac{dC_{44}}{dT}$	$\frac{dC_{12}}{dT}$		$\frac{dC_{11}}{dP}$	$\frac{dC_{44}}{dP}$	$\frac{dC_{12}}{dP}$	
	($\times 10^{7}$ $Nm^{-2}T^{-1}$)							
C	-1.48	-0.72	-0.71	(a)	5.98	2.98	3.06	(a)
Si	-1.34	-0.50	-0.70	(b)	4.34	0.80	4.22	(b)
Ge	-1.17	-0.61	-0.44	(c)	5.02	1.40	4.34	(c)
InSb	-0.87	-0.36	-0.55	(d)	4.80	0.54	5.10	(e)
GaSb	-1.00	-0.51	-0.41	(f)	4.96	1.01	4.64	(g)
GaAs	-1.12	-0.53	-0.44	(h)	4.63	1.10	4.41	(i)
ZnTe	-1.33	-0.44	-0.83	(j)	4.85	0.44	5.13	(k)
ZnSe	-1.54	-0.88	-0.54	(l)	4.21	0.49	4.73	(k)
GaP	-1.01	-0.55	-0.43	(f)	4.77	0.92	4.79	(m)
HgTe	-1.89	-0.84	-1.57	(n)	3.33	-0.12	4.01	(o)
HgSe	-3.05	-0.45	-2.83	(p)	1.89	-0.57	2.95	(q)
CdTe	-1.07	-0.20	-0.84	(r)	3.56±.06	-0.24±.02	4.35±.06	(s)

References: (a) McSkimin and Andreatch (1972); (b) McSkimin and Andreatch (1964); (c) McSkimin and Andreatch (1963); (d) Slutsky and Garland (1959); (e) Bashkin and Peresada (1974); (f) Boyle and Sladek (1975); (g) McSkimin et al (1968); (h) Cottam and Saunders (1973); (i) McSkimin, Jayaraman and Andreatch (1967); (j) Lee (1970a); (k) Lee (1970b); (l) Kusakov, Rusakov and Menster (1972); (m) Yogurtcu, Miller and Saunders (1981); (n) Cottam and Saunders (1975); (o) Miller *et al* (1981); (p) Kumazaki (1975); (q) Ford *et al* (1982); (r) Greenough and Palmer (1972); (s) present work.

Temperature and hydrostatic pressure derivatives of the SOEC of some tetrahedrally coordinated elements and compounds.

TABLE 4.4

	C_{111}	C_{112}	C_{123}	C_{144}	C_{155}	C_{456}	
Si	-8.25	-4.51	-0.64	0.12	-3.10	-0.64	(a)
Ge	-7.10	-3.89	-0.18	-0.23	-2.92	-0.53	(a)
InSb	-3.14	-2.10	-0.48	0.09	-1.18	0.002	(b)
GaAs	-6.22	-3.87	-0.57	0.02	-2.69	-0.39	(c)
GaP	-7.37	-4.74	-1.31	-1.07	-2.34	0.62	(d)
HgTe	-2.60	-1.70	-0.77	-0.17	-0.57	-0.01	(e)
CdTe	-2.13±.04	-2.10±.02	-0.42±.04	0.14±.01	-0.65±.01	-0.05±.01	(f)

References: (a) McSkimin and Andreatch (1964); (b) Drabble and Brammer (1967); (c) McSkimin and Andreatch (1967); (d) Yogurtcu, Miller and Saunders (1980); (e) Miller *et al* (1981); (f) present work

TOEC of some tetrahedrally coordinated elements and compounds. Units are 10^{11} Nm^{-2}.

4.3 DISCUSSION OF SOEC AND TOEC, EXTRAPOLATION TO HIGH PRESSURES AND THE APPLICATION OF THE VFF MODEL.

The elastic behaviour of CdTe fits well with the trends shown by other zincblende compounds. The decrease of the two shear moduli, C_{44} and $(C_{11}-C_{12})/2$ (=C') show that the slope of the transverse acoustic branches of the dispersion curve at the zone centre, corresponding to the long wavelength limit, are becoming smaller with applied stress. This *mode softening* behaviour is similar to that found in HgSe and HgTe. The presence of soft modes of this kind suggests that CdTe should undergo a shear induced first order phase transition, either to a cinnabar or rock salt structure, and indeed such a transition to the NaCl structure has been observed by Borg and Smith (1967) and Samara and Drickman (1962), at a pressure of about 30-35 kBar (3-3.5 GPa). The soft modes infer a decrease in the resistance of the crystal structure to a shear stress, and as the pressure is increased towards the phase transition, the crystal structure becomes unstable and less able to withstand the shear forces. At the phase transition pressure (P_t), the crystal can no longer withstand the stresses, and collapses into the NaCl structure.

The Born criterion for a stable crystal structure states that, for cubic crystals, $(C_{11}-C_{12})/2>0$, $C_{44}>0$ and $(C_{11}+2C_{12})/3>0$, these being the three eigenvalues of the elastic constant matrix; insisting that these three values are positive ensures that work is done when

applying stress to the crystal. A first order phase transition is characterised by a finite displacement of the atoms, which is often accompanied by a sudden volume change, 17% in CdTe at the transition pressure (Samara and Drickman 1962). Demarest *et al* (1977) have suggested as a modified Born criterion, that the dimensionless ratio C_t/B of a shear to bulk modulus ratio should reach a critical value before a first order transition will occur. By the use of pressure derivatives of the SOEC measured at moderate pressures, and assuming that the SOEC are linear with pressure, Rimai and Sladek (1979) have extrapolated up to P_t for several Ga and In (III-V) compounds. Their results show that C'/B is close to 0.2 at P_t. Yogurtcu *et al* (1981), by the same method, have found a number of zincblende compounds that at P_t, C'/B does indeed tend toward 0.2 , while for C_{44}/B is about 0.5. For CdTe, extrapolation up to P_t gives $C'/B=0.13$ and $C_{44}/B=0.35$, somewhat lower than the values quoted above, but still in good agreement with compounds such as HgTe and HgSe, which have high ionicities (0.68 and 0.65 for HgSe and HgTe respectively, compared to 0.717 for CdTe). Table 4.5 gives the values of the ratios at zero pressure and at the phase transition pressure for several zincblende compounds.

In sp^3, tetrahedrally coordinated compounds, the crystal structure must be stabilised against bond bending. The forces required to bend the bonds are characteristically high in these compounds, being associated with highly non-central forces inherent in the directional covalent bonds. Bond bending forces are responsible for stabilising the zincblende and diamond structures and preventing their collapse into denser

TABLE 4.5

	f_i	P_t (GPa)	C'/B	C_{44}/B	α (Nm^{-1})	β (Nm^{-1})	β/α	C'_t/B_t	$(C_{44})_t/B_t$	α_t (Nm^{-1})	β_t (Nm^{-1})	β_t/α_t
GaSb	0.261	6.7	0.427	0.767	33.78	7.24	0.214	0.285	0.567	55.92	8.04	0.144
GaAs	0.310	1.85	0.431	0.787	42.51	8.98	0.211	0.218	0.503	94.42	10.24	0.108
InSb	0.321	2.25	0.325	0.649	30.13	4.78	0.159	0.256	0.544	39.12	4.64	0.126
GaP	0.327	22.0	0.445	0.798	28.28	10.42	0.216	0.204	0.469	111.62	11.23	0.101
ZnTe	0.609	4.0	0.301	0.613	32.28	4.45	0.138	0.207	0.464	46.52	4.57	0.098
ZnSe	0.630	4.0	0.270	0.741	36.72	4.24	0.115	0.194	0.592	48.96	4.25	0.087
HgTe	0.65	1.6	0.201	0.502	29.27	2.54	0.087	0.165	0.435	34.35	2.52	0.073
CdTe	0.717	3.2	0.199	0.481	30.17	2.46	0.082	0.129	0.353	40.07	2.21	0.055
HgSe	0.68	0.95	0.153	0.439	39.99	2.59	0.065	0.140	0.418	39.90	2.42	0.061

Ratios C'/B, C_{44}/B and β/α for various zincblende compounds at zero pressure (no suffix) and at the phase transition pressure P_t (suffix t). P_t taken from Yogurtcu *et al* (1981) except CdTe (Borg and Smith 1967). All other ratios calculated by extrapolation using data given in table 4.3. C' is $(C_{11}-C_{12})/2$. Compounds are listed in order of increasing Phillips ionicity (f_i).

structures with eight- or twelvefold coordination numbers, and so from a point of view of understanding the mechanism of the phase transition in these materials, a quantitive analysis of these bond bending forces would be desirable. Such an analysis is given by the valence force field model (VFF).

4.3.1 The valence force field model (VFF).

In the VFF model, the bonds are interpreted in terms of short range bond stretching and bond bending forces. Keating (1966a,b) has developed a VFF model in which the SOEC of diamond type homopolar crystals are described in terms of bond stretch (α) and bond bend (β) harmonic force constants. This model was later extended by Martin (1970) for heteropolar, zincblende type crystals by including the longer range coulombic attractions. In terms of α and β, the SOEC are given by:

$$C_{11} = (\alpha+3\beta)/a - 4.053[Z^2e^2/4\pi\epsilon_0 a^4)]$$

$$C_{12} = (\alpha+\beta)/a - 5.538[Z^2e^2/(4\pi\epsilon_0 a^4)]$$

$$C_{44} = (\alpha+\beta)/a - 5.538[Z^2e^2/(4\pi\epsilon_0 a^4)] \qquad (4.3)$$
$$- \{(\alpha+\beta)/a - 4.189[Z^2e^2/(4\pi\epsilon_0 a^4)]\}\xi^2$$

where a is the lattice parameter, e the electronic

charge, ϵ_0 the permittivity of free space and

$$\xi = \frac{(\alpha+\beta)/a - 10.058[Z^2e^2/(4\pi\epsilon_0 a^4)]}{(\alpha+\beta)/a - 4.189[Z^2e^2/(4\pi\epsilon_0 a^4)]} \qquad (4.4)$$

is the internal strain parameter with Z the effective charge defined by the optic mode splitting

$$Z^2 = (\Omega\epsilon/4\pi e^2)M(\omega_l^2 - \omega_t^2) \qquad (4.5)$$

Ω being the volume of the primitive unit cell, and M is the reduced mass. For CdTe, Z has been taken as 0.838 (Martin 1970).

Phillips (1973) has pointed out that the ratio β/α is a measure of the covalent contribution to binding. As a crystal becomes more ionic, the bond bending forces tend to become smaller. In the ionic limit $f_i \to 1$, $\beta/\alpha \to 0$ since $\beta \to 0$, closed shell ionic structures being almost completely dominated by central, coulombic forces. By extrapolation of the SOEC using the dC_{IJ}/dP measured at low pressures, the theoretical curves of β/α as a function of pressure up to P_t have been calculated for various zincblende structures (figure 4.4). The higher ionicity (II-VI) compounds tend to have smaller values of β, and are less able to withstand high shear stresses and collapse at lower pressures (table 4.5). Conversely the more covalent (III-V) compounds undergo the transition at

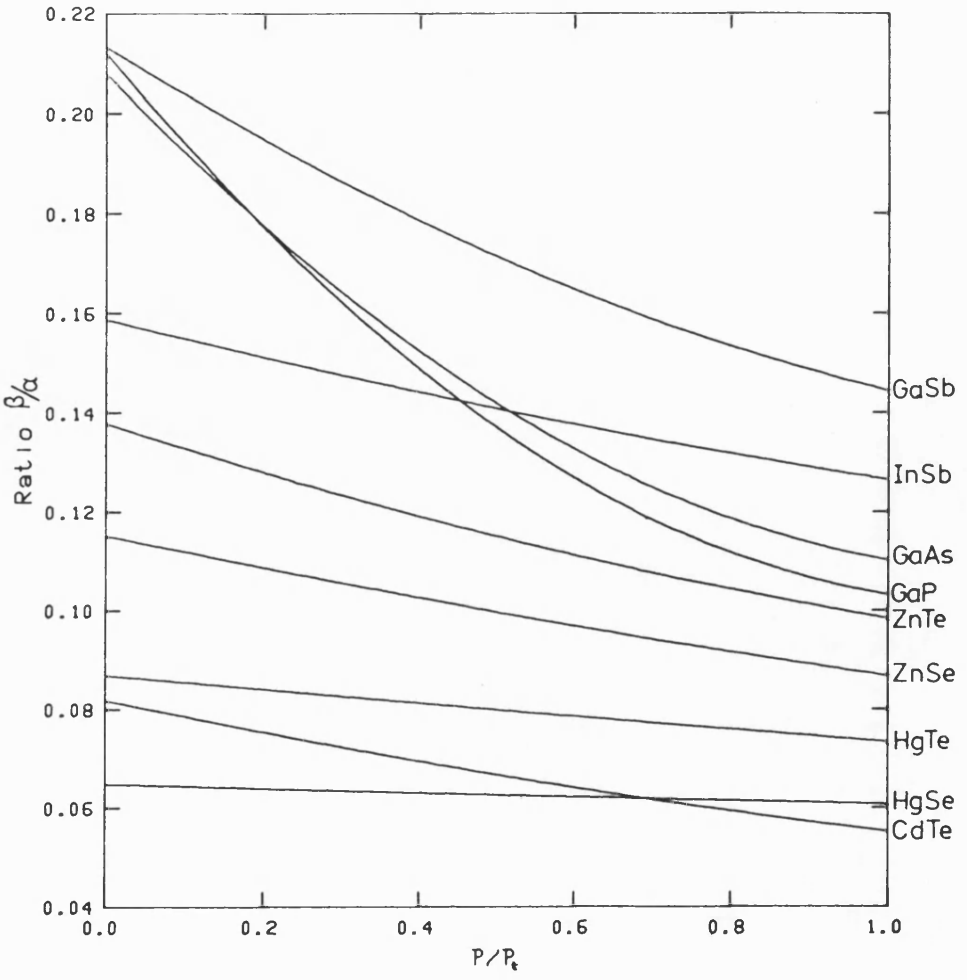

FIGURE 4.4

Theoretical change in the ratio (β/α) of bond stretch (α) to bond bend (β) force constants as a function of reduced hydrostatic pressure (P/P_t) for some (II-VI) and (III-V) zinceblende compounds.

much higher pressures due to the larger values of β, a high bond bending force constant producing a more stable tetrahedrally coordinated structure.

The β/α ratios for those compounds with low transition pressures (high ionicities) show hardly any change from zero pressure up to P_t, while those compounds with high transition pressures (low ionicities) exhibit a dramatic reduction as the phase transition pressure is approached (figure 4.4). The reduction in β/α ratio with pressure is predominantly due to an increase in the bond stretch force constant α, the values of β changing little with pressure (table 4.5). α shows a much greater tendency to increase for those compounds having a high value of P_t. The difference between α and α_t is comparatively small for the less stable (II-VI) compounds. Ford *et al* (1982) have noted a trend of decreasing β_t/α_t through the series of covalent elements, (III-V) semiconductors, (II-VI) compounds and have suggested that the ratio tends to a limit in the range 0.06 to 0.15 at the phase transition. This is confirmed by the values of β_t/α_t given in table 4.5, but figure 4.4 indicates that this ratio may cover to large a range to be an entirely satisfactory phase transition criterion. Ford *et al* (1982) have measured the pressure derivatives of the three ultrasonic modes propagated in the [110] direction right up to P_t for HgSe, and have shown that the longitudinal mode with stiffness $(C_{11}+C_{12}+2C_{44})/2$ also begins to soften as the transition is approached. There is no reason to suggest that this is anomalous behaviour, and it may be that softening of the longitudinal mode occurs in all tetrahedrally coordinated crystals at sufficiently high pressures. If this is the case, then the values of β_t/α_t

may be substantially smaller than the extrapolation indicates.

4.3.2 TOEC; extension to the VFF model.

The two force constants described in the section 4.3.1 (α and β) are harmonic force constants, and so are related only to the SOEC. Gerlich (1973) extended the Keating-Martin model to the TOEC, by including anharmonic force constants: a third order bond stretch force constant, γ, a third order bond bend constant, δ and a third order mixed bond stretch-bond bend force constant ϵ. In terms of these constants, the six TOEC are given by:

$$C_{111} = \gamma-\delta+9\epsilon+17.207[Z^2e^2/(4\pi\epsilon_0 a^4)]$$

$$C_{112} = \gamma-\delta+\epsilon+1.531[Z^2e^2/(4\pi\epsilon_0 a^4)]$$

$$C_{123} = \gamma-3\delta+3\epsilon+24.663[Z^2e^2/(4\pi\epsilon_0 a^4)]$$

$$C_{144} = \gamma(1-\xi)^2+\delta(1+\xi)^2+\epsilon(1+\xi)(3\xi-1)+[(\alpha-\beta)/a]\xi^2 +(24.663-33.526\xi+0.820\xi^2)[Z^2e^2/(4\pi\epsilon_0 a^4)]$$

$$C_{155} = \gamma(1-\xi)^2-\delta(1+\xi)^2+\epsilon(1+\xi)(3-\xi)+[(\alpha-\beta)/a]\xi^2 +(1.531-33.526\xi+10.062\xi^2)[Z^2e^2/(4\pi\epsilon_0 a^4)]$$

$$C_{456} = \gamma(1-\xi)^3+(24.663-50.288\xi+42.753\xi^2 \qquad (4.6)$$
$$-19.203\xi^3)[Z^2e^2/(4\pi\epsilon_0 a^4)]$$

The hydrostatic pressure derivatives can also be related to γ, δ and ϵ by the equations

$$\frac{\partial C_{11}}{\partial P} = -1-C_{11}/3B-(1/3B)\{3\gamma-3\delta+11\epsilon-20.269[Z^2e^2/(4\pi\epsilon_0 a^4)]\}$$

$$\frac{\partial C_{12}}{\partial P} = -1-C_{12}/3B-(1/3B)\{3\gamma+\delta-\epsilon+27.723[Z^2e^2/(4\pi\epsilon_0 a^4)]\}$$

$$\frac{\partial C_{44}}{\partial P} = -1-C_{44}/3B-(1/3B)\{3\gamma(1-\xi)^2-\delta(1+\xi)^2+\epsilon(1+\xi)(5+\xi)$$
$$+[3(\alpha-\beta)/a]\xi^2-[Z^2e^2/(4\pi\epsilon_0 a^4)](21.601+33.526\xi$$
$$-20.944\xi^2)\} \qquad (4.7)$$

The TOEC of CdTe are comparable to those of other zincblende compounds, especially to those higher ionicity compounds such as HgTe (table 4.4). C_{111} and C_{112} are much larger than any of the other constants, C_{456} being the smallest. Ford *et al* (1982) have pointed out that those compounds with higher phase transition pressures tend to have larger values of TOEC compared to those which have a lower P_t value, and the results for CdTe support this trend. A negative TOEC infers that the internal energy rises as the crystal is compressed. Thus those compounds with larger negative TOEC, e.g. GaP, would have a greater resistance to being compressed, and

consequently a higher phase transition pressure than those with smaller TOEC, such as CdTe or HgTe.

Application of the anharmonic VFF model to the CdTe data yields the three third order force constants as γ=-1.2, δ=0.13 and ϵ=-0.10 (x10^{10} Nm^{-2}). In this instance, the force constants were calculated using the hydrostatic pressure derivatives of the SOEC (equations 4.7). Again CdTe fits well with the observed trends (Gerlich 1973, Yogurtcu *et al* 1981, Miller *et al* 1981a, Ford *et al* 1982); γ tends to be considerably larger than either δ or ϵ, suggesting a greater degree of anharmonicity in vibrations which emphasize bond stretching rather than bond bending.

4.4 GRUNEISEN PARAMETERS: ANHARMONICITY OF THE LONG WAVELENGTH ACOUSTIC MODES.

In section 4 of chapter 2, the mode Gruneisen parameter $\gamma(p,N)$ was defined using the equations of Brugger (1965), and the average low and high temperature gammas were also introduced (Brugger and Fritz 1967). In order to quantify further the vibrational anharmonicity of CdTe, and more generally the zincblende structure compounds, the mode Gruneisen parameters have been numerically calculated using equations 2.27-31, and the results are shown in figure 4.5. $\gamma_o{}^{el}$ and γ_∞^{el} have been calculated for CdTe from equations 2.32 and 2.33, together with the elastic Debye temperature, θ_D^{el}, calculated from the equation

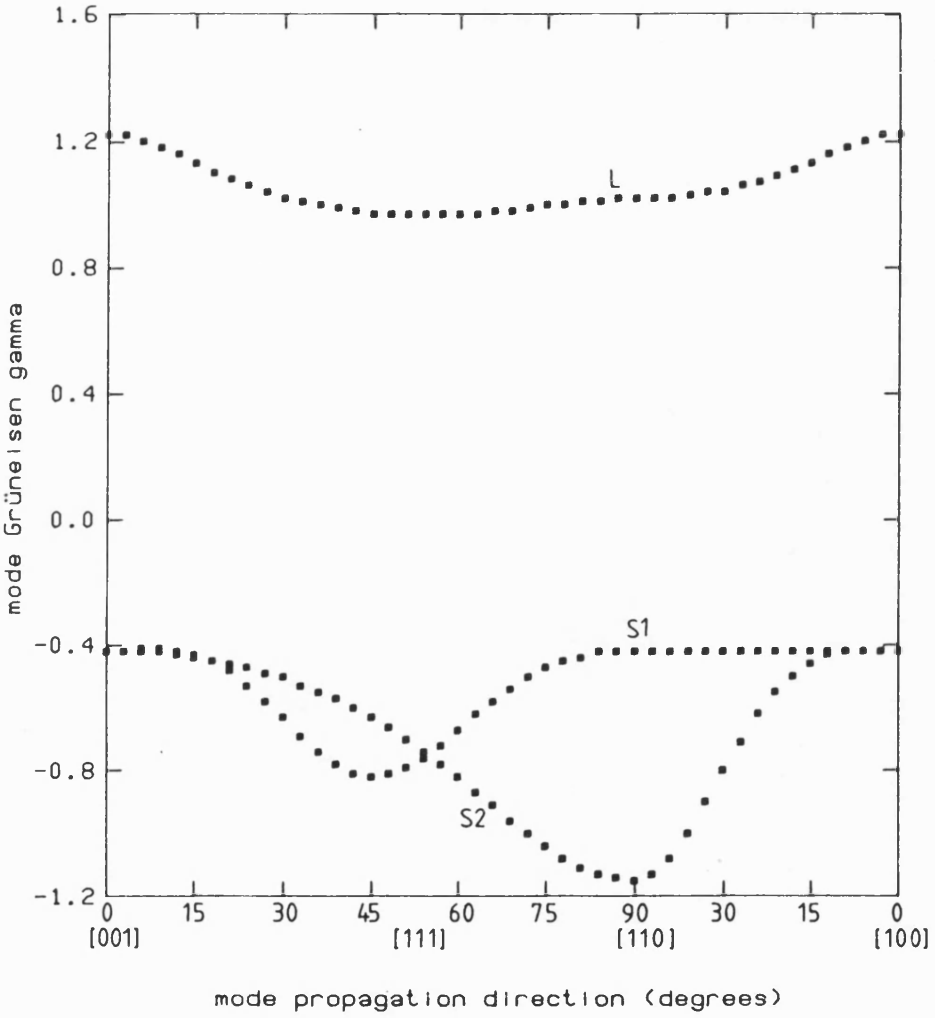

FIGURE 4.5

Mode Gruneisen parameters $\gamma(p,N)$ for longitudinal (L) and shear (S1,S2) modes, calculated as a function of mode propagation direction **N** in CdTe. For explanation of scale on horizontal axis see appendix I.

TABLE 4.6

	f_i	γ_0^{*l}	γ_∞^{*l}	γ_0^{th}	θ_D^{el}
C	0	0.911	1.003	-	2412.1
Si	0	0.238	0.487	0.44	650.7
Ge	0	0.504	0.737	0.49	373.9
GaSb	0.261	0.385	0.678	0.30	269.7
GaAs	0.310	0.375	0.657	0.32	347.6
InSb	0.321	0.085	0.303	0.21	205.5
GaP	0.327	0.267	0.579	-	445.5
ZnTe	0.609	0.052	0.486	0.07	224.2
ZnSe	0.630	-0.067	0.366	0.00	279.8
HgTe	0.65	-0.525	0.006	-1.2	141.7
HgSe	0.68	-1.318	-0.576	-	149.6
CdTe	0.717	-0.638	-0.063	-0.85	161.7

Low and high temperature acoustic Gruneisen parameters together with the low temperature thermal Gruneisen parameter (Barron *et al* 1980), the Debye temperature and Phillips ionicity for selected tetrahedrally coordinated elements and compounds.

$$\theta_D^{el} = \left(\frac{h}{k}\right)\left(\frac{18}{4\pi}\right)^{\frac{1}{3}}\left[\sum\int v^{-3}(p,N)\frac{d\Omega}{4\pi}\right]^{\frac{1}{3}} \qquad (4.8)$$

(h being Planks constant, k Boltzmanns constant and v(p,N) the mode velocity). Table 4.6 lists γ_0^{el}, γ_∞^{el} and θ_D^{el} for CdTe as well as other zincblende compounds and diamond type elements. When calculating $\gamma^{el}{}_0$, $\gamma(p,N)$ and v(p,N) were calculated from the SOEC extrapolated to 0K using the temperature derivatives listed in table 4.3. The room temperature pressure derivatives of the SOEC were used, even though the SOEC themselves were extrapolated to absolute zero; it is assumed that there are no fourth order effects, and that the pressure derivatives are temperature independent. It should be noted that for some of the materials listed, the Debye temperature is comparable or much larger than room temperature, and so γ_∞^{el} is not the true high temperature limit. Details of the numerical computation are given in appendix I.

γ^{el} is a measure only of the contribution of the zone centre acoustic modes to the anharmonicity, whereas γ^{th} takes into account contributions from both acoustic and optic branches. At low temperatures, only the zone centre acoustic phonons corresponding to the long wavelength limit are excited; of these modes, the TA branches are characteristically low in energy, a feature common in zincblende structures, and these tend to dominate the vibrational anharmonicity at low temperatures. At higher temperatures, LA and TA modes further into the zone, as well as optic modes, contribute more and more to the

anharmonic behaviour. Figures 4.6(a-c) illustrate this progressive excitation. They show the energy distribution over the phonon spectrum for temperatures of 4K, 54K and 304K calculated directly from the density of states due to Kushwaha and Kushwaha (1980). The zone centre optic mode and the zone boundary acoustic mode frequencies are marked by dotted lines. These figures show quite clearly how at low temperatures, all the energy is associated with the acoustic phonons; figure 4.6a shows negligible energy associated with the optic modes at all. However, the optic modes become more excited with an increase in temperature, and at relatively low temperatures ($T \sim \theta_D$), the optic modes are already showing a considerable excitation (figure 4.6b). At room temperature, both acoustic and optic modes are equally excited (figure 4.6c).

From equation (2.12), the high temperature thermal gamma was calculated for CdTe as 0.363, taking the room temperature values of C_P (Rusakov, Vekilov and Kadyshevich 1971) and α (Browder and Ballard 1969) as 105.5 $JKg^{-1}K^{-1}$ and 5.3×10^{-6} K^{-1} respectively.

The negative $\gamma^{el}{}_0$ is due to the dominant behaviour at low temperatures of the low energy shear acoustic modes, whose mode Gruneisen parameters are negative as shown in figure 4.5. These mode gammas reflect the soft zone centre TA phonons, which are directly related to the negative hydrostatic pressure derivatives of the two shear moduli $(C_{11}-C_{12})/2$ and C_{44}. The negative low temperature gammas suggest that the thermal expansion of CdTe should become negative below a certain temperature which Novikova (1961) finds to be 71.5K; this agrees well

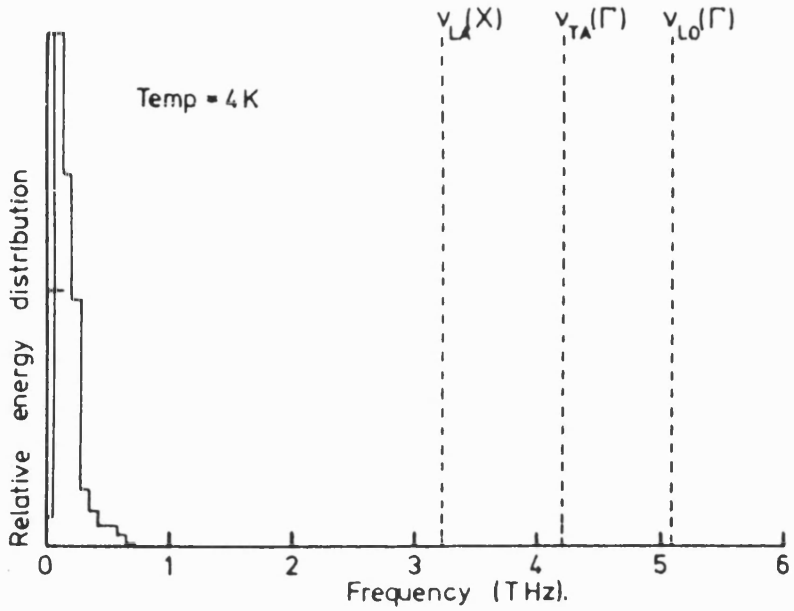

figure 4.6a

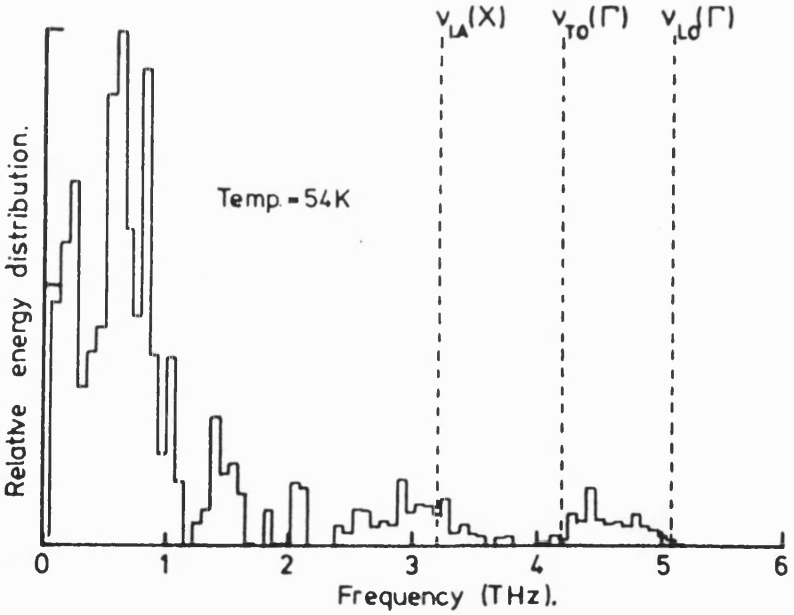

figure 4.6b

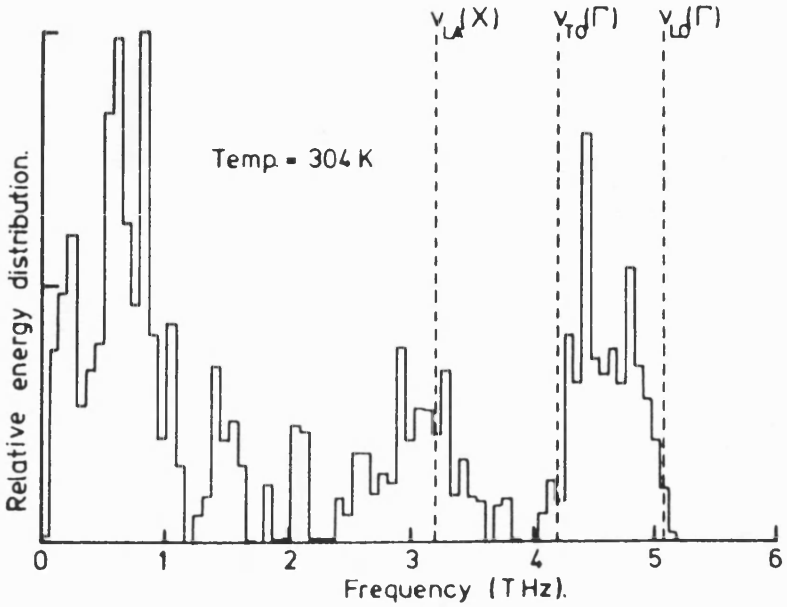

figure 4.6c

FIGURE 4.6a-c

Relative phonon energy distribution calculated from the density of states given by Kushwaha and Kushwaha (1980) for CdTe at various temperatures (a)-(c). LA, LO and TO phonon frequencies at the X and Γ points are indicated by dotted lines.

with the trends shown by other (II-VI) zincblende compounds with higher ionicities, e.g. ZnSe, HgSe and HgTe, all of which show negative thermal expansions below certain temperatures, and all have negative low temperature Gruneisen parameters. Again this supports the suggestion that the anharmonicity at low temperatures is dominated by the zone centre TA phonons.

In the high temperature limit, the existance of a negative γ_{∞}^{el} for CdTe is similar to HgSe, which has an unusually large negative room temperature acoustic gamma as shown in table 4.6. Two observations can be made from this. The first is that even at a temperature considerably higher than the Debye temperature, the TA gammas are sufficiently large enough to still dominate the elastic behaviour of CdTe. Secondly, since the thermal expansion, and hence the thermal Gruneisen gamma of CdTe are positive at room temperature, a large contribution by the optic modes and/or acoustic phonons further out toward the zone boundary must give a significant contribution to the thermal properties; as figure 4.6c shows, at room temperature all the phonon modes are considerably excited, and some or all of these modes must have positive mode Gruneisen parameters associated with them in order to produce the observed anharmonic effects.

4.5 DISCUSSION OF SOFT MODES AND THE STABILITY OF THE ZINCBLENDE STRUCTURE.

Soft modes are often associated with instabilities of the crystal structure, and are thought to be the mechanism by which pressure induced phase transitions occur. The long wavelength acoustic mode Gruneisen parameters arise only from the anharmonicity of acoustic modes close to the Brillouin zone centre. Negative values of the Gruneisen parameters for long wavelength acoustic modes imply a softening of such modes with increasing pressure and hence provide an indication of instability of the structure under pressure. Miller *et al* (1981a) have shown that the long wavelength shear mode acoustic gamma of HgTe become more negative as the phase transition pressure is approached. Consideration of the soft shear mode behaviour of these zincblende compounds, coupled with the ideas of the VFF model, gives considerable weight to the argument that it is the TA phonon modes that provide the main driving mechanism for the densification phase transitions. Ultrasonic data of the type presented here can only give information about the zone centre acoustic phonons, and nothing is known about the behaviour of the acoustic dispersion curves further out into the zone as a function of pressure. However, these data for CdTe do support the present ideas and trends associated with zincblende structures, showing that the zone centre acoustic phonons play an important role in the vibrational behaviour of these tetrahedrally coordinated compounds.

CHAPTER 5

ACOUSTIC MODE VIBRATIONAL ANHARMONICITY OF PbSe AND OTHER (IV–VI) COMPOUNDS

CHAPTER 5

ACOUSTIC MODE VIBRATIONAL ANHARMONICITY OF PbSe AND OTHER (IV-VI) COMPOUNDS.

5.1 INTRODUCTION.

The ten electron (IV-VI) compounds crystallise in three different but closely related structures, namely cubic, orthorhombic or rhombohedral. The lead chalcogenides and SnTe have the rocksalt structure. Littlewood (1980) and Enders (1983,1984a,1984b) have shown that these salts are predominantly covalent in nature, despite their high ionicities, the bonding being due to the unsaturated (resonant-like) p-valence orbitals, the full s states giving no contribution to the bond. The large p-state electronegativity difference gives rise to a polarisation of the bond, and this has the effect of opening up a small gap in the electronic spectrum at the L point. Thus these materials tend to be narrow gap semiconductors, and in consequence find important uses as infrared lasers and detectors.

The cubic structure of the lead chalcogenides is stable down to absolute zero, whereas SnTe undergoes a phase transition to the rhombohedral, arsenic type structure. In order for this transition to occur, it is necessary to produce sp hybrids to realise the rhombohedral structure. In the heavy lead chalcogenides, the relativistic mass enhancement causes a large energy gap between the s- and p-states. Hence it is difficult to promote an electron

from the lower energy s-state to the p-states, preventing the formation of the sp hybrid; the cubic structure remains stable. For the lighter SnTe, however, the energy difference is sufficiently small to allow such a transition (Littlewood 1980). The instability of this resonant p-valence bonded structure is reflected by the phonon spectra (Littlewood 1980, Enders 1983,1984a,1984b, Nakamshi and Matsubara 1980, Kawamura 1980). Inelestic neutron scattering experiments have evidenced softening of the TO phonon mode polarised along the [111] direction at the Γ point for SnTe. From measurements of the heat capacity, an assessment of the influence of mode softening upon the thermal properties of SnTe has been made, and strong temperature dependencies below 20K of the Debye temperature and the thermal Gruneisen parameter have been attributed to the thermal excitation of the low lying TO mode.

Enders (1984b) has shown that this softening of the TO mode alone is not sufficient to account for the phase transition, and that the interaction between this soft optic mode and the acoustic modes must be considered. Mode softening of the long wavelength acoustic modes has been observed in some of these materials from measurements of the effects of hydrostatic pressure and temperature on the SOEC, similar to the soft modes in zincblende structures discussed in the presvious chapter, and acoustic mode softening has been observed in GeTe-SnTe alloys near the cubic-rhombohedral phase transition (Seddon *et al* 1975). Thus it appears that the vibrational anharmonicity of the acoustic modes close to the zone centre is an important factor in determining the stability of the rocksalt structure.

In this chapter, the SOEC and their hydrostatic pressure derivatives of PbSe measured using the techniques previously descibed are presented (section 5.2). In section 5.3 the results are discussed in comparison with similar data for PbTe, PbS, SnTe and the alloy $Ge_{0.08}Sn_{0.92}Te$. Section 5.4 deals with the Gruneisen parameters, and in particular the mode Gruneisen parameters and the effect of the nearest neighbour repulsive forces upon them. Finally section 5.5 considers briefly the results presented with particular relevance to the cubic-rhombohedral phase transition.

5.2 EXPERIMENTAL RESULTS.

A single crystal of PbSe, grown by vapour phase deposition by N. Schäl at the Fraunhofer Institut fur Physikalische Messtechnik, was cut into a two-fold slice, the parallel faces being of type [110]. Orientation of the crystal was made simple by the fact that this particualar material cleaves easily along the [001] planes. Once prepared, the ultrasonic velocities in the [110] direction together with hydrostatic pressure derivatives were measured as described in chapter 3.

5.2.1 Ultrasonic velocities and SOEC.

Table 5.1 gives the three mode velocities that can be propagated in the [110] direction for PbSe, together with

TABLE 5.1

N	U	V (ms^{-1})	ρV^2 ($x10^{10}$ Nm^{-2})
[001]	[001]	3801.5 ± 1.3	11.772 ± 0.008
[110]	[110]	3164.9 ± 2.1	8.164 ± 0.011
[110]	[1$\bar{1}$0]	2529.7 ± 1.7	5.215 ± 0.007
[110]	[001]	1371.9 ± 0.9	1.534 ± 0.002

Ultrasonic velocities of the pure modes measured in PbSe.

the calculated values of $\rho_0 V^2$. These lead to the values of SOEC given in table 5.2 in comparison with other workers and also similar data for PbTe, PbS and SnTe. The results given in table 5.2 resolve one outstanding problem concerning the elastic properties of PbSe in that they substantiate the work of Lippman *et al* (1971) who obtained a set of elastic constants which disagree entirely with those measured by Chudnikov and reported by Rabii (1968). The elastic stiffness constants conform to the trends common to those of other rocksalt structure (IV-VI) compounds.

5.2.2 Hydrostatic pressure derivatives of the SOEC.

The changes in natural wave velocity induced by the application of hydrostatic pressure to PbSe are shown in figure 5.1. The pressure derivatives of the elastic constants (table 5.3), obtained from these results, follow the same pattern $\partial C_{11}/\partial P > \partial C'/\partial P > \partial C_{44}/\partial P$ observed for other (IV-VI) compounds (Miller *et al* 1981b). A nearly zero, or even a slightly negative value of $\partial C_{44}/\partial P$ is a common feature of rocksalt structured crystals, and the small negative value of $\partial C_{44}/\partial P$ found for PbSe shows that application of pressure produces slight softening of the N[110], U[001] shear mode at the long wavelength limit.

5.2.3 Temperature dependence of the SOEC of SnTe.

Figure 5.2(a,b) shows the two elastic shear moduli (C_{11} and C_{44}) measured in the [001] direction for SnTe as a

TABLE 5.2

	Density (Kgm^{-3})	C_{11}	C_{12}	C_{44}	$C'=\frac{1}{2}(C_{11}-C_{12})$	$B^s=\frac{1}{3}(C_{11}+2C_{12})$	ref.
PbSe	8150	11.783 ± 0.08	1.39 ± 0.02	1.553 ± 0.009	5.215 ± 0.007	4.85 ± 0.01	(a)
		12.37 ±0.05	1.93 ± 0.04	1.591 ± 0.005	5.22	5.41	(b)
		11.28	1.48	1.31	4.90	4.75	(c)
PbTe	8219	10.53 ± 0.02	0.70 ± 0.02	1.322 ± 0.001	4.91 ± 0.01	3.98	(d)
		10.80 ± 0.07	0.77 ± 0.08	1.343 ± 0.008	5.01 ± 0.08	4.11	(e)
PbS	7500	12.61 ± 0.02	1.62 ± 0.03	1.71 ± 0.02	5.50 ± 0.03	5.29 ± 0.03	(f)
SnTe	6383	10.43 ± 0.02	0.178 ± 0.03	1.133 ± 0.001	5.13 ± 0.02	3.59	(g)

References: (a) Present work; (b) Lippmann *et al* 1981; (c) Rabii 1968; (d) Miller *et al* 1981; (e) Houston *et al* 1968; (f) Peressada *et al* 1976; (g) Seddon *et al* 1975.

SOEC of (IV-VI) compounds at room temperature. Units are 10^{10} Nm^{-2}.

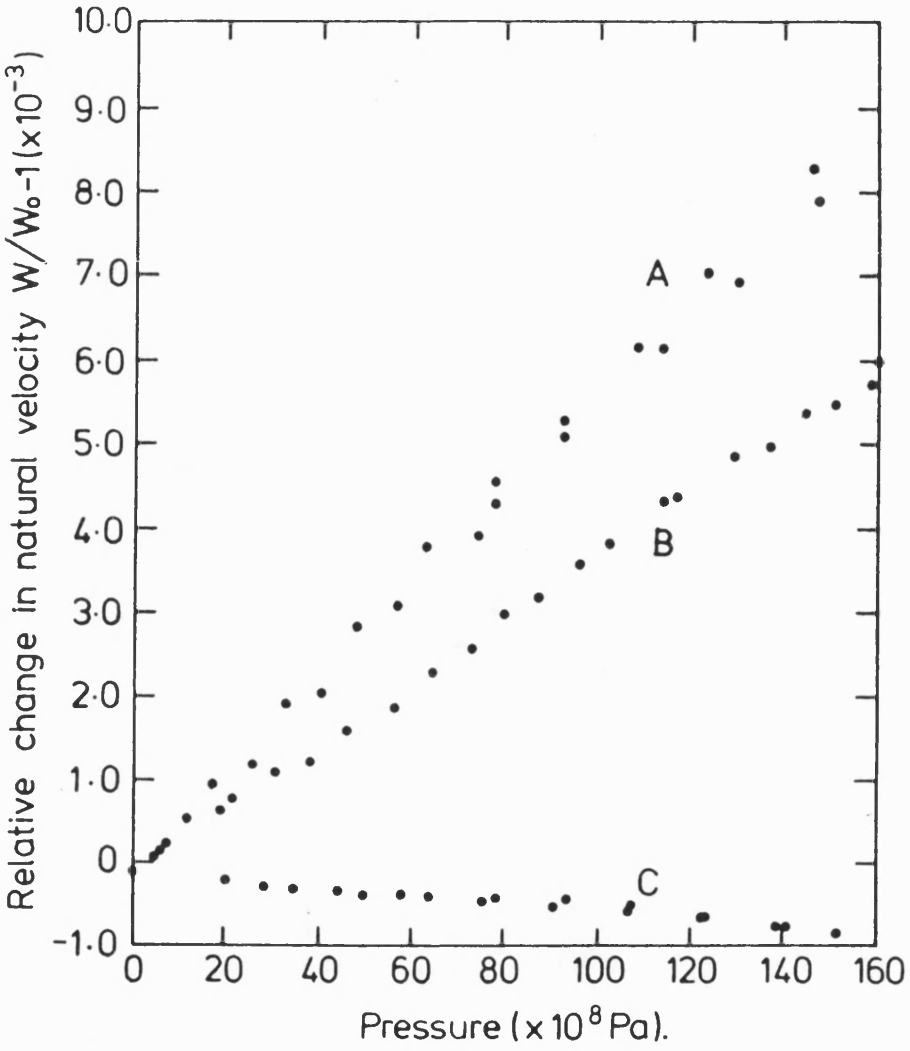

FIGURE 5.1

Relative change in natural wave velocity under hydrostatic pressure for PbSe. The modes are:

A N[110], U[1$\bar{1}$0];
B N[110], U[1$\bar{1}$0];
C N[110], U[001];

where N and U are the propagation and polarisation vectors respectively.

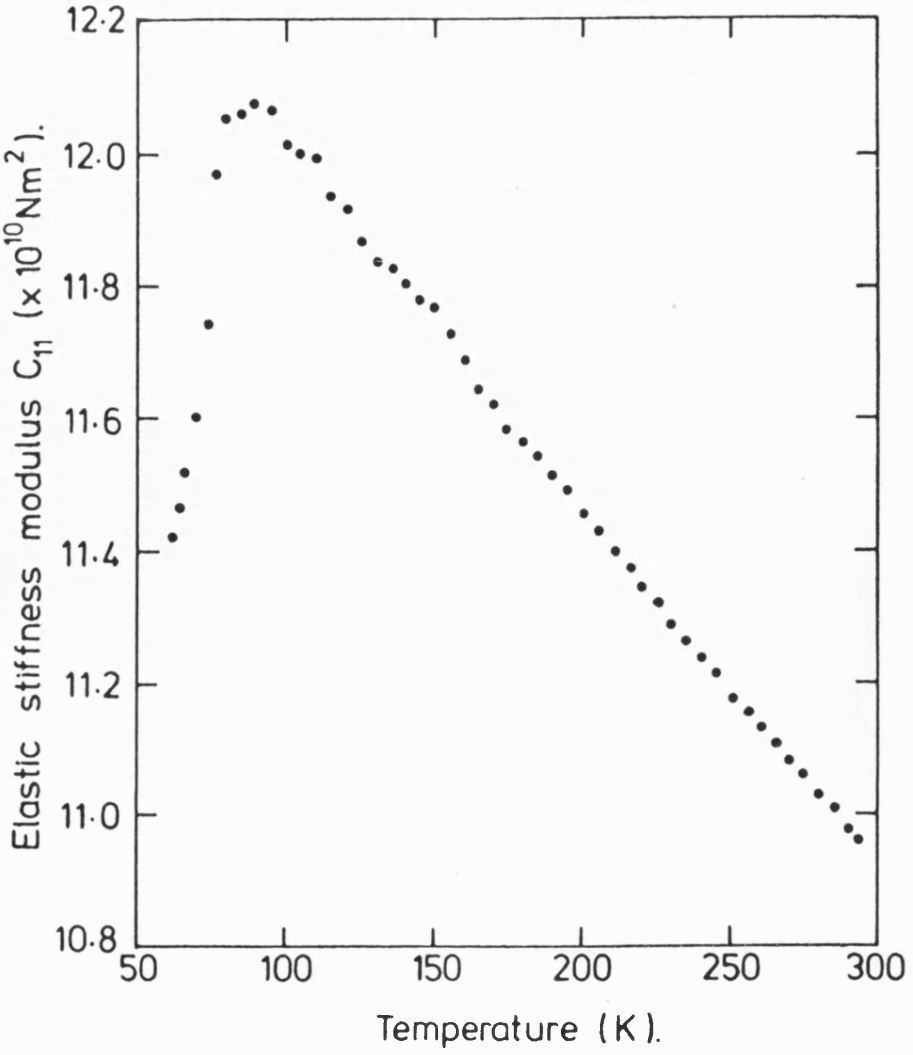
12·2
12·0
11·8
11·6
11·4
11·2
11·0
10·8
Elastic stiffness modulus C_{11} ($\times 10^{10} Nm^2$).
50
100
150
200
250
300
Temperature (K).

figure 5.2a

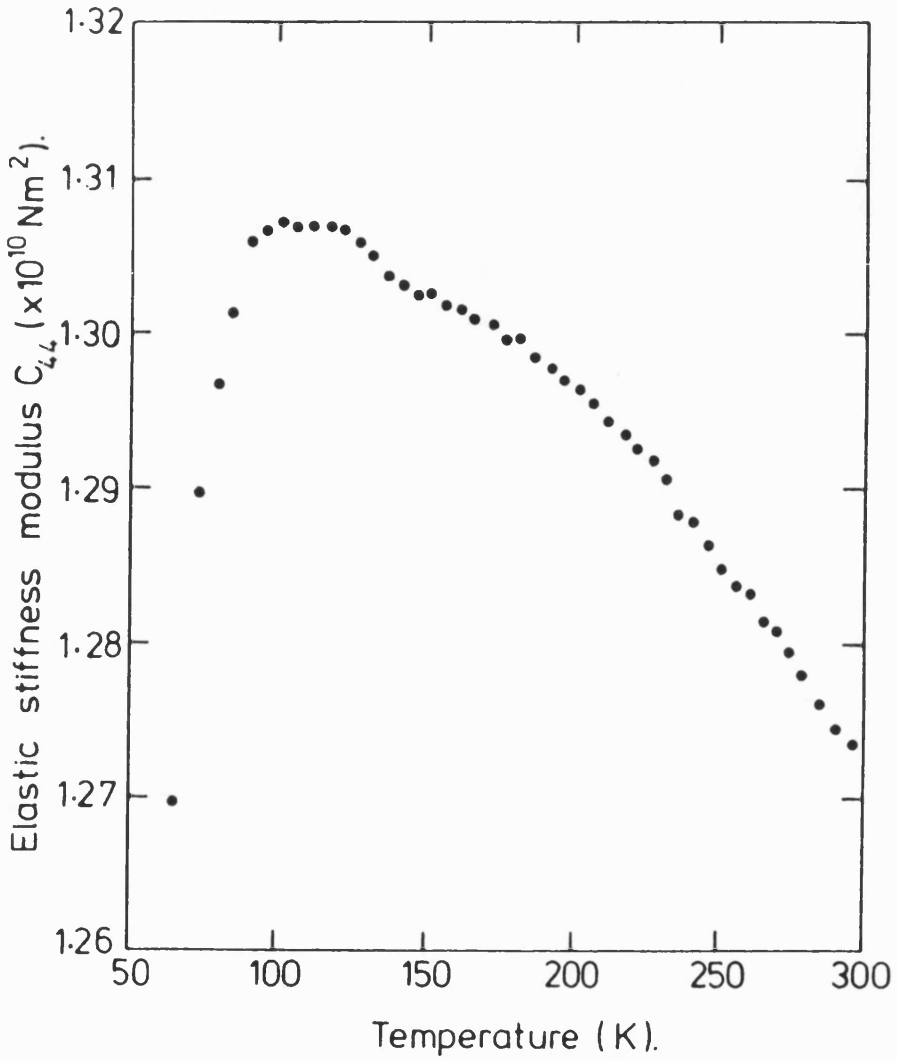

figure 5.2b

FIGURE 5.2

Change in the elastic stiffness moduli, (a) C_{11} and (b) C_{44} as a function of temperature for SnTe.

TABLE 5.3

	PbSe	PbTe	PbS	SnTe
$\partial C_{11}/\partial P$	13.87 ± 0.22	13.40 ± 0.13	14.84 ± 0.02	13.99 ± 0.15
$\partial C_{12}/\partial P$	0.39 ± 0.29	1.00 ± 0.14	2.00 ± 0.20	1.48 ± 0.16
$\partial C_{44}/\partial P$	-0.0048 ± 0.006	0.190 ± 0.004	-0.0097 ± 0.0008	0.140 ± 0.002
$\partial C'/\partial P$	6.74 ± 0.25	5.93 ± 0.06	6.42 ± 0.20	6.25 ± 0.07
$\partial B^S/\partial P$	4.88 ± 0.21	5.13 ± 0.14	6.28 ± 0.20	5.65 ± 0.16
$C_1=C_{111}+2C_{112}$	-228	-178	-264	-172
$C_2=C_{144}+2C_{166}$	-16	-15.2	-17	-13.4
$C_3=C_{123}+2C_{112}$	7.8	-2.6	-17.5	-5

The hydrostatic pressure derivatives of the SOEC and three combinations of the TOEC (in units of 10^{10} Nm^{-2}) for (IV-VI) compounds. Data for PbTe and SnTe is taken from Miller *et al* 1981, and for PbS from Lippmann *et al* 1981.

TABLE 5.4

	γ_0^{el}	γ_∞^{el}	γ_{298}^{th}	θ_D^{el}
PbS	0.93	1.75	2.64	164.0
PbSe	0.92	1.66	2.00	146.1
PbTe	0.91	1.53	2.01	129.5
SnTe	0.79	1.45	1.83	142.6
$Ge_{0.08}Sn_{0.92}Te$	0.92	1.51	-	151.6
NaCl	1.34	1.66	1.6	241.5

Comparison of the mean long wavelength acoustic mode Gruneisen parameters in the low (γ_o^{el}) and high (γ_∞^{el}) temperature limits, together with the thermal Gruneisen parameter (γ_{298}^{th}) and elastic Debye temperature (θ_D^{el}) at 298K for the (IV-VI) compounds.

function of temperature down to the phase transition (the data were kindly made available By Prof. G Saunders in a private communication). A positive value of $\partial C_{ij}/\partial T$ indicates a soft mode behaviour, and such behaviour is observed in SnTe, both C_{11} and C_{44} reducing rapidly with decreasing temperature as the phase transition is approached. Elastic constant data obtained on GeTe-SnTe alloys shows (Miller *et al* 1981b) that below the phase transition the shear moduli increase with decreasing temperature. The data presented in figure 5.2 shows that SnTe has a similar acoustic mode softening behaviour. Hall effect measurements show that this SnTe crystal is p-type with a carrier concentration of 4×10^{20} cm^{-3}. The transition temperature T_c for SnTe decreases strongly with increasing carrier density. Resistance anomaly measurements indicate that a sample having a hole concentration of 4.2×10^{20} cm^{-3} had a T_c of 53.5K, while that determined by Raman scattering was 64K (Sugai *et al* 1977). The ultrasonic data are consistent with T_c for our sample being in this range of temperature but the ultrasonic signals became too weak in the vicinity of the transition for an accurate determination.

5.3 ELASTIC BEHAVIOUR OF THE (IV-VI) COMPOUNDS.

For cubic crystals to be stable, C_{44} must be greater than zero. Since C_{44} is small for the rocksalt structure, there is a tendency for these materials to be close to the modified Born stability requirement (see chapter 4) that C_{44}/B should not reduce below a crtitical value (0.22 for PbTe, 0.25 for SnTe, Miller *et al* 1981b), when

a complex macroscopic shear assists the transformation to the orthorhombic structure. It is interesting to note that Littlewood (1980) has predicted that PbSe should undergo a cubic to orthorhombic phase trasition at a hydrostatic pressure of 42 x 10^8 Pa; assuming linearity under pressure of C_{44}/B, the present measurements of $\partial C_{44}/\partial P$ and $\partial B/\partial P$ (table 5.3) show that at this pressure C_{44}/B would become 0.22 for PbSe - the same value at which PbTe transforms. A search for a phase transtion in the neighbourhood of $40x10^8$ Pa would be well worthwhile.

Three combinations C_1, C_2 and C_3 of the third order elastic constants can be obtained from the hydrostatic pressure derivatives of the SOEC using

$$\frac{\partial C_{44}}{\partial P} = - \frac{(C_{11}+2C_{12}+C_{44}+C_{144}+2C_{166})}{(C_{11}+2C_{12})}$$

$$\frac{\partial C'}{\partial P} = - \frac{(3C_{11}+3C_{12}+C_{111}-C_{123})}{2(C_{11}+2C_{12})}$$

$$\frac{\partial B}{\partial P} = - \frac{(C_{111}+6C_{112}+2C_{123})}{3(C_{11}+2C_{12})} \qquad (5.1)$$

Results are given in table 5.3. To obtain all six independent TOEC would require measurements of the changes in the ultrasonic mode velocities induced by uniaxial stress (see chapters 3 and 4). Unfortunatally this was not experimantally possible with the present sample of PbSe due to the severly degraded echo train which was obtained in the [100] direction, perpendicular to the cleavage planes. Such measurements have been

carried out, however, for PbTe with the results: C_{111}=-18.5; C_{112}= 0.35; C_{123}=-0.97; C_{144}= 0.44; C_{166}= 0.98; C_{456}= 0.12 in units of 10^{11} Nm^{-1} (Miller *et al* 1981b). Hence C_{111} is much the larger TOEC for PbTe, and inspection of the values of C_1, C_2 and C_3 in table 5.3 indicates that this is probably also the case for PbSe, PbS and SnTe.

5.4 VIBRATIONAL ANHARMONICITY IN THE LONG WAVELENGTH; ACOUSTIC GRUNEISEN PARAMETERS.

As with the zincblende compounds discussed in chapter 4, the vibrational anharmonicity of the long wavelength acoustic modes can be further quantified by calculating the mode Gruneisen parameters, as well as the mean elastic and thermal Gruneisen gammas (see chapter 2). In this section, the anharmonicity will be discussed in terms of these Gruneisen parameters, and in order to gain a greater understanding of the nature of the interatomic forces in these ten electron rocksalt structured compounds, the effect of the nearest neighbour repulsive forces on the TOEC, calculated using the Born-Meyer potential model, will be discussed first.

5.4.1 The Born-Meyer potential model and TOEC.

Thakur (1980) has developed a model for the TOEC of rocksalt structured compounds which utilises spherically

symmetric pairwise forces of the type found in highly ionic materials, such as NaCl. This model is based on a Born-Meyer type interaction potential which can be written as

$$\Phi_{\mu\nu}(r) = -(Z_\mu Z_\nu e^2/r) + \psi_{\mu\nu}(r) \qquad (5.2)$$

where e is the electronic charge, Z_μ and Z_ν the charges on the ions and r the ionic seperation. The repulsive potential $\psi_{\mu\nu}(r)$ is used in the exponential form

$$\psi_{\mu\nu}(r) = A\exp(-r/\rho) \qquad (5.3)$$

where ρ is a characteristic distance of the material. Thakur (1980) has divided contributions to the TOEC into an attractive (coulombic) part and a repulsive part. Applying this model to SnTe and the alloy $Ge_{0.08}Sn_{0.92}Te$, Miller *et al* (1981) have shown that C_{111} is by far the largest TOEC because the nearest neigbour (anion-cation) repulsive forces dominate it (and in turn the hydrostatic pressure dependences of $\partial C_{11}/\partial P$ and $\partial B/\partial P$) but are not involved in the other TOEC to any marked extent. This has important consequences on the acoustic mode Gruneisen parameters and hence the thermodynamic properties of the (IV-VI) compounds.

5.4.2 Acoustic mode Gruneisen parameters.

Figure 5.3(a-c) shows the directional dependence of the acoustic mode Gruneisen parameters of PbSe (figure 5.3a) and PbS (figure 5.3b), together with those for NaCl (figure 5.3c) for comparison. The orientational dependences of the $\gamma(p,N)$ for all these (IV-VI) compounds show similar behaviour, which has been explained for PbTe and SnTe on the basis of the proponderance of contributions of nearest neighbour repulsive forces (Miller *et al* 1981). For PbSe (or PbS), consider for example the $\gamma(p,N)$ for modes propagated along the fourfold <001> axes. For the longitudinal mode $\gamma(p,N)$ is large and positive because k(p,N) (equation 2.28) is given by $(C_{111}+2C_{112})$, which is dominated by C_{111}, the largest TOEC due to the nearest neighbour repulsion, hence the frequencies of acoustic [001] longitudinal modes near zero wave vector are strongly volume dependent. However for the shear wave propagated along an <001> axis, k(p,N) is $(C_{144}+2C_{166})$ which is not influenced by nearest neighbour repulsive forces and is small. Hence $\gamma(p,N)$ for this mode is small and in fact slightly negative, which is not uncommon for rocksalt structure crystals (Miller *et al* 1981b). In general in the (IV-VI) compounds $\gamma(p,N)$ is quite large for those modes in which there is substantial contribution from the nearest neighbour repulsive forces, while those modes which do not involve this strong repulsion have small Gruneisen parameters which indicate a weak dependence of frequency upon crystal volume.

The Born-Meyer potential model is based on central

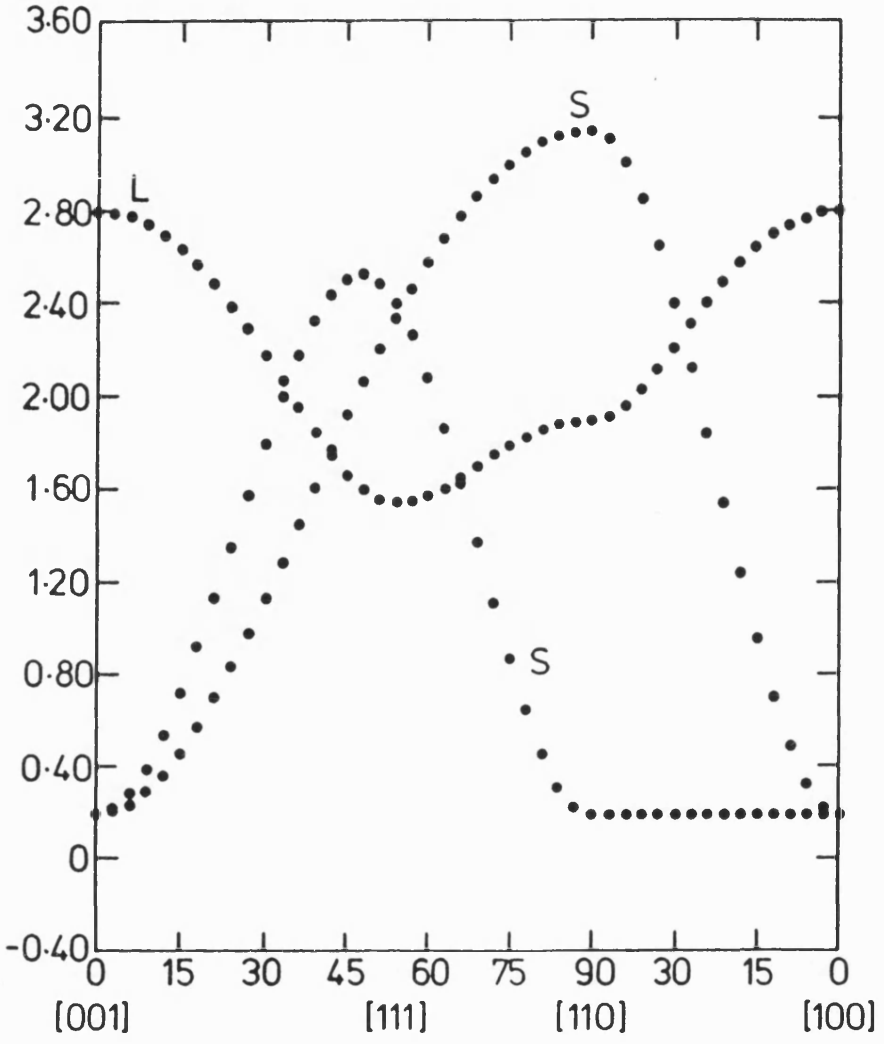
3·60
3·20
2·80
2·40
2·00
1·60
1·20
0·80
0·40
0
-0·40
L
S
S
0 15 30 45 60 75 90 30 15 0
[001] [111] [110] [100]
Mode propagation direction.

figure 5.3a

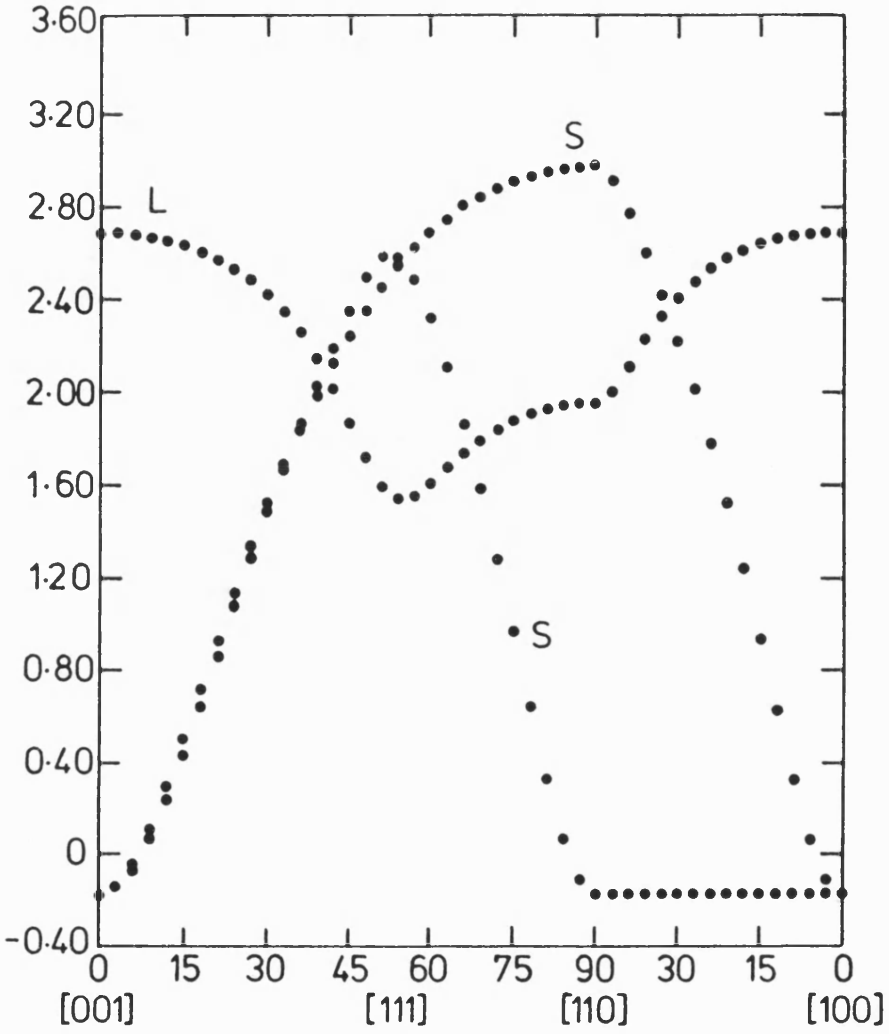
3·60
3·20
2·80
2·40
2·00
1·60
1·20
0·80
0·40
0
-0·40
L
S
S
0
15
30
45
60
75
90
30
15
0
[001]
[111]
[110]
[100]
Mode propagation direction.

figure 5.3b

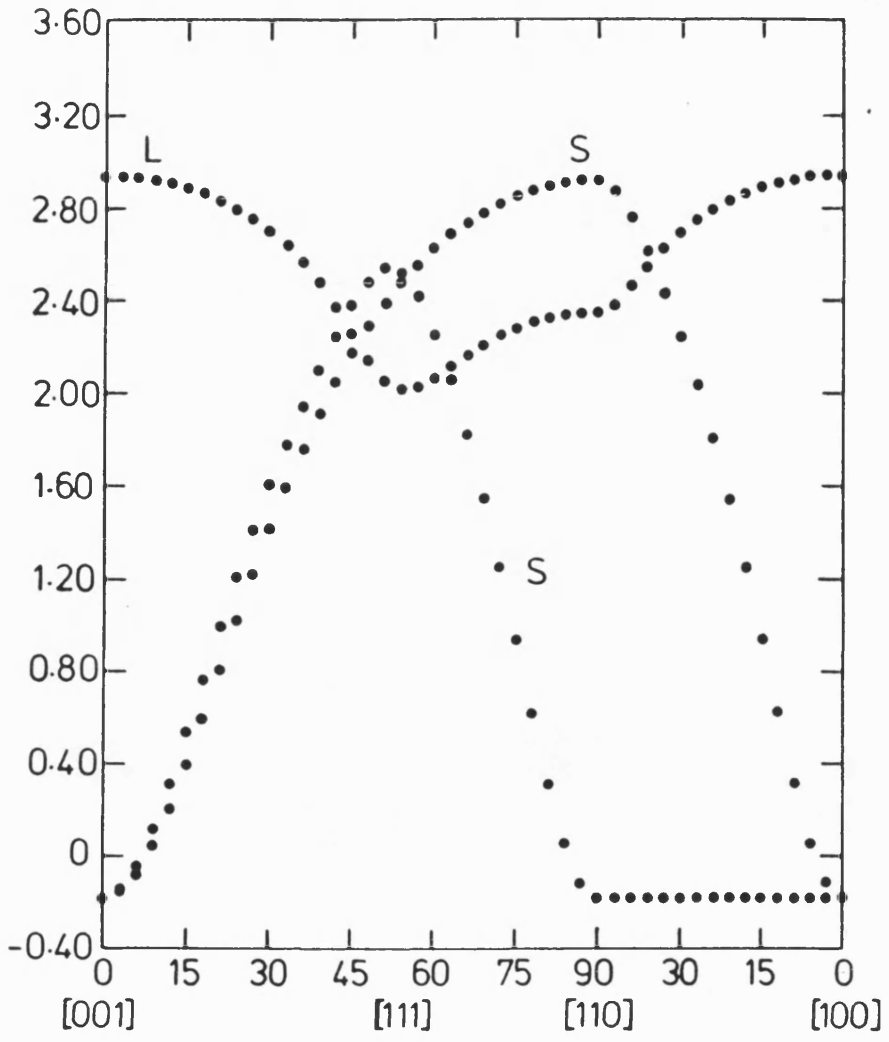

figure 5.3c

FIGURE 5.3

Mode Gruneisen parameters $\gamma(p,N)$ for longitudinal (L) and shear (S) modes, calculated as a function of mode propagation direction N in (a) PbSe, (b) PbS and (c) NaCl. For explanation of scale on horizontal axis see appendix I.

pair-wise forces, and is essentially an ionic model. The applicability of such a model to mixed ionic-covalent structures, such as the (IV-VI) compounds, must be limited and although it has shown quite conclusively that C_{111} is dominated by the nearest neighbour repulsive forces, it fails to predict other TOEC with any accuracy (Miller *et al* 1981b). The reason for this is clear; no account of the directional nature of the strongly covalent p-valence bonds is taken into account. However the similarity between the mode Gruneisen parameters for NaCl, for which one would expect the Born-Meyer model to be a good one, and those for PbSe and PbS is striking. This gives weight to the argument that the vibrational anharmonicity is strongly dependent upon the nearest neighbour repulsive forces. The orientational dependence of the acoustic mode Gruneisen parameters has a similar form for all rocksalt structure crystals.

5.4.3 Mean acoustic and thermal Gruneisen parameters.

The low and high temperature limits of the elastic Gruneisen parameters have been calculated using equations (2.32) and (2.33) respectively for the lead chalcogenides, SnTe, the alloy $Ge_{0.05}Sn_{0.92}Te$, as well as for NaCl for comparison (table 5.4). The thermal Gruneisen parameter was calculated using equation (2.12) and the room temperature θ_D from equation (4.8). The values of all three Gruneisen parameters listed are similar for all the compounds, those of SnTe being the smallest. The elastic Gruneisen parameter of the lead salts show an interesting trend; the low temperature

limit parameters are all similar with the a value of around 0.9, whereas the high temperature gamma shows a marked decrease with increasing interatomic distance r_o (increasing electronegativity). In the last subsection, it was pointed out that the mode Gruneisen parameters tend to be large and positive for these modes where C_{111} dominates and hence the effect is largely due to the nearest neighbour repulsive forces. By application of the Born-Meyer potential model, Thakur (1980) has shown that the repulsive (non-coulombic) part of C_{111} increases steadily with an increase in r_o. Thus γ_o^{el} shows a marked decrease with increasing r_o, corresponding to an increase in nearest neighbour repulsive contribution to C_{111}.

Knowledge of γ_o^{el} and γ_∞^{el} enables separation (at low or high temperatures) of the contributions of the long wavelength acoustic modes from those of other excited modes. The values of γ_o^{el} is smaller than γ_∞^{el} for each of the (IV-VI) compounds on account of dominance at low temperatures of γ_o^{el} by the low lying TA modes which have smaller values of $\gamma(p,N)$ than the LA modes (see figures 5.4,5,6). That the values of γ_o^{el} and γ_∞^{el} are somewhat smaller for SnTe than those of other (IV-VI) compounds is consistent with there being negative contributions from the soft TA modes in SnTe leading to a reduction in the mean acoustic Gruneisen parameters. The pronounced temperature dependence of both θ_D^{el} and γ^{th} for SnTe above 3K has been attributed to excitation of the very low-lying soft TO mode (Smith *et al* 1976). There is a deep minimum in the γ^{th} whcih suggests that the mode gamma for the soft TO mode is much smaller algebraically than that of the acoustic modes and may well be negative. This is consistent with the inference (Smith *et al* 1976)

from the measurements (Pawley *et al* 1966) of the soft TO mode frequencies that γ_{TO} could be large and negative (-55 to -65). The large decrease to a minimum at low temperatures in γ^{th} probably occurs when the temperature becomes large enough to excite the zone centre soft TO mode - the measured mode frequency of about $5x10^{11}$ s^{-1} (Pawley *et al* 1966) suggests that this mode excitation could occur as low as 5K (Smith *et al* 1976). Another characteristic of these compounds is that $\gamma^{th} > \gamma_{\infty}^{el}$ which carries the implication that the mode gammas $\gamma(p,N)$ of the other modes (acoustic modes not near the zone centre and optic modes) taken together have a higher mean than that of the zone centre acoustic modes. An exception would be the $\gamma(p,N)$ of the soft TO mode in SnTe and it's contribution may be repsonsible in part for this compound having a smaller γ^{th} than those of the other lead chalcogenides.

5.5 DISCUSSION OF STRUCTURAL STABILITY OF THE (IV-VI) COMPOUNDS.

The cubic to rhombohedral phase transition in SnTe results from a large electron-TO phonon coupling (Littlewood 1981, Enders 1983,1984a,1984b), and the softening of the long wavelength TO phonon propagating in the [111] direction is considered to be the dominant driving mechanism. As the phase transition is approached from above, the TO mode couples to the TA modes near the zone centre; this causes the reduction in the shear moduli observed in SnTe (figure 5.2) and $Ge_{0.08}Sn_{0.92}Te$ alloys (Seddon *et al* 1975). Enders (1984b) has pointed

out that for a complete model of the phase transition, account must be taken of the interaction between acoustic and optic modes; clearly the acoustic vibrational anharmonicity in these materials must play an important role in their structural stability.

In the previous section, the Born-Meyer model was used to show that the majority of the anharmonicity in the (IV-VI) compounds is predominantly due to nearest neighbour repulsive interactions. Thus we can infer that the stability of the rocksalt structure is also due to these nearest neighbour repulsive forces. This is analogous to the situation discribed in chapter 4 concerning the zincblende structured compounds, where again the anharmonicity of the long wavelength acoustic modes was shown to be of great importance in the stability of the tetrahedral structure. The Born-Meyer model is however an ionic one, whereas the (IV-VI) compounds have been shown to be extremely covalent in nature, despite their large ionicities. Even though the half filled resonant p orbital bonds show a marked degree of directional character, their highly polarised nature may be the reason why the ionic Born-Meyer model appear to give such good results for the nearest neighbour interactions, and hence explain the dominance of C_{111} in dictating the long wavelength acoustic mode vibrational anharmonicity.

CHAPTER 6

HOT ELECTRONS IN SEMICONDUCTORS

CHAPTER 6

HOT ELECTRONS IN SEMICONDUCTORS.

6.1 INTRODUCTION.

At low temperatures, non-ohmic behaviour can be observed in semiconductors due to the mobility becoming field dependent; this phenomenon is generally attributed to *hot electron effects*. As an introduction to the measurement of nonlinear current-voltage characteristics in cadmium mercury telluride alloys ($Cd_xHg_{1-x}Te$), this chapter will deal briefly with the phenomenological physics of hot electrons in semiconductors. Section 6.2 will qualitatively describe how nonlinear transport occurs in semiconductors; the important concepts of momentum and energy relaxation, as well as the various electron scattering mechanisms will be briefly outlined, and the validity of the single electron temperature model which is often used to quantify these effects discussed (Hess 1980, Seeger 1982). The last section (6.3) deals with the application of hot electron effects to mm-wave and far infrared detection, and a review of the theory of hot electron bolometers due to Kogan (1963b) is given.

6.2 PHENOMENOLOGICAL PHYSICS OF HOT ELECTRONS IN SEMICONDUCTORS.

Interest in hot electron effects began in 1951 with the experiments of Ryder and Shockley (reported by Ryder 1953), who measured the nonlinear current-voltage characteristics of semiconductors. When an electric field is applied to a semiconductor, the electrons are accelerated in the opposite direction to the field, gaining additional energy and momentum. This energy is quickly lost to the lattice by inelastic collisions with phonons, and the directed momentum randomised. At moderate values of electric field, the rate of energy loss is sufficiently high not to allow the electrons to increase their mean energy much above the thermal value. Since mobility is generally a function of electron energy, the conductivity is field independent, and Ohm's law is obeyed. This is not necessarily the case at higher fields; the rate of energy gain from the field is now greater than the rate of energy loss, and the electrons *warm up* until a new steady state condition is established when once more the rates of energy gain and energy loss are balanced. The mean energy of the electrons is now field dependent, and therefore so is the mobility; this leads to non-ohmic behaviour.

At room temperature, the electron lattice interaction is very strong due to the large numbers of inelastic collisions with optic phonons. For this reason, high electric fields ($\sim 10^4$ Vcm^{-1}) are generally required to produce this nonlinear behaviour, and so hot electron phenomena are often referred to in the literature as *high field effects*. However, at low temperatures ($T << \theta_D$) the

number of thermally excited optic phonons is very small; the collision rate is considerably reduced and the electron-lattice coupling is weakened. This leads to a much smaller rate of energy loss by the electrons, and nonlinear behaviour can now be observed even at relatively low fields.

The nature of the nonlinear behaviour due to hot electron effects is dependent upon how the electron mobility and energy loss rate vary with electron energy; these are in turn governed by the dominating scattering mechanisms in the semiconductor. For this reason, the following subsections discuss the more important scattering mechanisms, and how they affect the dependence of the momentum relaxation time on electron energy.

6.2.1 Mobility and momentum relaxation.

Before discussing specific scattering mechanisms, the momentum relaxation time (τ_m) will be defined in order to distinguish it from the energy relaxation time (τ_ϵ), which will be introduced later. The mobility (and hence the conductivity) is governed by the momentum relaxation time via the equation

$$\mu = e\tau_m/m^*, \qquad (6.1)$$

where m^* the electron effective mass and e the electronic charge. τ_m is defined from the relaxation time approximation of the Boltzmann transport equation;

$$\frac{df(v)}{dt} + \frac{f(v) - f_0(v)}{\tau_m(v)} = 0 \qquad (6.2)$$

where f(v) is the electron distribution as a function of the electron velocity v. f(v) can be considered to consist of a symmetric part (the equilibrium distribution $f_o(v)$), and an antisymmetric part which is due to any directed velocity gained from an external force, such as an E field. Therefore, the relaxation time defines the rate at which any directed velocity (momentum) is randomised by collisions back to $f_o(v)$, which in most cases can be considered a Maxwell-Boltzmann type distribution.

The relaxation time is generally most dependent on the electron energy; the dependence of τ_m on lattice temperature is usually only through the occupancy of phonon states, and is invariably complex in nature. The relationship between τ_m and electron energy (ϵ) is often approximated by a power law of the form

$$\tau_m \propto \epsilon^r \qquad (6.3)$$

where r is within the range ±2. In the next subsection, the important scattering mechanisms in semiconductors will be discussed, and where possible a value of r given, hence showing the type of deviation from Ohm's law that

would be expected for hot electrons.

6.2.2 Scattering mechanisms in semiconductors.

Electron scattering mechanisms can generally be divided in to four main types: (i) electron-electron scattering, (ii) scattering by phonons, (iii) scattering by impurities, (iv) scattering by lattice defects. Since electron-electron scattering does not change the total momentum of the electron gas, it has little effect on the mobility, but does have important consequences in the application of the electron temperature model, which will be dealt with later. Scattering by defects (such as dislocation scattering) will not be discussed here as the crystals will be assumed to be perfect. Therefore this section will only concentrate on phonon and impurity scattering.

The types of scattering which could be important are:

1) ionised impurity scattering,
2) acoustic deformation potential scattering,
3) piezoelectric scattering,
4) optical deformation potential scattering,
5) polar optical scattering.

Apart from ionised impurity scattering, these mechanisms are all due to phonons. At low temperatures, ionised impurity scattering and scattering by acoustic phonons dominate, since the number of optic phonons is minimal.

Therefore, since the measurements concerned with here are at liquid helium temperatures, only a brief description of the first three types of scattering need be given.

1) Ionised impurity scattering.

In this case the electrons are considered to undergo elastic collisions with ionised impurity atoms in the semicondutor, the interaction being due to the coulombic potential of the ionised impurities (Conwell and Weisskopf 1950, Brooks and Herring 1955). This type of scattering yields a value of r in (6.2) of +3/2, and so as the electrons are heated up by the field, the mobility (and hence conductivity) should increase, leading to a positive deviation from Ohm's law.

2) Acoustic deformation potential scattering.

Even though this is a phonon interaction, which should be treated as an inelastic collision, it is the long wavelength acoustic phonons with which the electrons interact; these have vanishly small frequencies and hence very little energy associated with them. Thus acoustic phonon scattering is generally treated as if it were elastic. The scattering of electrons by acoustic waves requires the theory of the *deformation potential* put forward by Bardeen and Shockley (1950); a long wavelength LA phonon causes a macroscopic strain of the crystal lattice, which in turn causes a shift in the conduction band edge in the electronic spectrum, scattering the electrons into different Bloch states. In this case, r has the value of -1/2, producing a negative deviation from Ohm's law. The interaction is

short range, however, and the electrons are only weakly scattered.

3) Piezoelectric scattering.

In polar semiconductors with no centre of symmetry (such as those zincblende type semiconductors discussed previously, as well as CMT alloys), the LA phonons can produce an electric polarisation with which the electrons interact. Unlike the deformation potential scattering, this electrostatic interaction is long range but again is generally treated as elastic. In practice, piezoelectric scattering is difficult to observe since at high temperatures polar optical phonon scattering is by far the more important mechanism, and at low temperatures the purity of these binary polar semiconductors is such that ionised impurity scattering dominates. However, it may be that piezoelectric scattering is the major energy loss mechanism at low temperatures, and this is indeed the case in InSb (Cronin, 1977), and could also true of CMT, due to the very polar nature of this alloy. Because piezoelectric scattering can be considered to be elastic and independent of wave vector (in the limit of infinitely long waves, q=0), then a momentum relaxation time can be defined, r having the value of +1/2. Hence a positive deviation from Ohm's law would be expected for this type of scattering.

Even though at low temperatures ($T<<\theta_D$) there are no thermally excited optic phonons with which the electrons can interact, it is possible for hot electrons to have sufficient energy ($>\hbar\omega$) to emit one. This obviously has a

great influence on the energy loss rate; electrons gain momentum from the field until they possess sufficient energy to emit an optic phonon, at which point they are scatterd back to the Brillouin zone centre, losing most of their energy. Thus the energy loss rate becomes very high for the most energetic electrons, and a further increase in electron energy as the field is increased becomes impossible. This may lead to a an region of negative differential resistance in the I-V curve, or at least a flattening out of the characteristic. Such a phenomenon occurs in InSb at low temperatures (Cronin 1977). The effect is not expected to occur in CMT however, since the electron heating is likely to be much less. Figure 6.1 summarises thepossible effects of the various scattering mechanisms on the I-V characteristic.

6.2.3 The energy balance equation, electron temperature model and energy relaxation time.

In a steady state condition, the average rate of energy gain per electron from the field must be equal to the rate of energy loss per electron to the lattice via inelastic collisions with phonons (Joule heating). This can be expressed as

$$e\mu E^2 = \left\langle \partial\epsilon/\partial t \right\rangle_c \qquad (6.4)$$

where $\left\langle \partial\epsilon/\partial t \right\rangle_c$ is the mean energy lost per electron per

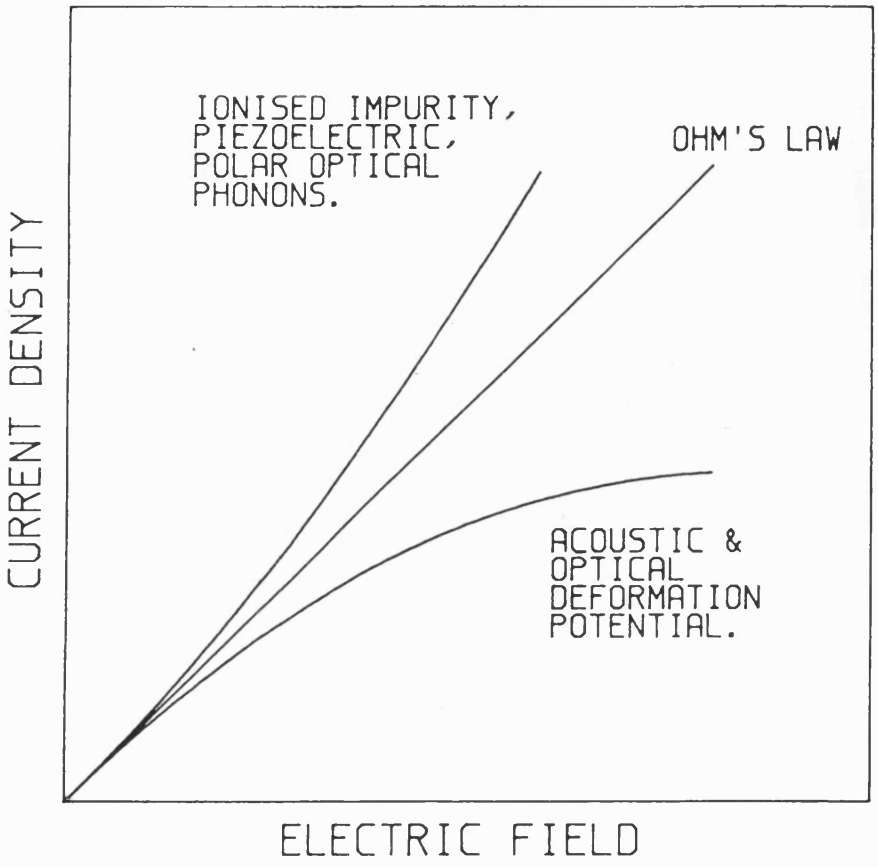

FIGURE 6.1

Diagram showing the type of nonlinear conductivity expected due to hot electron effects, for various electron scattering mechanisms in semiconductors.

second due to collisions. (6.4) is known as the *energy balance equation.* The energy loss rates for the various scattering mechanisms discussed previously are given by Seeger (1982), Kogan (1963a) and others. However, in order to gain a more qualitative understanding of hot electron effects in CMT, a simpler energy relaxation time approach will be adopted. Many of the calculations involving hot electron phenomena are performed on the basis of a single electron temperature model, in which the energy of the electrons is characterised by a single temperature (T_e) which is higher than the lattice temperature (T). By making this assumption, (6.4) can be approximated by

$$e\mu E^2 = \frac{3}{2}k_B(T_e - T)/\tau_\epsilon \qquad (6.5)$$

where τ_ϵ is defined as the *energy relaxation time.* In order to describe the electrons as having a temperature T_e, it has to be assumed that the electron gas has either a Maxwell-Boltzmann or Fermi-Dirac energy distribution; i.e. the antisymmetric part of the electron distribution must be small compared to the symmetric (Maxwellian) part. However, this is not always the case; the various scattering mechanisms can badly distort the Maxwell-Boltzmann distribution so that an unambiguous definition of an electron temperature becomes impossible. However, if there is a large electron concentration ($>10^{12}$ cm^{-3}), then electron-electron collisions occur far more frequently than collisions with other particles, and this has the effect of randomising the energy gained from

the field to such an extent that the electron distribution can be considered to be only slightly perturbed from a Maxwell-Boltzmann distribution. The use of a single electron temperature is then justified.

Even though the electron temperature model is useful in giving an understanding of hot electron effects, for a more rigourous quantitative approach, the use of powerful numerical techniques are required (e.g. Monte Carlo simulation). This is simply due to the fact that in general, the electrons do not possess a Maxwell-Boltzmann type distribution, and in some cases (when polar optical phonon scattering is considered, for example) the electron distribution can become extremely distorted and complex. Analytical solutions then become impossible, and numerical techniques must be used. In the present work, however, only the simple single temperature model will be adopted in order to obtain an empirical understanding of hot electron effects in CMT.

6.3 APPLICATION OF HOT ELECTRON EFFECTS TO SUB-MILLIMETRE WAVE DETECTION.

Photoconductivity is defined as a change in electrical conductivity of a solid due to illumination with electromagnetic radiation. In the case of short wavelength radiation (e.g. infrared) the effect is due to a change in carrier density, electrons being promoted into the conduction band by the absorption of photons. If hot electron effects are included, it is clear that a change in conductivity can be brought about by changing

the mobility of the electrons by increasing their mean energy. This second type of photoconductivity is thus due to free carrier absorption, and hence is more suited to the shorter wavelengths (i.e. sub-millimetre and far infrared radiation). Rollin (1961), Moss (1961) and Lifshits *et al* (1962) have estimated the sensitivity of such detectors, and have shown that they can be used to produce low-inertia wide-band receivers for millimetre and sub-millimetre wavelengths. Expressions for the voltage responsivity and time response will now be derived, following closely the theory of Kogan (1963b), who has shown that these quantities can be directly related to the nonlinearity of the D.C. I-V characteristic via the *hot electron* or *nonlinearity parameter* β;

$$\beta = \frac{1}{\sigma} \frac{d\sigma}{d(E^2)} \quad , \qquad (6.6)$$

where σ is the conductivity, which is assumed to be a function of electron temperature $\sigma=\sigma(T_e)$, and E is the electric field. β can be calculated directly from the I-V curve and characterises the nonlinear electrical behaviour.

In order to estimate the voltage responsivity, the change in detector voltage due to illumination must be calculated. The approach adopted by Kogan (1963b) was to calculate the increase in electron temperature (ΔT_e) due to the absorption of the electromagnetic radiation, and relate this to a change in conductivity. Consider a

crystal driven by a constant current; a change in voltage ΔV across the crystal due to a change in conductivity (electron temperature) is given by

$$\Delta V = V\frac{1}{\sigma(T_e)}\frac{d\sigma(T_e)}{dT_e}\Delta T_e \qquad (6.7)$$

The energy balance equation (6.4) can be written as

$$\sigma(T_e)E^2 = P(T_e) \qquad (6.8)$$

where $P(T_e)$ represents the power lost by the electrons to the lattice. On illumination, the electrons will gain energy from the radiation due to free carrier absorption and consequently heat up. Once a steady state condition is achieved, the additional power gained by the electrons must be equal to the increase in power lost to the lattice (ΔP). The increase in electron temperature causes a change in the mobility; this in turn causes a change in the power gained from the current source (σE^2), which must be included in the energy balance equation. Considering only the changes in power due to the crystal being irradiated, the increase in power lost to the lattice by the electrons can be written as

$$\Delta P = \frac{dP}{dT_e}\Delta T_e \ . \qquad (6.9)$$

The change in power gained from the current source is given by

$$\Delta[\sigma(T_e)E^2] = E^2\frac{d\sigma}{dT_e}\Delta T_e + 2E\Delta E\sigma(T_e) \quad . \qquad (6.10)$$

By replacing $-\Delta V/L$ for ΔE, where L is the length of the detector, and then substituting (6.7) for ΔV, (6.10) becomes

$$\Delta[\sigma(T_e)E^2] = -E^2\frac{d\sigma}{dT_e}\Delta T_e \quad . \qquad (6.11)$$

Bringing all these terms together, the energy balance equation (6.8) can now be rewritten as

$$W_{em}/v - E^2\frac{d\sigma}{dT_e}\Delta T_e = \frac{dP}{dT_e}\Delta T_e \qquad (6.12)$$

where W_{em} is the total electromagnetic power absorbed by the electrons, and v is the detector volume. Rearranging (6.12) yields an expression for ΔT_e;

$$\Delta T_e = \frac{W_{em}}{v}\left[\frac{dP}{dT_e} + E^2\frac{d\sigma}{dT_e}\right]^{-1} . \qquad (6.13)$$

(6.13) can now be substituted for ΔT_e in (6.7) to give an expression for the detector voltage responsivity ($R=\Delta V/W_{em}$), in terms of the rates of change in conductivity ($d\sigma/dT_e$) and power loss (dP/dT_e) with respect to electron temperature. However, (6.13) can be considerably simplified by introducing the nonlinearity parameter (β). From (6.6), β can be written as

$$\beta = \frac{1}{\sigma(T_e)}\,\frac{d\sigma}{dT_e}\,\frac{dT_e}{d(E^2)} . \qquad (6.14)$$

By differentiating (6.8) with respect to E^2 an expression for $dT_e/d(E^2)$ can be obtained;

$$\frac{dT_e}{d(E^2)} = \sigma(T_e)\left[\frac{dP}{dT_e} - E\frac{d\sigma}{dT_e}\right]^{-1} . \qquad (6.15)$$

Using (6.13,15), the equation for the increase in electron temperature (ΔT_e) can now be expressed in terms of β;

$$\Delta T_e = \frac{W_{em}}{v}\left(\frac{d\sigma}{dT_e}\right)^{-1}\left[\beta/(1 + 2\beta E^2)\right] . \qquad (6.16)$$

The voltage responsivity (R) can now easily be obtained by substitution of ΔT_e in (6.7);

$$R = \frac{\Delta V}{W_{em}} = \frac{V\beta}{v\sigma(T_e)[1 + 2\beta E^2]} \qquad (6.17)$$

It is possible to simplify (6.17) still further by realising that the factor in the denominator, $\sigma(T_e)[1+2\beta E^2]$, is the differential conductivity σ_d (=dJ/dE). Hence (6.17) becomes

$$R = \frac{V\beta}{v\sigma_d(T_e)} . \qquad (6.18)$$

Up to this point, only the steady state situation has been considered, where the net rate of energy gain by the electrons is zero. In order to calculate the time response of the detector, it is necessary to consider the time dependent response of the electrons to the radiation being switched off, i.e. the time constant with which the electron temperature decays back to it's dark value (due only to the energy gained from the current source). The energy balance equation (6.12) now has a time dependent term on the left hand side;

$$-\frac{3}{2}nk_B\frac{d\Delta T_e}{dt} - E^2\frac{d\sigma}{dT_e}\Delta T_e = \frac{dP}{dT_e}\Delta T_e \qquad (6.19)$$

where $(3/2)nk_B$ is the specific heat of the electron gas, n being the electron concentration. Since there is no illumination, $W_{em}=0$. (6.19) states that the rate of change of electron temperature is proportional to the difference in the rates of energy gain and energy loss. Again using (6.14,15), (6.19) can be expressed in terms of β, and on rearranging becomes

$$\frac{d\Delta T_e}{\Delta T_e} = -\frac{2}{3}\frac{d\sigma}{dT_e}\frac{1}{nk_B\beta}(1+2\beta E^2)dt \ . \qquad (6.20)$$

The solution of (6.20) is given by

$$\Delta T_e = \Delta T_0 \exp(-t/\tau) \qquad (6.21)$$

where τ is the characteristic response time;

$$\tau = \frac{3}{2}\left(\frac{k_B}{e}\right)\left(\frac{d\mu}{dT_e}\right)^{-1}\frac{\beta}{(1+2\beta E^2)} \qquad (6.22)$$

and $d\mu/dT_e$ is the change in mobility with electron temperature. Hence the time response of a hot electron photoconductor is also dependent on the nonlinearity of the d.c. I-V characteristic (through β).

(6.18) and (6.22) predict the ideal voltage responsivity and response time of a hot electron bolometer; they assume that all the incident radiation is absorbed by the electrons. This is only true when the electron scattering rate is such that $\omega\tau_e << 1$, (where ω is the frequency of the electromagnetic radiation and τ_e the electron scattering time). At higher frequencies, the absorption may be phonon assisted, in which case the radiation will heat up the lattice as well as the electrons. Moss *et al* (1973) have derived more exact expressions for the photoresponse under these conditions. However, the expressions derived here will be sufficient to give a comparative assesment of the detector for CMT alloys and n-InSb.

CHAPTER 7

MEASUREMENT OF CURRENT-VOLTAGE CHARACTERISTICS AT LOW TEMPERATURES

CHAPTER 7

MEASUREMENT OF CURRENT-VOLTAGE CHARACTERISTICS AT LOW TEMPERATURES.

7.1 INTRODUCTION.

In order to examine the hot electron effects in cadmium mercury telluride alloys as a function of composition and temperature in the region 2-20K, a fully automated computer controlled low temperature I-V characteristic measurement apparatus was developed. It was considered necessary to use an automated system because of the large number of I-V curves that needed to be measured, and such a system would enable the measurements to be done quickly and efficiently. The system was designed to allow flexibility in the way in which measurements were taken, e.g. single shot or continuous measurements over a predefined temperature range at set temperature intervals, controlled current or controlled voltage measurements and pulsed measurements to reduce Joule heating effects (see section 7.2.4). The entire apparatus was monitored by a small microcomputer from which all the operating parameters could be controlled. The computer also performed the I-V measurements and displayed them before storing them on disc. In the following section, the various aspects of the system will be described in detail. Section 7.3 will deal with the preparation of the CMT samples, and the characterisation of those samples carried out at the GEC Hirst Research Centre, Wembley.

7.2 THE AUTOMATED LOW TEMPERATURE I-V CHARACTERISTIC MEASUREMENT FACILITY.

In this section, the I-V characteristic measurement apparatus will be described in detail. The first two subsections (7.2.1,2) are concerned with the operation of the Oxford Instruments MD4 cryostat and the CMT sample holder. the temperature controller and the measurement apparatus is described in subsection 7.2.3. Subsection 7.2.4 deals with Joule heating effects, which were found to be a problem at temperatures above about 8K, and the design of a pulsed measurement system to reduce the total power input to the crystal samples. The last subsection (7.2.5) concentrates on the software and operating procedure.

7.2.1 Helium cryostat and pumping system.

Figure 7.1 shows a schematic diagram of the pumping system for the Oxford Instruments MD4 cryostat which was used for the measurements. The MD4 was fitted with a long tail attachment, and was capable of variable temperatures from 2.5K to 300K. The MD4 cryostat achieves this by allowing a flow of liquid helium down through a capillary tube via a needle valve to the sample area, where it passes over a resistance heater and thermocouple before being allowed to flow into the sample space. By adjustment of the temperature controller and needle valve, the temperature could be stabilised to within

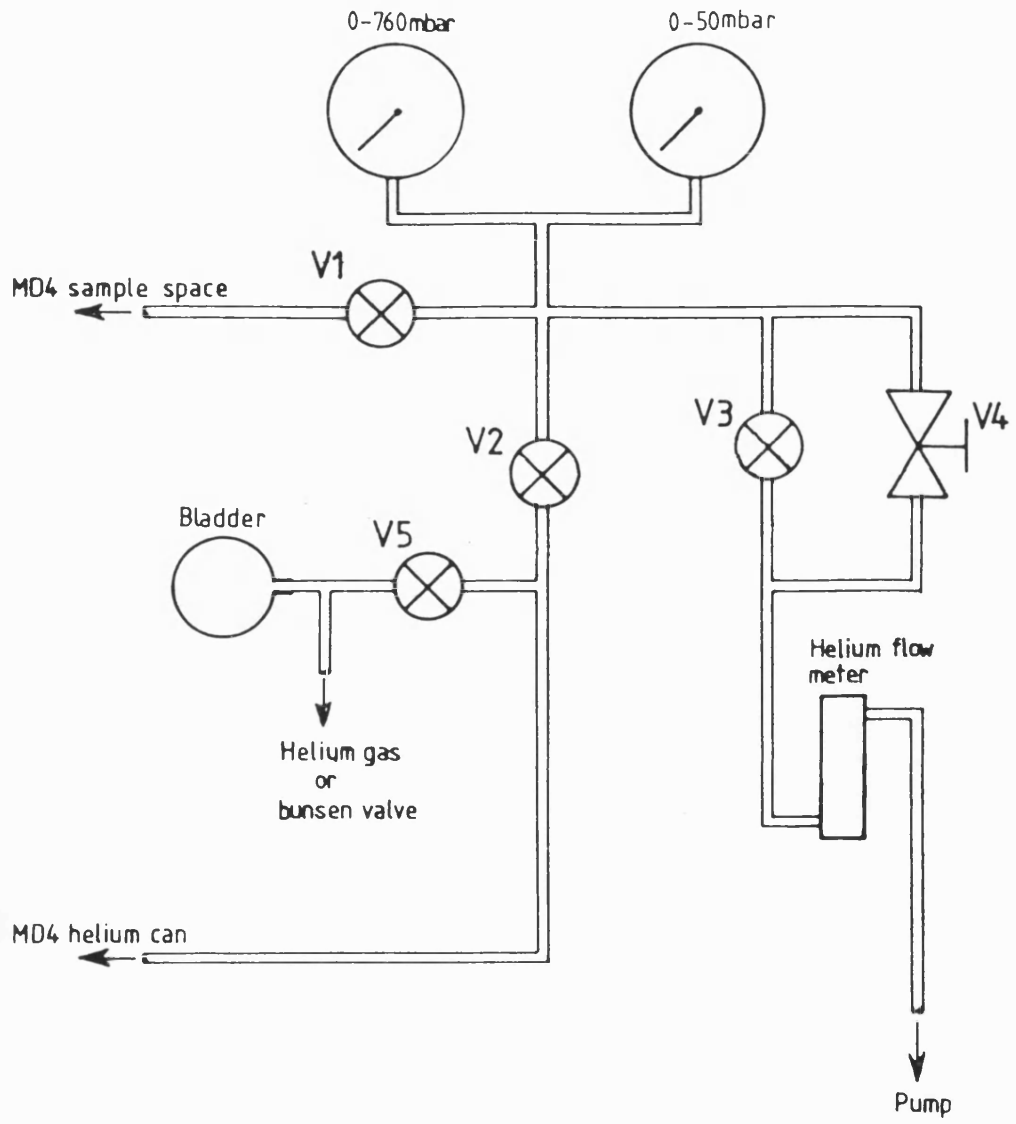

FIGURE 7.1

Schematic diagram of the pumping system for the Oxford Instruments MD4 cryostat (not shown).

0.1K.

When designing the pumping system for the cryostat, two points had to be considered: (i) the sample space needed to be pumped at a controlled rate to draw the liquid helium through the capillary, (ii) the cryostat had to be precooled with liquid nitrogen first, which required the cryostat to be pumped out and purged with helium gas before liquid helium could be transferred. The valve arrangement, shown in figure 7.1, accomodates both these requirements. Referring to the diagram, valves V1 and V2 allow pumping access to the sample space and helium can respectively. V5 is a gas inlet valve, which is used to allow helium gas back into the cryostat; fitting this port with a Bunsen valve, V5 also doubled as a gas release valve when transferring liquid helium/nitrogen into the cryostat. V4 is a high precision needle valve which is used in conjunction with the needle valve in the cryostat to control the flow rate of the liquid helium. V3 is a simple bypass valve for V4 allowing rapid pumping of the cryostat when purging.

7.2.2 Sample holder.

Figure 7.2 shows a diagram of the sample holder used for the CMT work, and a photograph is given in figure 7.3. In order to speed up the measurement process, the sample holder and measurement system was designed to accomodate four separate samples at the same time. The end of the sample holder consisted of a copper block containing eight bolts in two rows of four (two terminals

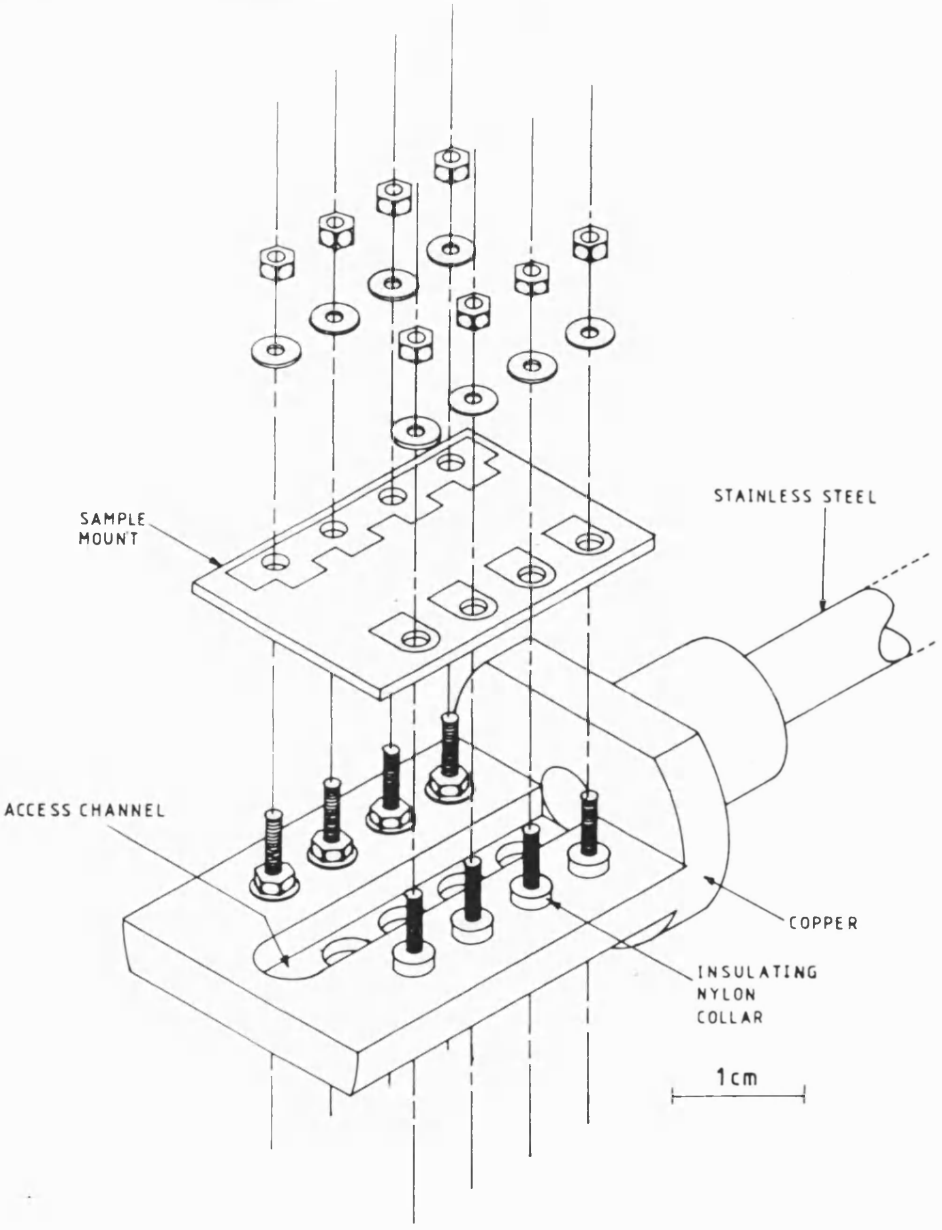

FIGURE 7.2

Exploded diagram of the CMT sample holder. The access channel and holes are for the electrical wiring and thermocouple (not shown).

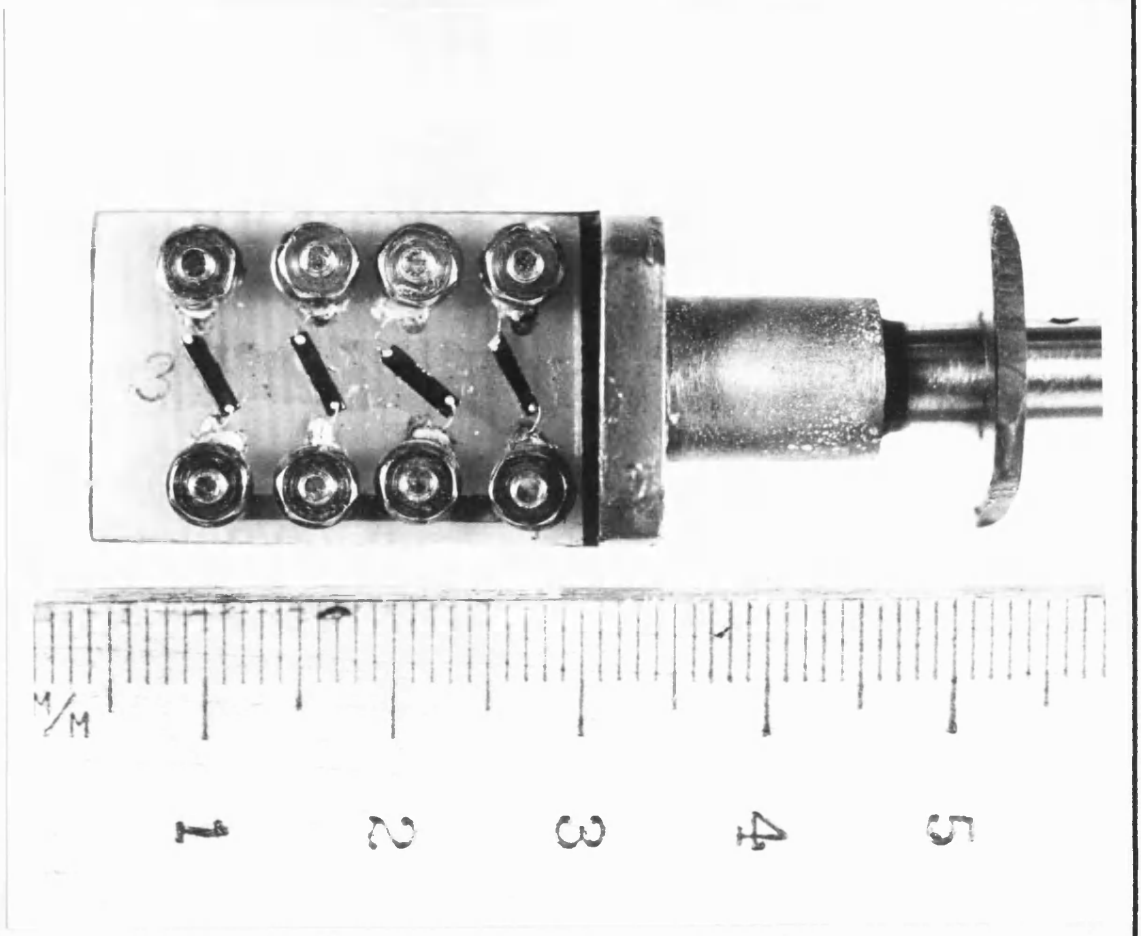

FIGURE 7.3

Photograph looking down onto the CMT sample holder, showing the circuit board mount with four CMT samples contacted into position.

per sample). A small circuit board onto which the samples were mounted was located onto the bolts, which provided the electrical contacts to the sample mounts. This allowed the samples to be replaced quickly since four more could be prepared and mounted on another circuit board while the previous four were still in the cryostat.

A total of nine thin enamelled wires had to be passed down the sample tube; four voltage lines and one common earth, and four current lines, the current return path being the sample tube itself. The sample tube also contained a Au/Fe chromel thermocouple, the junction of which was recessed into an access channel in the copper block underneath the sample mount (see figure 7.2).

7.2.3 Measurement and control hardware.

A block diagram of the measurement and control apparatus is shown in figure 7.4. The computer (BBC micro) is required to monitor and set the temperature of the cryostat via the Oxford Instruments temperature controller (DT2), as well as take the voltage and current measurements. The temperature controller was interfaced tothe computer by means of a CIL interface, which consisted of eight analogue inputs (I0-I7), four analogue outputs (O0-O3) and four relays. The temperature controller itself had several analogue outputs for monitoring temperature, set (required) temperature, error signal etc, together with one analogue input which could be used to adjust the required temperature. This input was connected to the O0 output of the CIL interface, thus

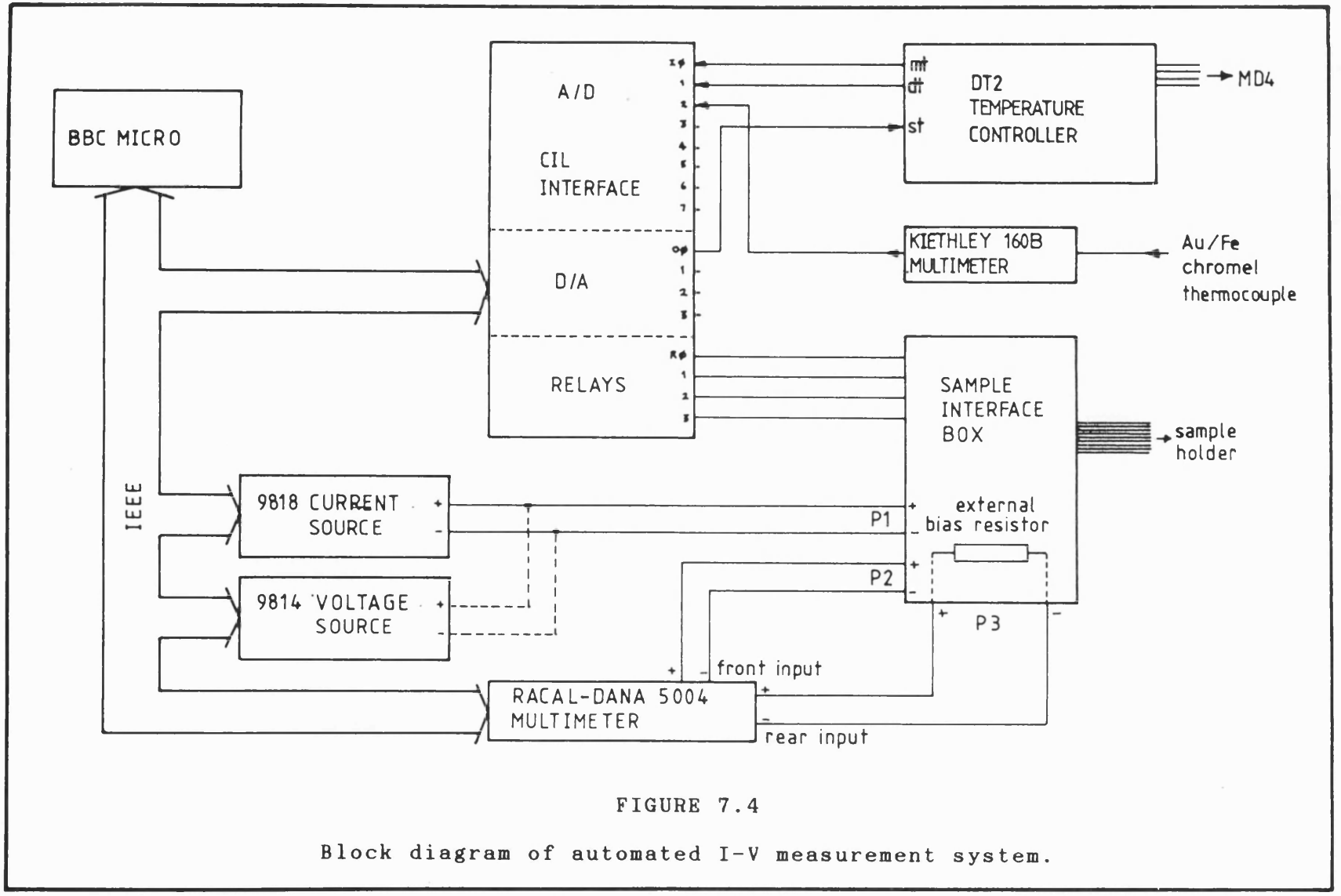

FIGURE 7.4

Block diagram of automated I-V measurement system.

enabling the computer to adjust the desired temperature setting on the controller. Two of the analogue inputs on the CIL (I0,I1) were used to monitor the measured temperature (mt) and desired temperature (dt) outputs on the controller. A third analogue input (I2) was used to measure the amplified signal of the Au/Fe chromel thermocouple in the sample holder. A Kiethley 160B digital multimeter, which has a x1000 output, was used to amplify the thermocouple voltage, whose reference junction was held at 77.3K. Hence the computer was able to monitor the temperatures of the cryostat and samples, and also adjust the temperature controller.

The four relays in the CIL interface were used to connect each sample in turn to the measurement apparatus, by switching four more precision duel relays in the sample interface box, shown in figure 7.5. The box had three ports (P1, P2 and P3, see figure 7.5), one for connections to either the voltage or current sources, depending on which measuring configuration was being used, another for sample voltage measurements and a third across which an external bias resistor could be connected for precise sample current measurement. The voltage and current sources were Time electronics programmable voltage (9814) and current (9818) calibrators. The range of the voltage calibrator was 5nV to 10V while the current calibrator could produce a constant current between 5nA and 1A. Each was equipped with an IEEE interface which allowed direct control by the computer. The voltage measurements were made using a Racal-Danar 5004 digital multimeter, which was also fully controllable via an IEEE interface. The front inputs on the 5004 were used for the sample voltage measurements,

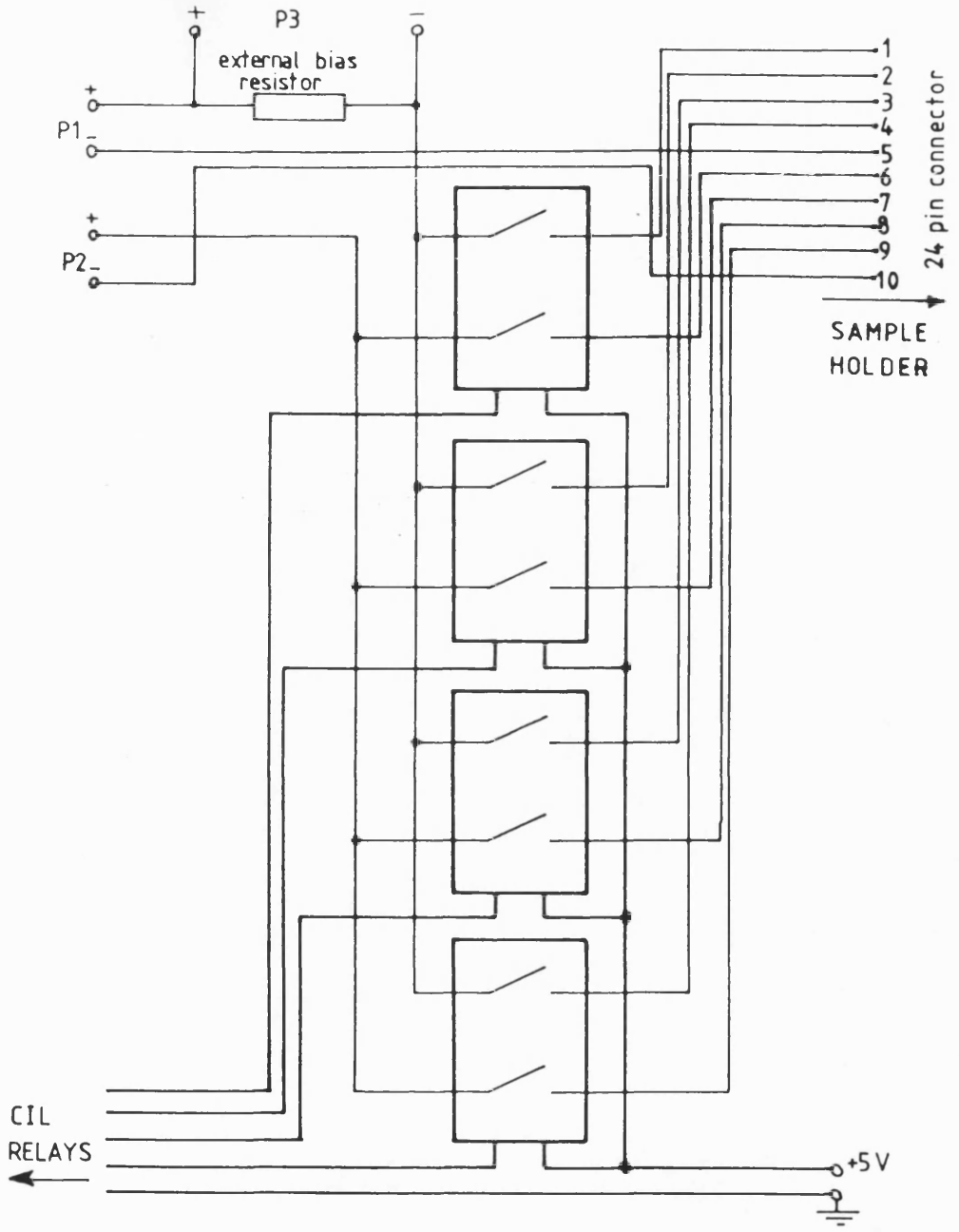

FIGURE 7.5

Circuit diagram of the sample interface box, showing the four dual precision relays. P1, P2 and P3 refer to the those ports shown on figure 7.4.

while the rear input was used to measure the voltage across the external bias resistor in order to determine the sample current. When the controlled current configuration was used (which was generally the case), the sample current was taken as that value output by the 9818, and so there was no need to measure the current directly, and hence the rear input on the 5004 was not used. In this case the bias resistor was shorted out.

7.2.4 Pulsed current measurements.

When making d.c. measurements of I-V characteristics, there is a danger that the power input to the crystals is sufficient to heat them up and so cause a change in their conductivity. This Joule heating can be difficult to distinguish from the nonlinearity caused by hot electron effects, and so a pulsed current source was built in order to reduce the total power input to the samples and hence make the effect of lattice heating negligible. To prevent any major alteration to the static (unpulsed) measurement system, the pulse unit consisted simply of a bipolar transistor switch (BC107) placed in series with the current source and sample interface box. The sample voltage was then monitored by a sample and hold (S/H) circuit, the continuous output of which was measured by the 5004 multimeter, as with the static system. The complete circuit is given in figure 7.6.

The pulse frequency is generated by a 4-input NAND (7413) which generates a square wave, the frequency of which is divided down by a 4 bit binary counter (7493) to

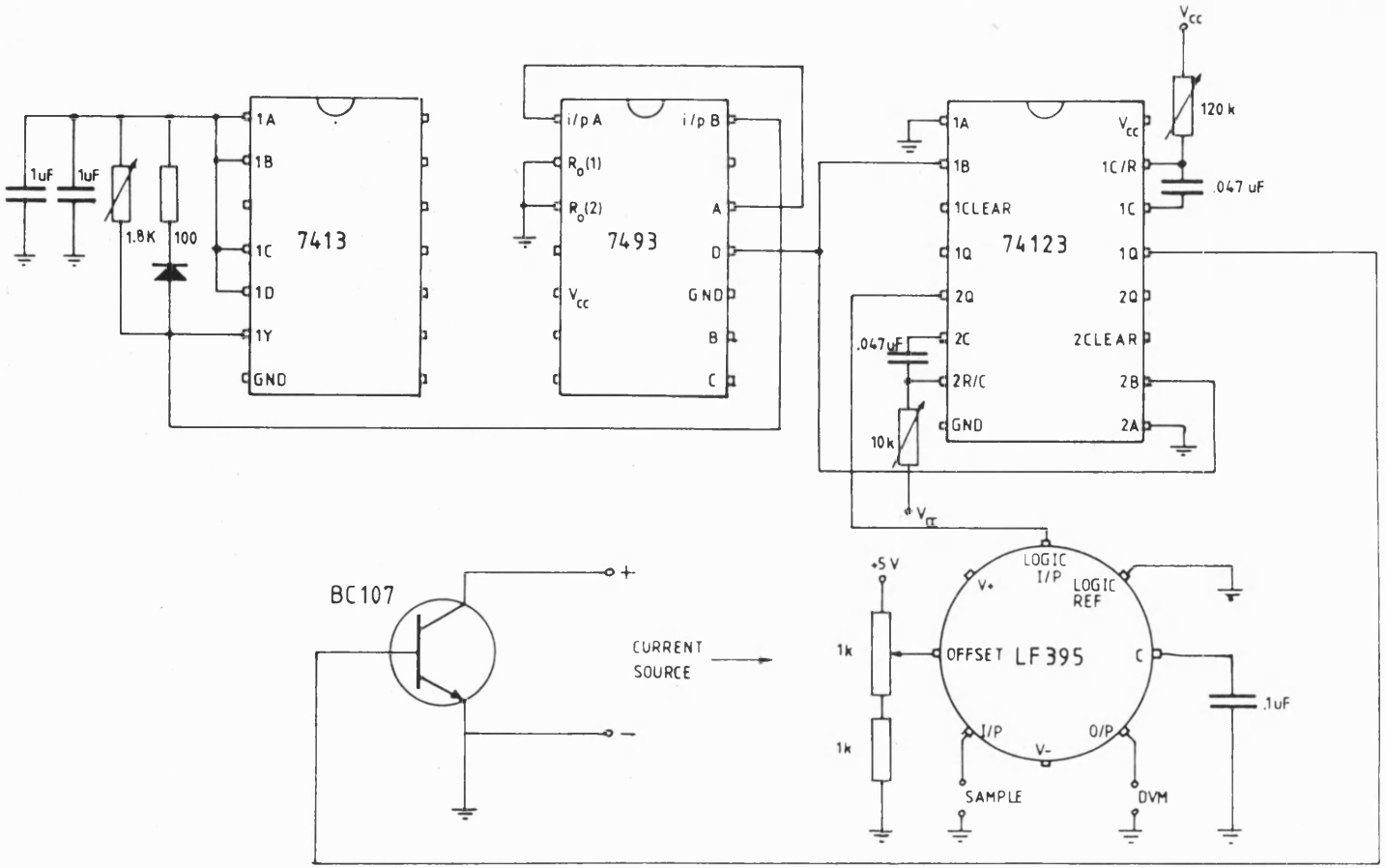

FIGURE 7.6

Diagram of the pulsed current switch and sample and hold circuitry.

give a frequency of approximately 30-400 Hz (adjustable using the 1.8K pot). This signal is then used to trigger two monostables (74123) each producing a pulse (approximately of width 150 μS), one of which is used to switch on the current via a transistor (BC107), while the other is used to activate the sample and hold (LF395). Figure 7.7 shows a timing diagram for the current pulse and sample and hold. The sample and hold pulse must be shorter than the current pulse, but long enough to enable the current source to stabilise. For this reason the width of the S/H pulse (T2) was made adjustable by a 10K pot. The current switch pulse (T1) was also adjustable via a 120K pot. The method adopted was to monitor both the S/H pulse and sample voltage pulse on an oscilloscope, and then adjust the both T1 and T2 using the relevant pots until the the correct voltage was output by the sample and hold.

A simple model was used to estimate the temperature rise in the samples caused by Joule heating when immersed in liquid helium. This model (see appendix II) predicts that even at very high current densities, the Joule heating effect would be negligible, and this was indeed confirmed experimentally, there being no difference between pulsed and continuous measurements at 4.2K. However, during the course of the experiments it was found that Joule heating effects did become a problem above about 8K. Figure 7.8 gives an example of a pulsed measured I-V curve and a static measured I-V curve taken at 10K. It is clear from this figure that Joule heating effects are far from negligible at these temperatures. With a current pulse of 180μS and a frequency of 30Hz, power input into the samples was reduced by a factor of

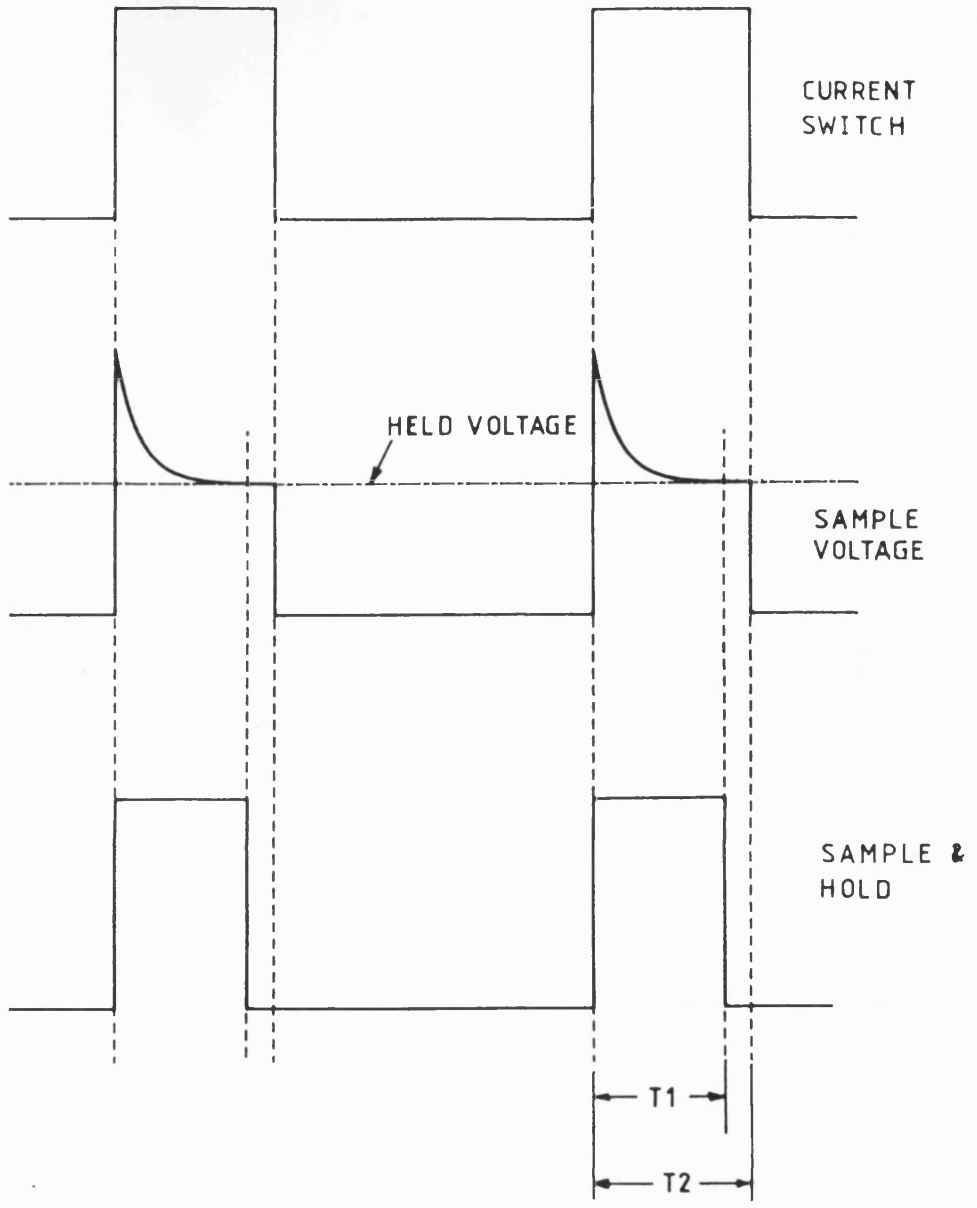

FIGURE 7.7

Diagram showing the current switch pulse (top), the sample and hold pulse (bottom), and the voltage pulse measured across the sample (middle). Both T1 and T2 must be adjusted to output the correct held voltage from the sample and hold.

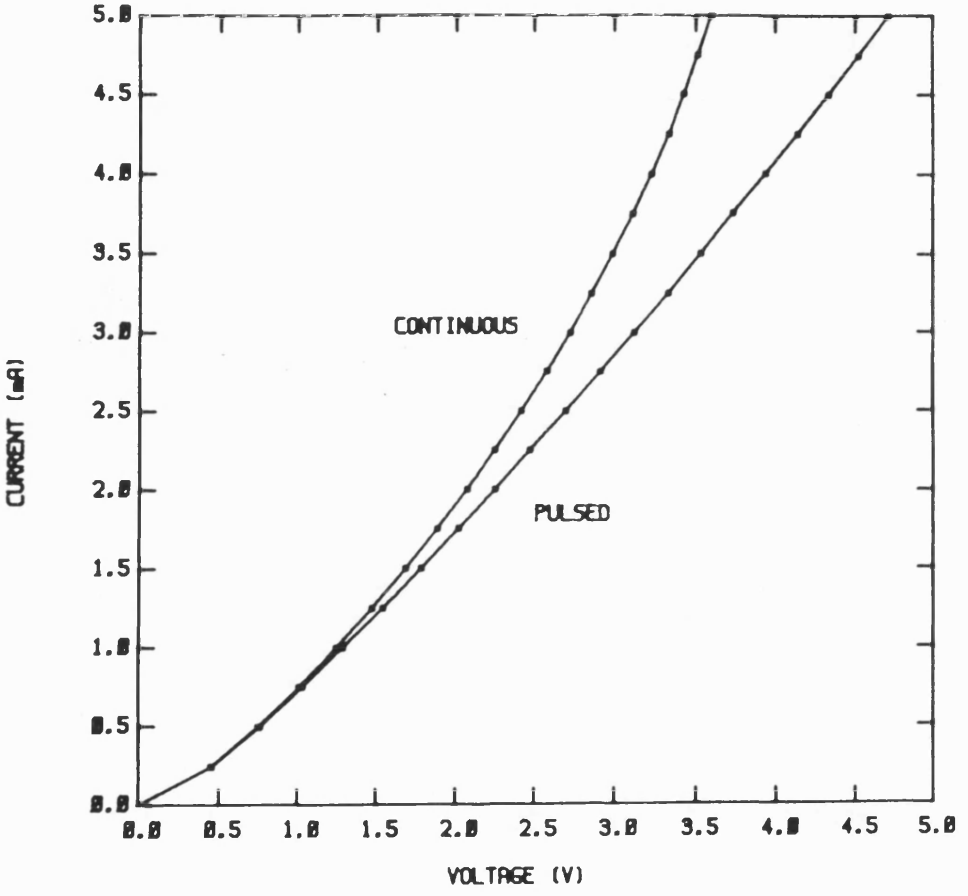

FIGURE 7.8

Comparison of pulsed and continuous I-V measurements showing the effect of Joule heating. The measurements were taken at a temperature of 10K on an x=0.245 sample of CMT.

185; at 400Hz it was reduced by a factor of 13. At the values of current used in the experiments reported here, there appeared to be no difference between measurements taken at 400Hz and 30Hz; a reduction in sample power input by a factor of 13 was sufficient to make the Joule heating effects negligible.

7.2.5 Software.

In order to realise the desired flexibility in the measurement system, extensive software is needed. Due to the restriction of memory in the BBC micro, the software had to be divided up into a number of program units, each unit would, depending on the mode of operation, 'chain' another unit off the disc. This required all the operating parameters, such as current/voltage interval, number of data points etc., to be dumped to disc by one program unit, and then re-read by the next. This disc based system had the disadvantage of being relatively slow, but allowed a library of program units to be built up in such a fashion that it was simple to add a new measurement mode when the need arose.

There are at present four program modes: mode 1 makes a single measurement of an I-V curve of the selected sample, mode 2 makes measurements of all four samples, mode 3 makes a temperature run, taking measurements at specific temperature intervals up to a specified temperature for a selected sample, and finally mode 4 performs a similar temperature run for all four samples. Each I-V curve is dumped to a separate data file on the

disc. Apart from the actual measurement and control software, there is a control program (IVPROG2) which enables all the measurement parameters to be altered and changed. The system is entirely interactive, and selection of the various parameter to be modified is made by the red function keys on the BBC micro. The display (figure 7.9) gives all the information about the parameters as well as the voltage, current and resistance measurements and various temperatures being monitored by the computer. Figure 7.10 gives an example of the graphics output of the measured I-V curve. The computer only produced such a graph if the plot mode was set to 1, else the data was dumped straight to disc and the computer continued with the program. A list of all the program units and their functions is given in appendix III.

7.3 SAMPLE PREPARATION AND CHARACTERISATION.

The samples of $Cd_xHg_{1-x}Te$ were provided by the GEC Hirst Research Centre, Wembley, and the majority of the sample preparation and characterisation was carried out there. The material was Bridgman grown and sliced into 1cm diameter discs, approximately 600μm thick. These slices were cleaned, chemomechanically polished flat and parallel and then the alloy composition (x) of each slice was determined by Fourier transform infrared spectroscopy (FTIR). The extrinsic carrier concentration was determined by Hall effect measurements, and the samples were found to be good n-type material, with carrier concentrations in the order of $10^{14}cm^{-1}$. After this

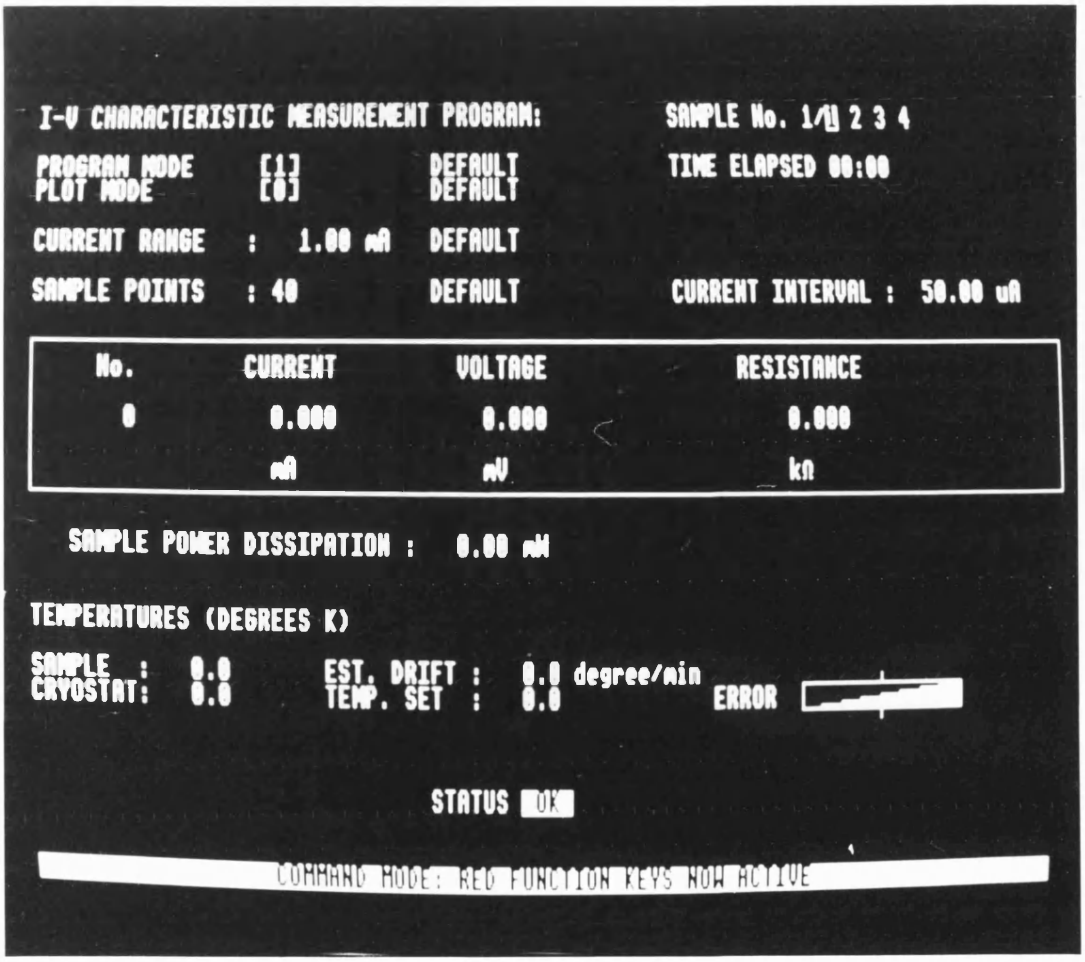

FIGURE 7.9

Photograph of the computer display of the automated I-V measurement system.

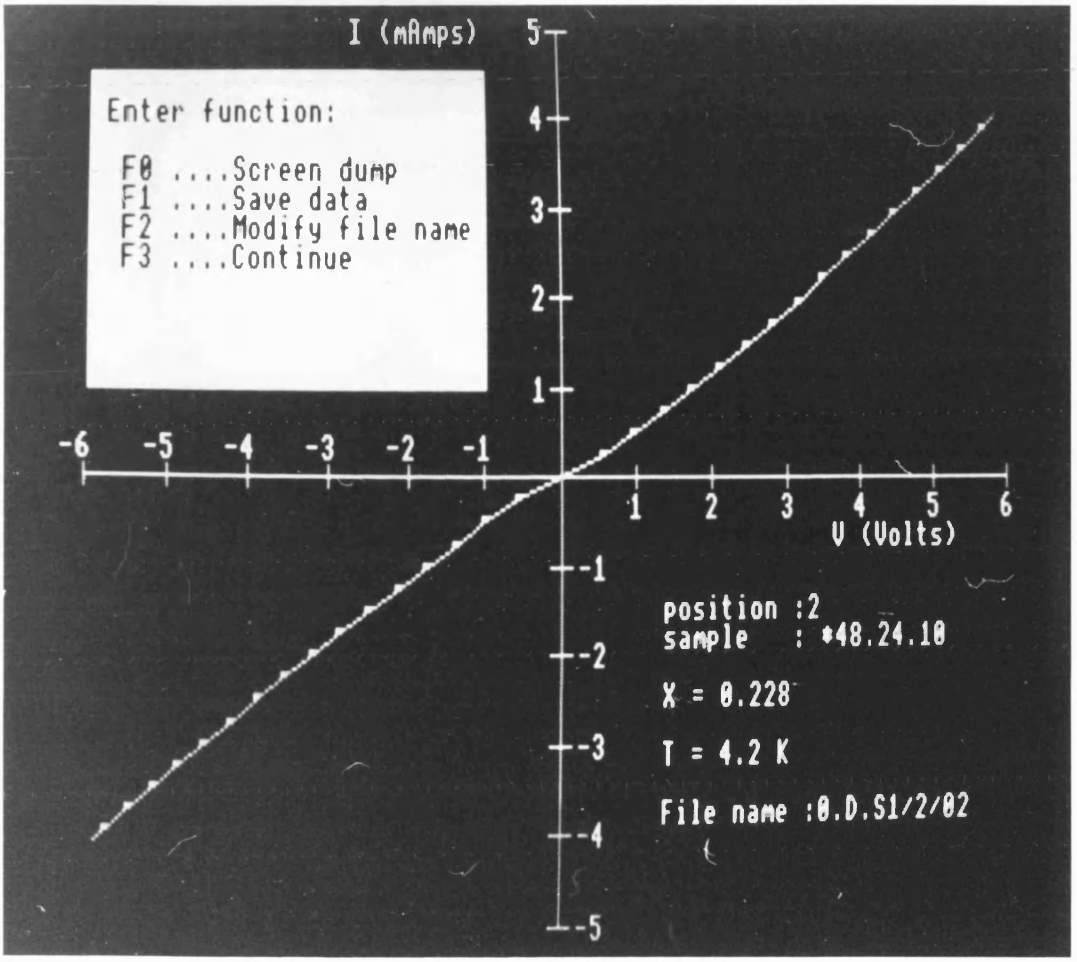

FIGURE 7.10

Photograph of the graphics output produced after an I-V measurement is performed (only with plot mode set to 1).

initial preparation and characterisation, the discs of CMT had to be cut into small ingots for the I-V measurements (the dimensions were approximately 3mmx1mmx400μm). Each slice was waxed down onto a silicon wafer and sliced up using a dicing saw. It was found that the only way to prevent the samples from breaking up was partially to cut through the thickness of the disc, and then gently snap the ingots apart after they had been removed from the wafers. This produced a great deal of damage to the edges of the ingots, which was removed during the etching process.

Once the samples were removed from the wafers and separated, they were solvent cleaned (boiled three times in butanol followed by three times in iso-propyl alcohol, and then washed in de-ionised water), and then etched down for fifteen minutes in a solution of bromine in methanol (approximately 2%) to remove all surface damage. The samples were then solvent cleaned again, and were then ready for contacting.

There is in principal no problem with making ohmic contacts to n-type CMT; indium has been shown to make good ohmic contacts to n-type material. However the problem is not to heat the CMT excessively, since this would damage the crystal by driving out mercury. The procedure adopted here was as follows: the end of the ingot was brushed with a suitable flux, and a small piece of pure indium placed on it. One end of a length of 2/1000th gold wire was brought into contact with the indium, and the wire was then heated using a soldering iron until the indium melted and formed a spherical contact on the surface of the sample. This allowed indium

contacts to be made without heating the sample anymore than was necessary. The procedure was then repeated for the contact at the other end, and the contacted sample cleaned in iso-propyl alcohol.

The dimensions of the contacted samples were measured using a travelling microscope connected to a micrometer. Since the samples were not uniform in the shape subsequent to etching, an average of some thirty readings were taken. This information was then stored on disc together with compositional x value and sample identification so that all the analysis programs could have ready access to the data.

CHAPTER 8

NONLINEAR ELECTRICAL BEHAVIOUR AND SUB-MILLIMETRE WAVE DETECTION IN CADMIUM MERCURY TELLURIDE

CHAPTER 8

NONLINEAR ELECTRICAL BEHAVIOUR AND SUB-MILLIMETRE WAVE DETECTION IN CADMIUM MERCURY TELLURIDE.

8.1 INTRODUCTION.

In chapter 6, the theoretical background of nonlinear conductivity due to hot electron effects in semiconductors was outlined. This chapter is concerned with the measurement of nonlinear electrical effects in n-type cadmium mercury telluride alloys, $Cd_xHg_{1-x}Te$ (CMT), as a function of lattice temperature ($2.5<T<20K$) and alloy composition ($x=0.228$, 0.245, 0.286), using the experimental apparatus described in chapter 7. Nonlinear conductivity in CMT has been investigated before: Nimtz *et al* (1974) have studied high field effects in CMT at $T=77K$ for a sample of $x=0.205$, while Chattopadhyay (1981) has predicted theoretically the hot electron drift mobility for the same x value and temperature using Monte Carlo techniques. Chattopadhyay and Nag (1975) have calculated the influence of the various scattering mechanisms on the mobility, and have shown that at 77K, account must be taken of polar optical phonon scattering, and more specifically the electron interaction with the TO phonons of HgTe, as well as ionised impurity scattering. Because of this, Chattopadhyay (1981) has taken no account of piezoelectric scattering in his drift calculations, having shown that it only affects the vanishly small field mobility by 0.2% at 77K, and the effect is reduced still further at higher fields due to

the increased energy of the electrons. Sladek (1960) and Cronin (1977) have calculated the I-V characteristics of n-InSb at 4.2K, and have shown that piezoelectric scattering does in fact determine the energy loss rate, while ionised impurity scattering dominates the momentum loss (mobility). Because CMT has a more polar nature than n-InSb, the degree of electric polarisation caused by the acoustic phonons should be greater; the piezoelectric coupling is thus likely to be stronger in these alloys, and so at low temperatures, ionised impurity and piezoelectric scattering should dominate the momentum and energy relaxation respectively, as with InSb. Another type of scattering not mentioned in chapter 6 which may be applicable to CMT is alloy scattering; this has been shown to become important only at relatively large x values (>0.4), and so will not be considered here (Chattopadhyay and Nag 1975).

To produce nonlinear effects at the lower temperatures concerned with in this work, much smaller fields are required, typically of the order of 5 Vcm^{-1} as compared to the work of Nimtz *et al* (1975), who used fields of 10^4 Vcm^{-1}. The I-V characteristics of CMT at 4.2K and below have been measured by Kimmit *et al* (1985) for samples with x>0.39, in order to assess their performance as detectors for the sub-millimetre and far infrared wavelengths. The possibility of using CMT alloys as hot electron bolometers and heterodyne receivers for these wavelenghs has been under investigation for some time (Weber and Kulpa 1980, 1982, Kimmit *et al* 1985). Putley (1966) first suggested the use of CMT as a far infrared detector since at the correct alloy composition it showed similar properties to the normally used

electron bolometer n-InSb, and work by Weber and Kulpa (1980,1982) has evidenced that CMT may have an improved bandwidth as compared to n-InSb. Section 8.4 of this chapter is concerned with the assessment of the samples studied here with respect to their possible use as detectors. The voltage responsivity and time response are calculated from the measured I-V curves, using the expressions of Kogan (1960) derived in chapter 6. Before discussing the detector applications, however, Section 8.2 discusses briefly the semimetal-semiconductor crossover that occurs in CMT alloys, and hence justifies the range of x chosen for investigation. Section 8.3 will present the measured I-V curves and discuss the observed nonlinearity in terms of electron temperature and energy relaxation time. Finally, section 8.5 summarises the results and gives an indication of possible further work.

8.2 SEMIMETAL-SEMICONDUCTOR CROSSOVER IN $Cd_xHg_{1-x}Te$.

HgTe is semimetal with a band overlap of 0.30 eV at T=4.2K, while CdTe is a semiconductor (E_g=1.65 eV at T=4.2K). Hence as the alloy composition (x) of $Cd_xHg_{1-x}Te$ varies from 0 to 1, a crossover from semimetallic to semiconductor type behaviour is expected. This phenomenon is depicted in figure 8.1. The variation of the bandgap with x and temperature (T) has been measured by Hanson, Scmit and Casselman (1982), who have produced an empirical expression for the bandgap as a function of x and T of the form

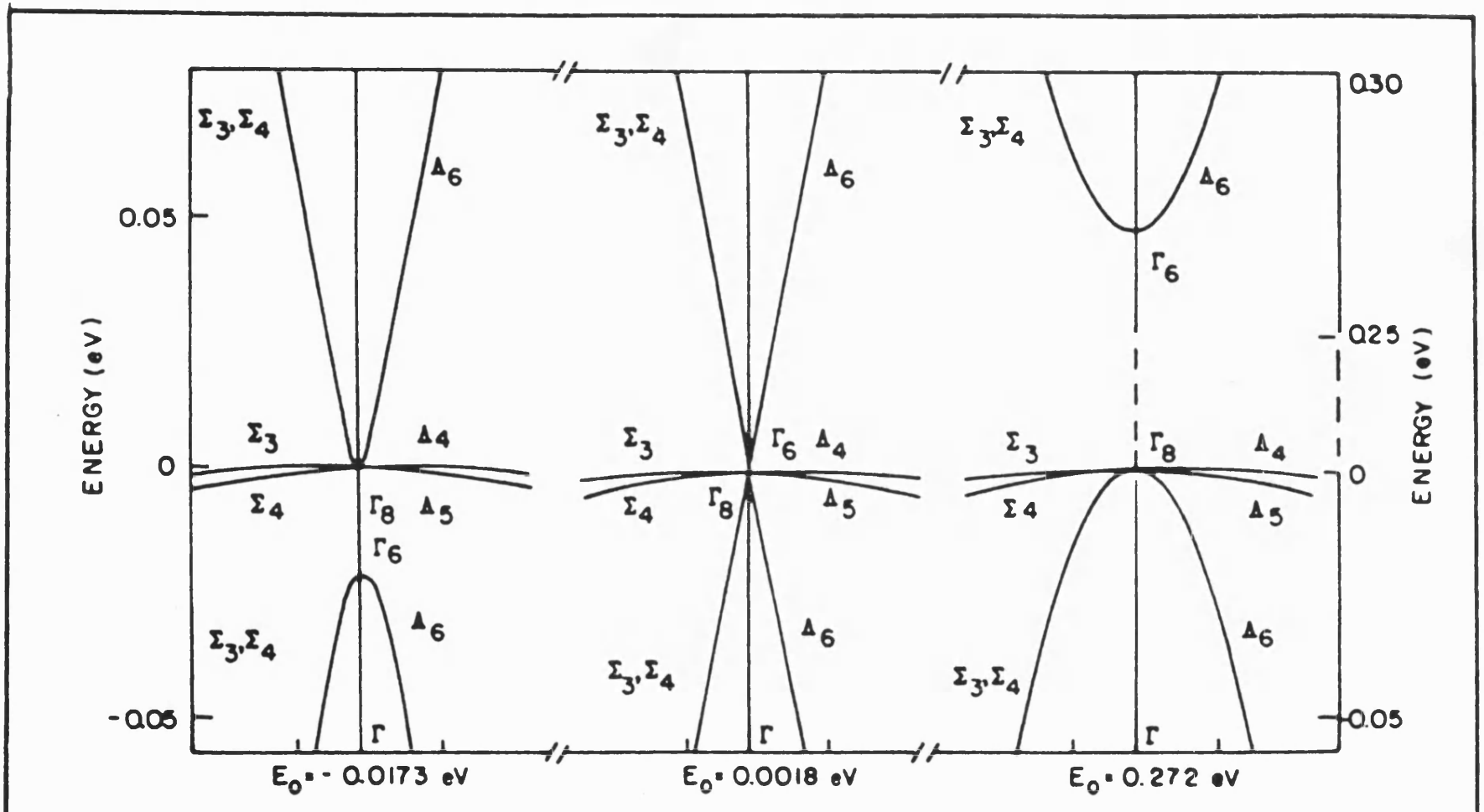

FIGURE 8.1

Band structure near the Γ-point of $Cd_xHg_{1-x}Te$ for selected values of direct gap energy [from Overhof (1971)]

$$E_g = -0.302 + 1.93x + 5.35(10^{-4})T(1-2x) - 0.810x^2 + 0.832x^3 \ (eV) \qquad (8.1)$$

Using (8.1), the alloy composition which gives the zero gap (crossover point) at 4.2K has been calculated as x=0.165. Since the work reported here is restricted to semiconductors, only samples with x>0.16 will be investigated. Thus all the samples will tend to be narrow gap semiconductors, since even at x=0.3, the bandgap is still in the order of 0.2 eV.

8.3 CURRENT-VOLTAGE CHARACTERISTICS OF CMT; EVALUATION OF NON-OHMIC BEHAVIOUR.

For x=0.20 and below, no deviation from Ohm's law was observed at the values of current density used, while for x>0.30, the resistance of the samples were too high to enable reliable measurements of sample voltage due to noise (only very small currents could be used due to the limitations of the current source). It was also found to be increasingly difficult to make good ohmic contacts to the higher x values. For these reasons, therefore,only the results for three samples with x=0.228, x=0.245 and x=0.286 will be reported.

Table 8.1 gives the dimensions and extrinsic carrier concentration of the three samples. The I-V characteristics were measured from 3K up to 20K at intervals of 1K for each sample, and figures 8.2-4 show typical results at four temperatures between 4.2K and

TABLE 8.1

Sample	x value	dimensions			N
		l (mm)	w (mm)	t(μm)	(cm^{-3})
*48.24.10	0.228	7.35	1.24	126	1.0×10^{14}
*48.22.13	0.245	4.26	1.42	545	1.5×10^{14}
*48.18.23	0.286	4.12	1.27	470	2.0×10^{14}

Dimensions, compositional x value and extrinsic electron concentration (N) for the three samples of $Cd_xHg_{1-x}Te$ investigated.

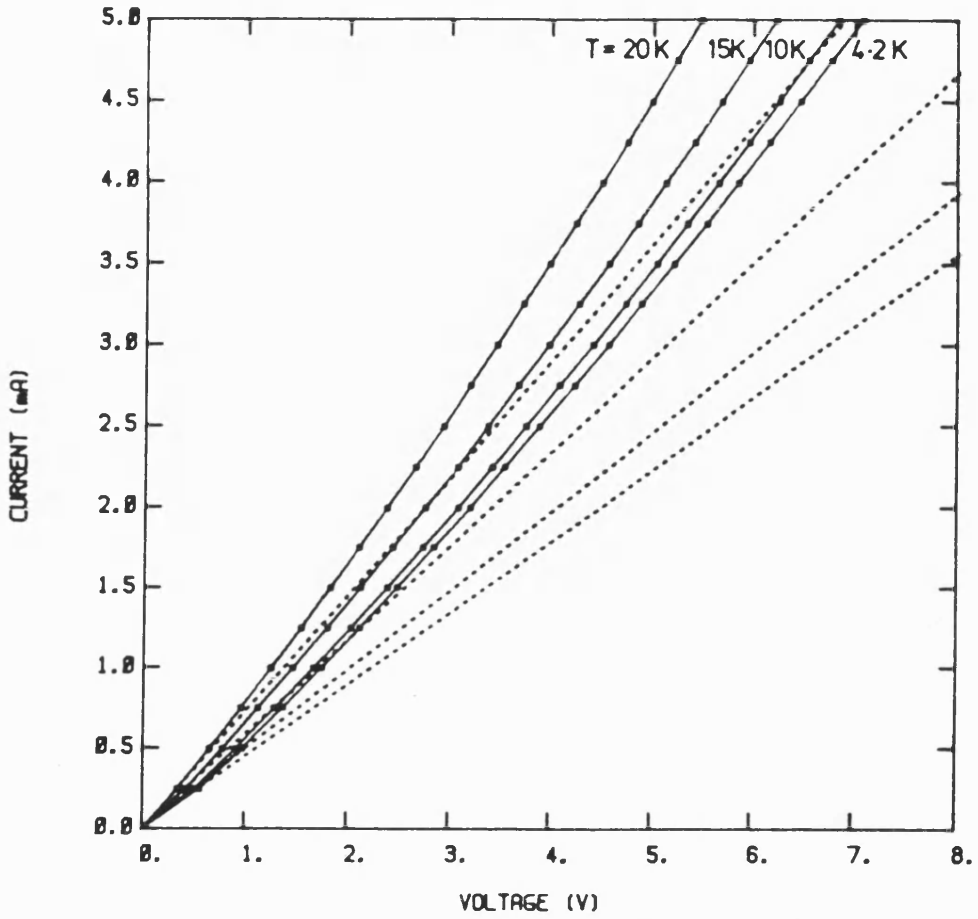

FIGURE 8.2

I-V characteristics for $Cd_xHg_{1-x}Te$ with x=0.228 (sample *48.24.10) at lattice temperatures of T=4.2K, 10K, 15K and 20K. The dotted lines show the ohmic behaviour in each case.

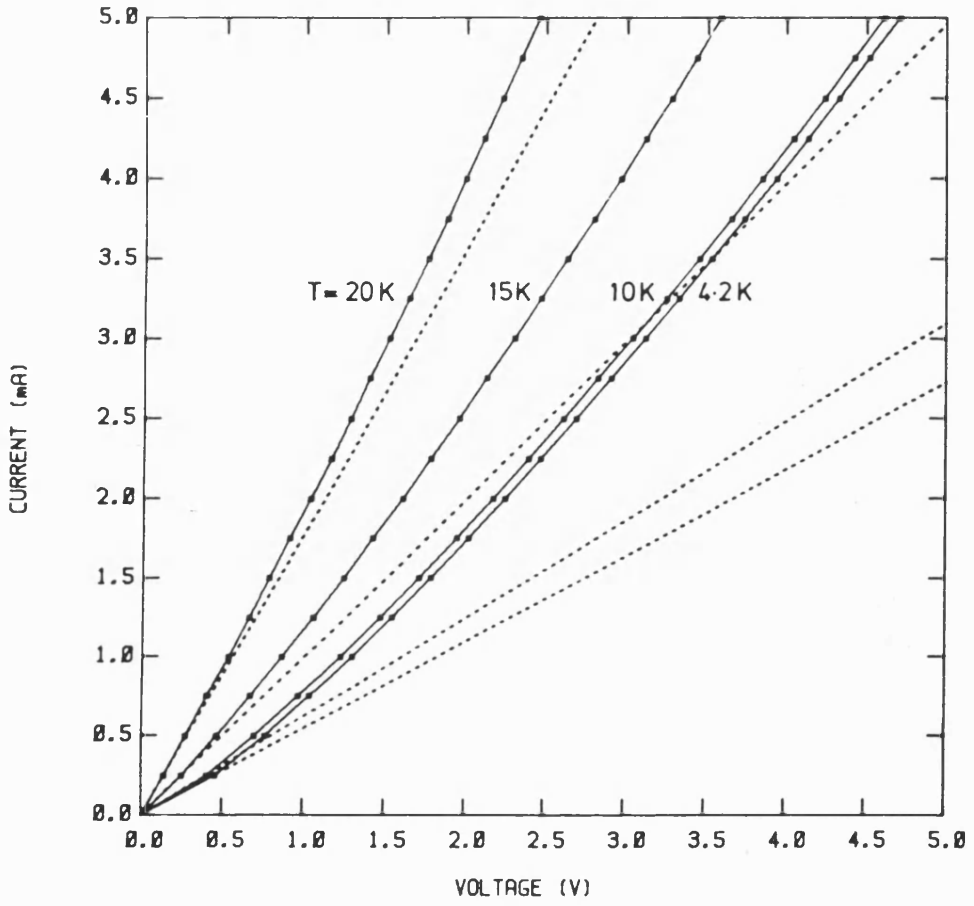

FIGURE 8.3

I-V characteristics for $Cd_xHg_{1-x}Te$ with x=0.245 (sample *48.22.13) at lattice temperatures of T=4.2K, 10K, 15K and 20K. The dotted lines show the ohmic behaviour in each case.

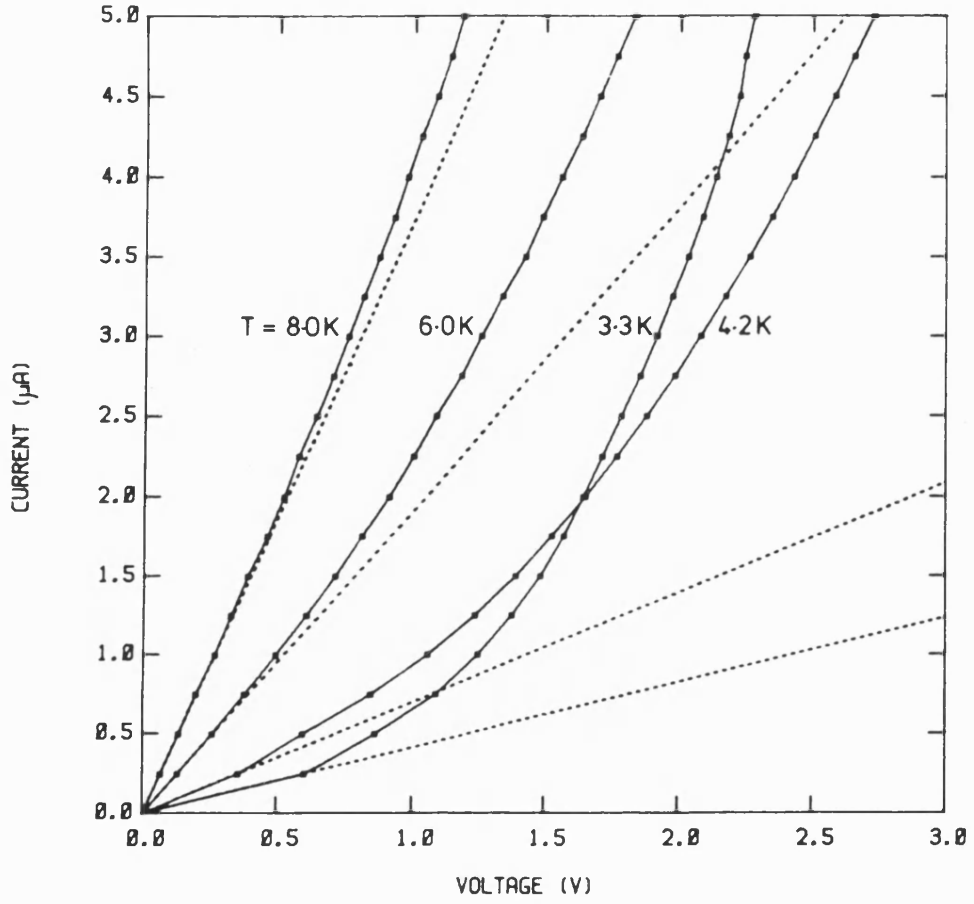

FIGURE 8.4

I-V characteristics for $Cd_xHg_{1-x}Te$ with x=0.286 (sample *48.18.23) at lattice temperatures of T=3.3K, 4.2K, 6.0K and 8.0K. The dotted lines show the ohmic behaviour in each case.

20K. The nonlinearity is made clearer in each case by the dotted line, which indicates the ohmic behaviour. In the case of the x=0.286 sample, the high resistance meant that only relatively small currents (μA) were required to give electric field strengths high enough to produce nonlinear effects. Under these conditions, Joule heating was not a problem, and continuous measurements could be made. However, for the 0.228 and 0.245 samples, the currents were sufficiently high (mA) that pulsed measurements were required in order to reduce the lattice heating (see chapter 7).

8.3.1 Deviations from Ohm's law.

From the results given in figures 8.2-4, four points are immediately obvious: (a) all the characteristics show a positive deviation from Ohm's law, (b) the characteristics tend towards linearity at higher temperatures, (c) most of the nonlinearity appears to be at lower fields, the characteristics becoming more linear at higher fields, (d) samples having higher x values show a greater degree of nonlinearity. The first of these points is consistent with the assumption that the mobility is governed by ionised impurity scattering (see chapter 6). As the lattice temperature is increased, the phonon occupancy governed by the Planck equation also increases; this leads to a greater energy loss rate, and hence a more linear characteristic, as was observed in point (b). The last point (d) arises because as x increases, the temperature dependence of the mobility is enhanced. If the momentum relaxation time is governed by

ionised impurity scattering, then theoretical calculations show that the conductivity of the higher x values do have a much stronger dependence on electron temperature than lower x material, and in fact with $x<0.2$, there appears to be little change in conductivity with temperature. This has been confirmed experimentally by many authors who have measured the Hall mobility in the temperature region of 4.2K (see, for example, Scott 1972). Figure 8.5 shows the temperature dependence of the zero field conductivity for the three samples examined here, calculated from the measured characteristics. As expected, the $x=0.286$ sample shows a much stronger dependence of conductivity on temperature, the $x=0.228$ sample showing the least effect; the higher x values, therefore, show the greatest degree of nonlinearity.

Another way of depicting the non-ohmic behaviour is by plotting the relative change in conductivity (σ/σ_o-1) against E field, as in figures 8.6,7. Figure 8.6 shows the results for the $x=0.245$ sample at various lattice temperatures, while figure 8.7 shows all three samples at $T=4.2K$. The graphs clarify the behaviour already observed in the I-V characteristics; figure 8.6 clearly shows the increased effect on the nonlinearity of decreasing the lattice temperature, while figure 8.7 emphasises that the nonlinearity increases sharply with x.

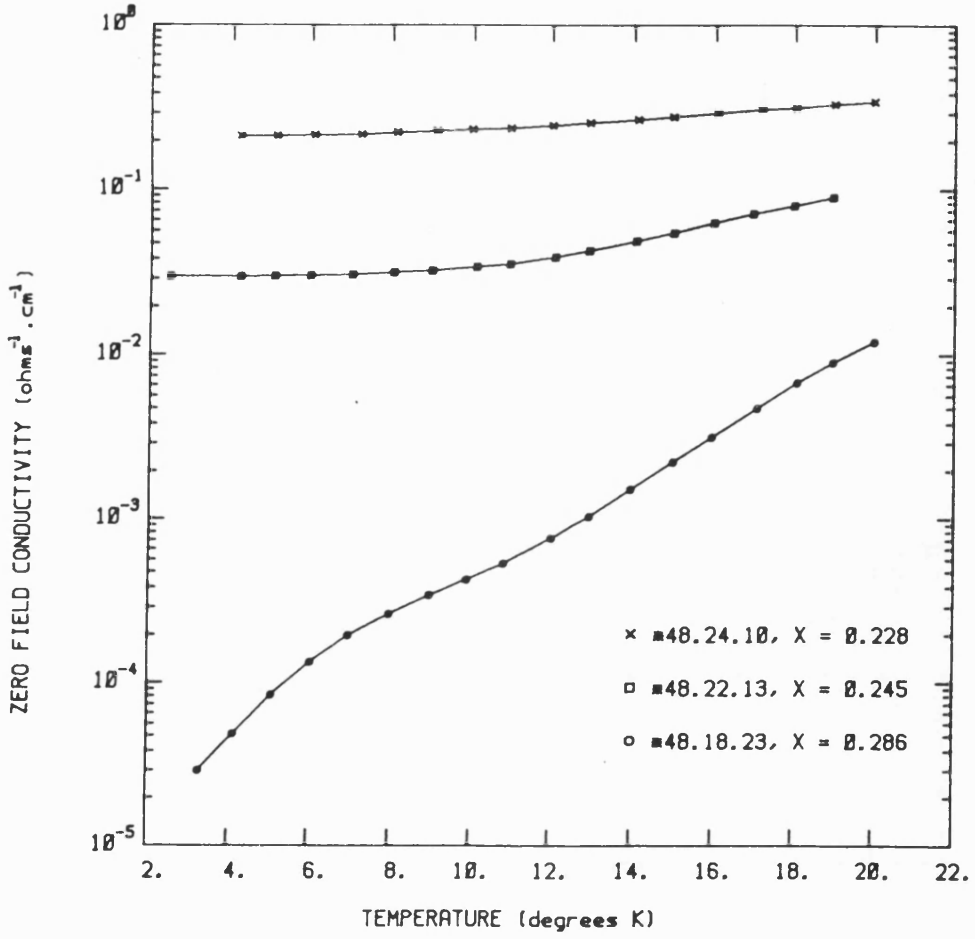

FIGURE 8.5

The zero field (ohmic) conductivity as a function of temperature for $Cd_xHg_{1-x}Te$ (x=0.228, 0.245, 0.286), calculated from the gradient of the measured I-V characteristics at E=0.

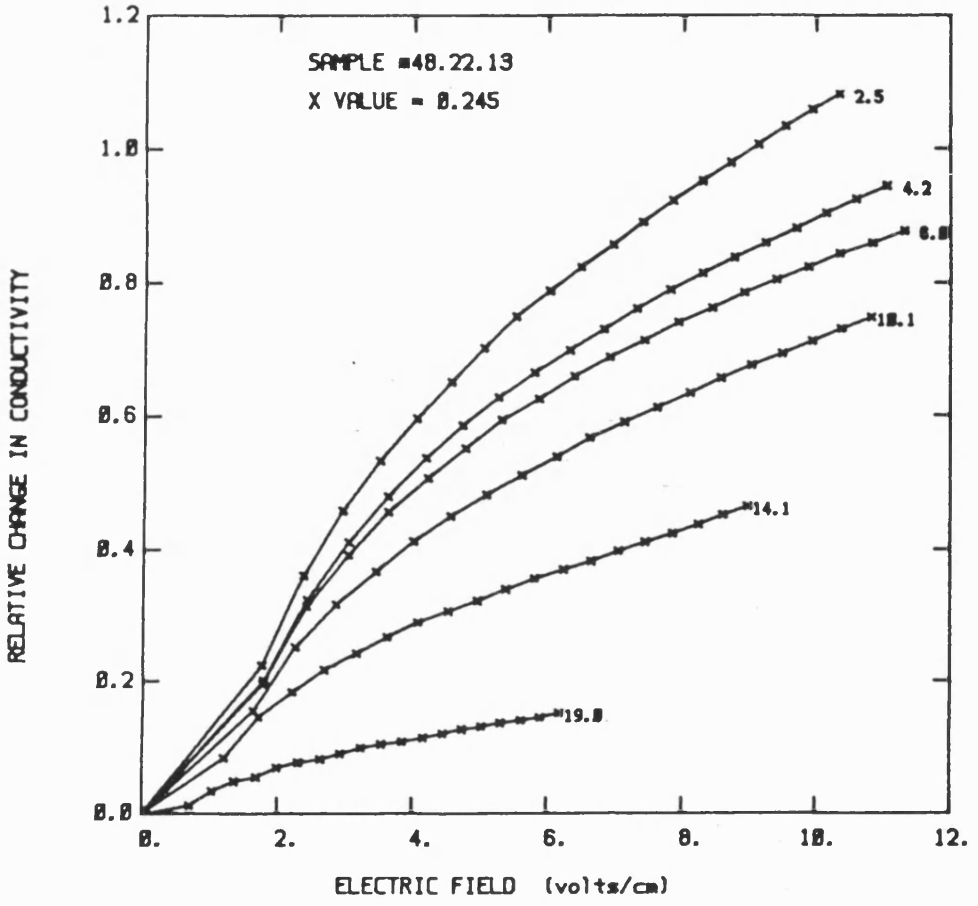

FIGURE 8.6

Relative change in conductivity ($\sigma/\sigma_o - 1$) as a function of electric field (E) for $Cd_xHg_{1-x}Te$, with x=0.245 (sample *48.22.13), at various temperatures.

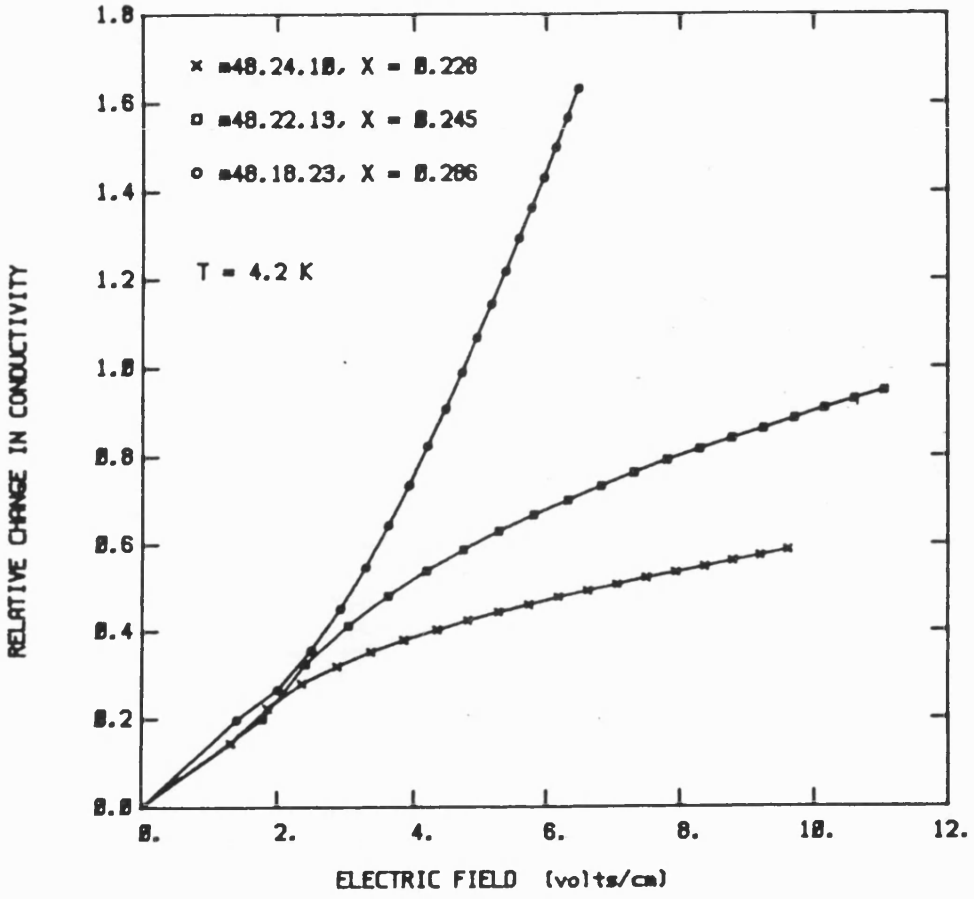

FIGURE 8.7

Relative change in conductivity ($\sigma/\sigma_0 - 1$) as a function of electric field (E) for $Cd_xHg_{1-x}Te$, with x=0.228, 0.245 and 0.286, at T=4.2K.

8.3.2 Electron Temperature and Energy Relaxation Time.

If ionised impurity scattering is assumed to be the only mechanism limiting the mobility, then the x-axis in figure 8.5 can be taken to represent electron temperature, as opposed to lattice temperature. The justification for this is as follows: the momentum relaxation time due to ionised impurity scattering is directly dependent on electron energy (temperature), the only effect that the lattice temperature has is through the change in bandgap, which in turn affects the effective mass of the electrons via the k.p interaction; this is a relatively small effect. Hence, to a first approximation, the conductivity can be taken to be a function of electron temperature only. Thus by calculating the conductivity at each point in the I-V curve, and relating this to a temperature via the curves given in figure 8.5, the relative change in electron temperature ($T_e/T-1$) can be calculated as a function of E field. Figure 8.8 gives the results of this calculation for the x=0.245 sample, again at various lattice temperatures, while figure 8.9 shows the relative change in electron temperature as a function of E field for all three samples at T=4.2K.

As expected, the electron heating is greater at lower temperatures (figure 8.8), due again to the smaller energy loss rate. The marked flattening out of the curves indicates that the energy loss rate is increasing with electron energy, thus preventing any additional rise in electron temperature as the field is increased; this effect is directly related to the I-V curves becoming more linear at higher fields. The electron heating

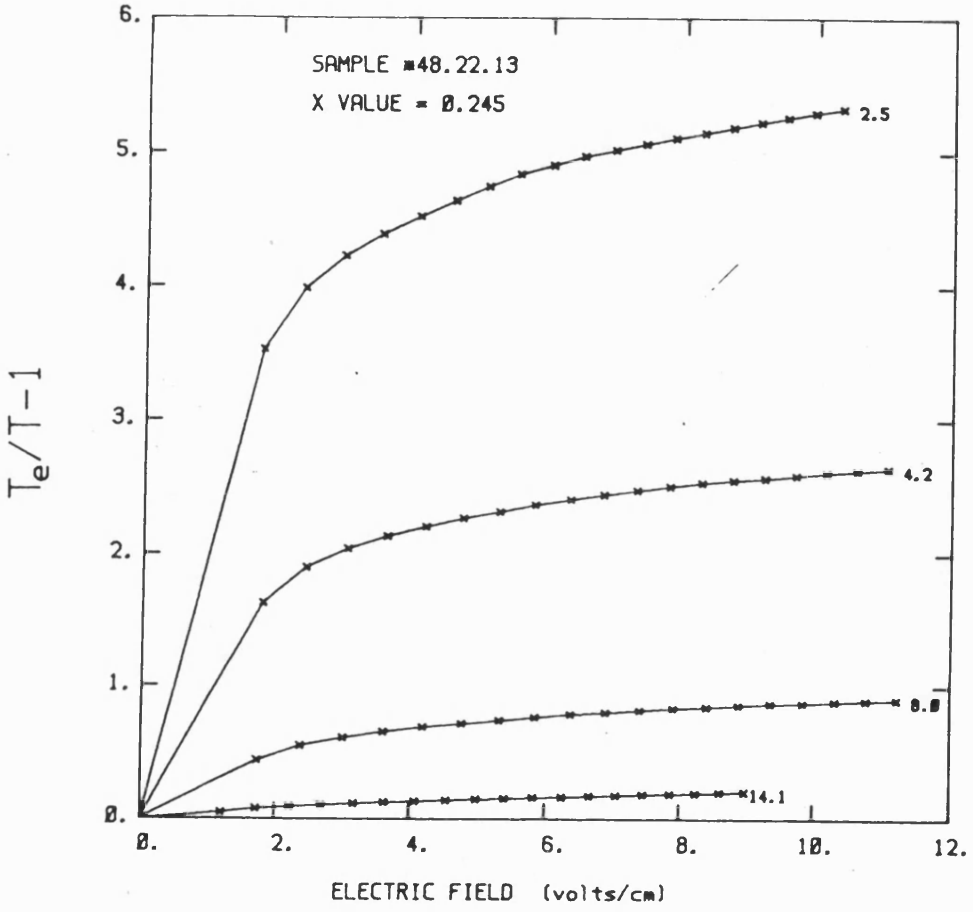

FIGURE 8.8

Relative change in electron temperature ($T_e/T-1$) as a function of electric field (E) for $Cd_xHg_{1-x}Te$, with x=0.245, at various temperatures.

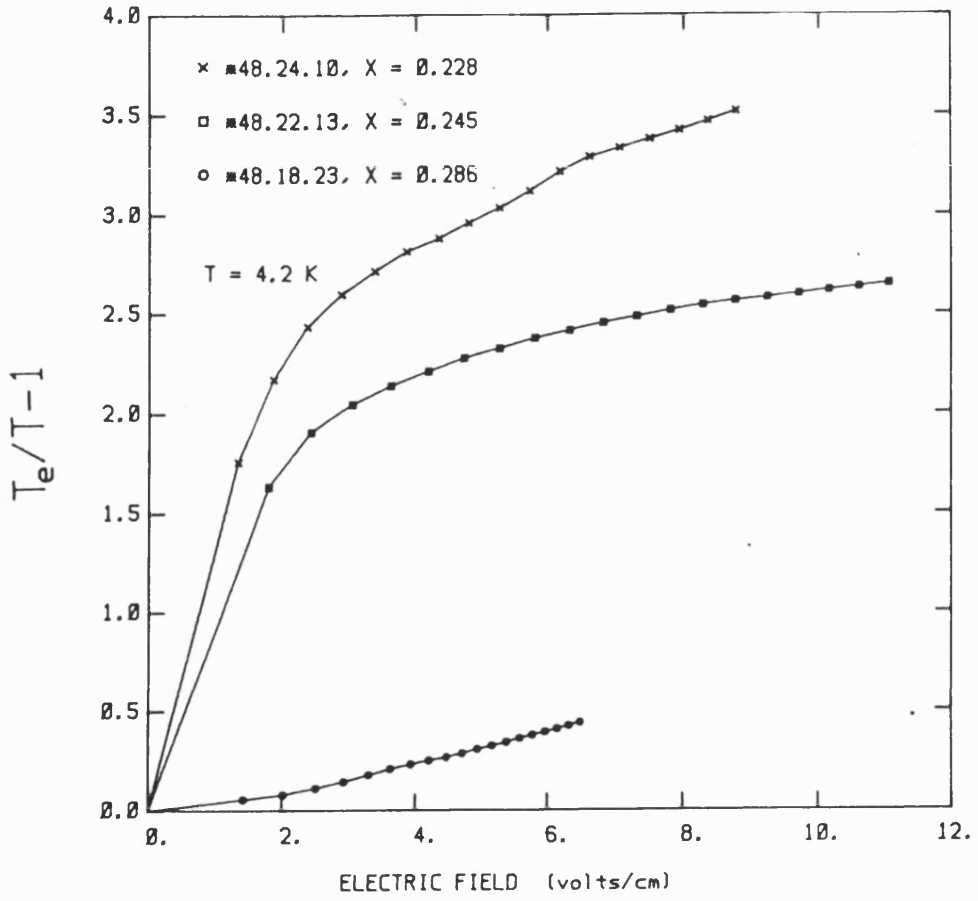

FIGURE 8.9

Relative change in electron temperature ($T_e/T-1$) as a function of electric field (E) for $Cd_xHg_{1-x}Te$, with x=0.228, 0.245 and 0.286, at T=4.2K.

appears to be much greater in the lower x value samples (figure 8.9), even though they show the least nonlinearity. This is again a reflection of the strong temperature dependence of the conductivity of those samples with higher x; the electrons only have to gain a relatively small amount of energy in order to produce a significant change in their mobility.

To quantify further the energy loss rate, the energy relaxation time (τ_ϵ) has been calculated from (6.5), and figures 8.10,11 show τ_ϵ as a function of electric field for x=0.245 at various temperatures, and all three samples at 4.2K respectively. The degree of nonlinearity is only in part due to the temperature dependence of the mobility as mentioned previously. The amount by which the electrons are allowed to raise their temperature above that of the lattice is also an important factor; this is governed by the energy loss rate, and how it varies with electron energy. A small value of τ_ϵ indicates a relatively large electron-lattice coupling, resulting in a higher energy loss rate. Figures 8.10,11 show that the energy loss rate is indeed increasing with electric field strength, as indicated by the decrease in the energy relaxation time. The results shown in these two graphs reflect concisely those observations concerning the energy loss rate that have already been made. However, one interesting additional point now becomes apparent; the energy relaxation time appears to be a much stronger function of electric field (and hence electron energy) than lattice temperature (figure 8.10). This is not the behaviour that would be expected from an energy loss mechanism purely due to acoustic phonons (piezoelectric scattering). For piezoelectric scattering,

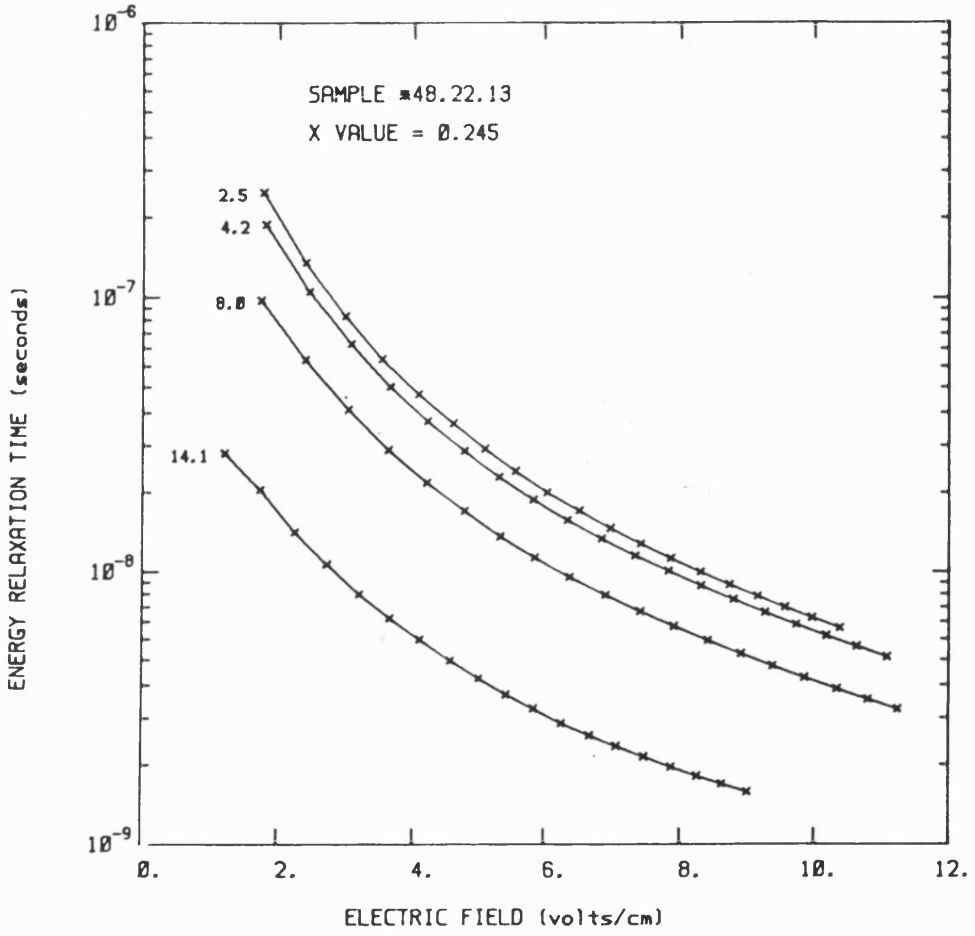

FIGURE 8.10

Energy relaxation time (τ_ϵ) as a function of electric field (E) for $Cd_xHg_{1-x}Te$, with x=0.245, at various temperatures.

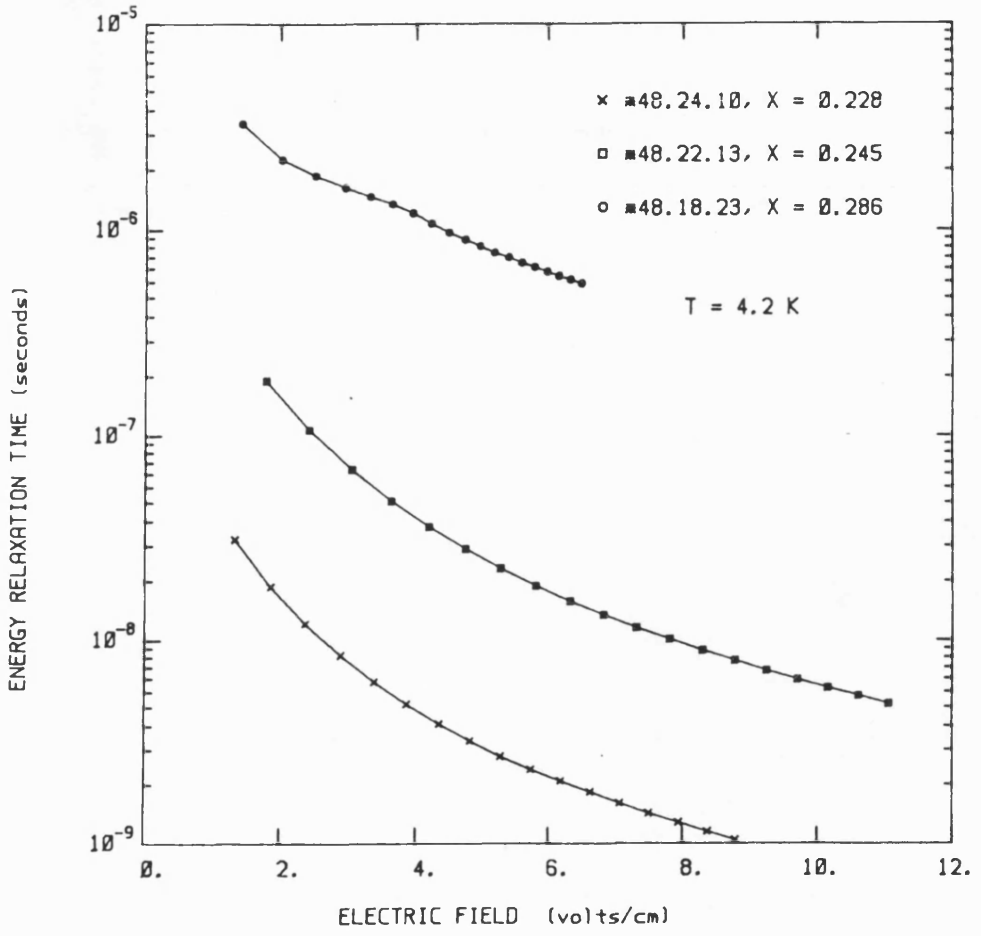

FIGURE 8.11

Energy relaxation time (τ_ϵ) as a function of electric field (E) for $Cd_xHg_{1-x}Te$, with x=0.228, 0.245 and 0.286, at T=4.2K.

the energy loss rate should decrease with increasing electron temperature (Sladek 1960), and the energy relaxation time should correspondingly increase. Thus from this work it would appear that piezoelctric scattering is not (as previously thought) the dominant electron energy loss mechanism at liquid helium temperatures. The type of behaviour observed is more typical of interactions with optical phonons. However, the lattice temperature is too low to excite thermally optic phonons, and the electron temperature is not sufficiently high to allow phonon emission. To conclude from this that other mechanisms must be responsible for the energy loss of the electrons may be unjustified, since the energy relaxation time approximation makes a great many assumptions that may not be true in the case of CMT at low temperatures (the simple model is based on a non-degenerate electron gas, for example, and the nonparabolicity of the band structure in CMT may well have an effect). Further experimental work, as well as a more exact theoretical approach is obviously required to resolve this anomaly.

8.4 APPLICATION OF CMT TO SUB-MILLIMETRE WAVE DETECTION.

The recent work by Kimmit *et al* (1985) has shown that CMT alloys with an x in the range of $0.3<x<0.4$ can produce good hot electron bolometers for the far infrared and sub-millimetre wavelengths, with detectivities similar to those of the more normally used n-InSb, but with a much increased bandwidth. A severe lattice absorption in the 220-340 μm region and also below 140 μm

means that CMT can only be used effectively above about 350 μm. Kimmit *et al* (1985) found that at large x values, CMT ceases to be a hot electron bolometer and becomes an extrinsic photoconductor; this is due to freeze out effects. No evidence of freeze out effects have been seen for $x<0.3$ material, and so it is assumed that free carrier absorption will be the only mechanism by which radiation is absorbed for the three x values of interest here.

8.4.1 The Nonlinearity Parameter.

Using (6.6), the nonlinearity parameter (β) has been calculated for all three samples as a function of electric field at 4.2K (figure 8.12). The maximum value of β occurs at an electric field of the order of 1-2 Vcm^{-1} for all three x values. A typical value of β for n-InSb is 10 cm^2V^{-2}, so the nonlinearity in CMT appears to be an order of magnitude less. The order of increasing β in figure 8.12 is x=0.245,0.228,0.286, whereas observation of figures 8.2-4 clearly show that the nonlinearity (and hence $d\sigma/dE^2$) increases with increasing x. This apparant inconsistency is due to the $1/\sigma$ factor in (6.6); the conductivity decreases sharply with increasing x, and thus causes β to go through a minimum, which explains the smaller value attributed to the x=0.245 sample.

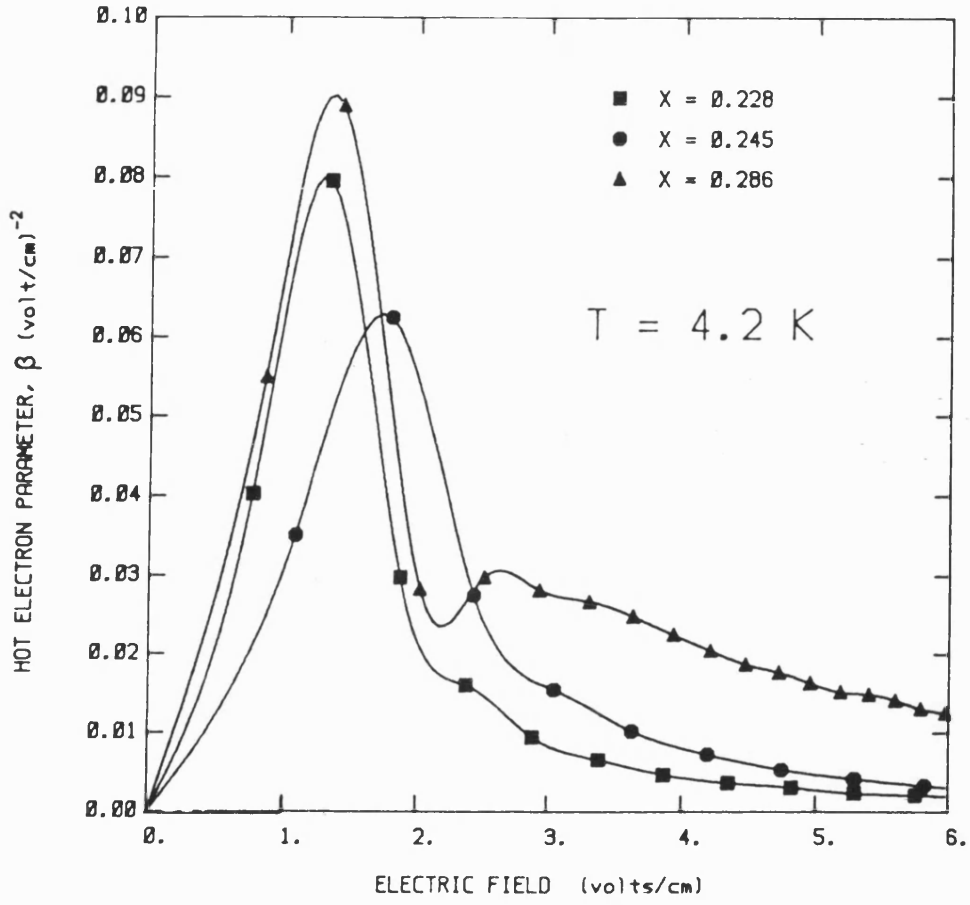

FIGURE 8.12

Hot electron (nonlinearity) parameter (β) as a function of electric field (E), for $Cd_xHg_{1-x}Te$, with x=0.228, 0.245 and 0.286, at T=4.2K. The points are interpolated using a cubic spline.

8.4.2 Voltage Responsivity and Time Response.

Once the values of β have been calculated, it is a simple step to obtain the voltage responsivity (R) as a function of electric field, using (6.17). Figures 8.13a-c show the curves of voltage responsivity as a function of E field for x=0.228, x=0.245 and x=0.286 respectfully. The peak responsivity in each case corresponds to the peak in the β-E graphs (figure 8.12), as expected from (6.17). If used as detectors, the samples would be biased to a voltage corresponding to the E field at which the responsivity is a maximum, and so it is this maximum that is of most interest. Both the x=0.228 and x=0.245 samples give maximum values of R that are comparable to n-InSb (219 and 286 $V.Watt^{-1}$ for x=0.228 and x=0.245 respectively, compared to 130 $V.Watt^{-1}$ for n-InSb). The x=0.286 sample, however, appears to have a responsivity that is several orders of magnetude greater; this is primarily due to the very large resistance of the sample, corresponding to a low conductivity which appears as part of the denominator in (6.17). This very low value of conductivity has severe repercussions on the use of this material as a detector, as will be shown later.

The results for the maximum responsivity are summarised in table 8.2, which also includes a calculated value of the response time (τ) at the bias field. The response time was obtained from (6.22), $d\mu/dT_e$ being approximated from figure 8.5. A typical value of τ for n-InSb is 0.17 μsec. Table 8.2 shows that even though the x=0.286 seems to have a very high responsivity, the response time is very much longer because of the low conductivity. Consequently it would be of no use as a fast detector.

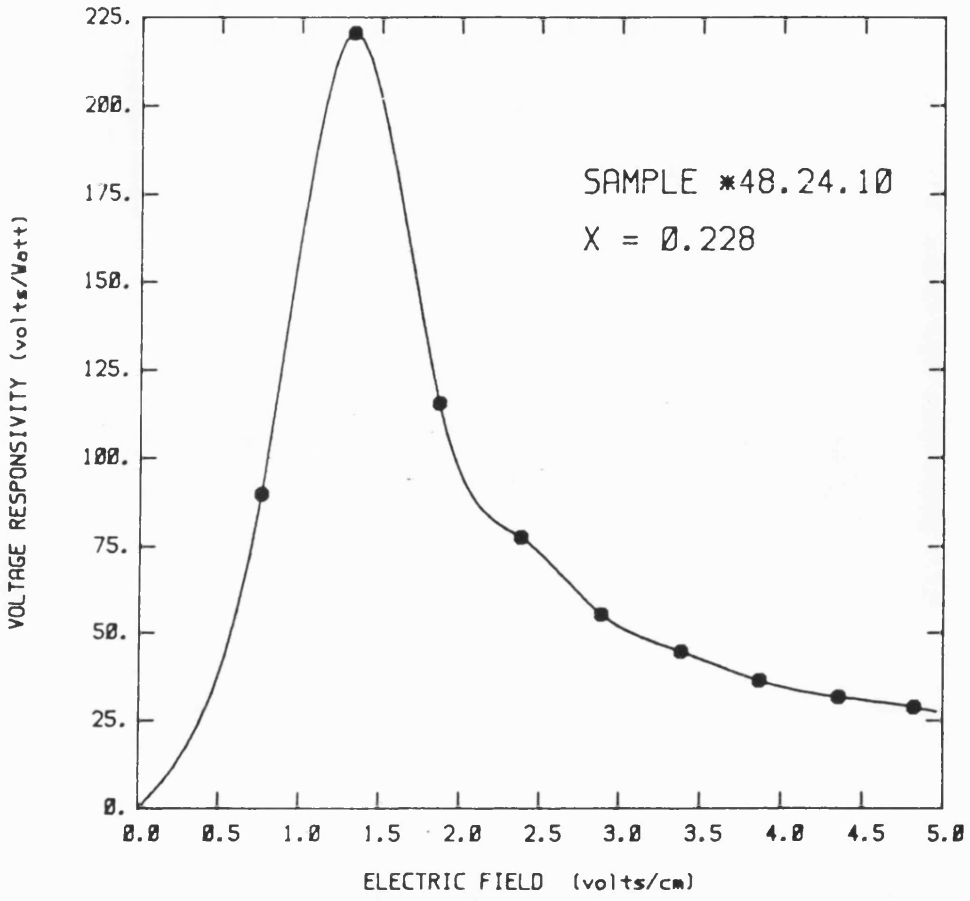
SAMPLE *48.24.10
X = 0.228
VOLTAGE RESPONSIVITY (volts/Watt)
ELECTRIC FIELD (volts/cm)
225.
200.
175.
150.
125.
100.
75.
50.
25.
0.
0.0
0.5
1.0
1.5
2.0
2.5
3.0
3.5
4.0
4.5
5.0

figure 8.13a

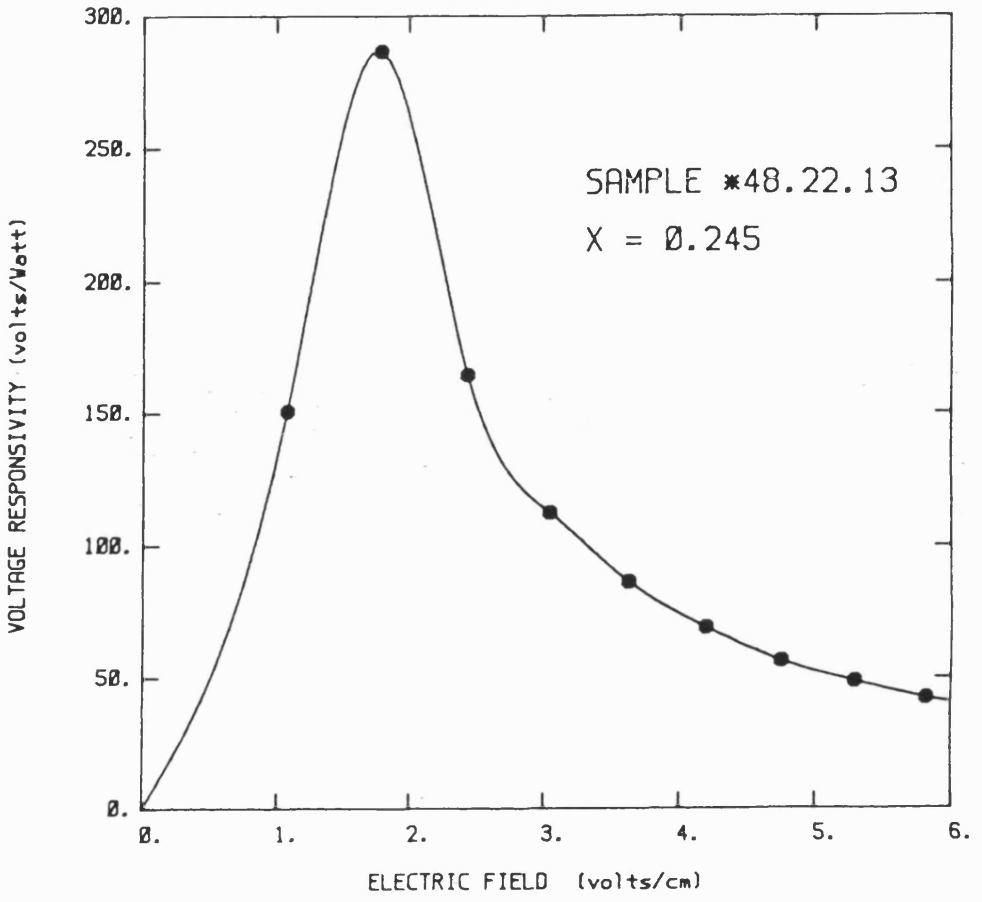
300.
250.
200.
150.
100.
50.
0.
VOLTAGE RESPONSIVITY (volts/Watt)
SAMPLE *48.22.13
X = 0.245
0.
1.
2.
3.
4.
5.
6.
ELECTRIC FIELD (volts/cm)

figure 8.13b

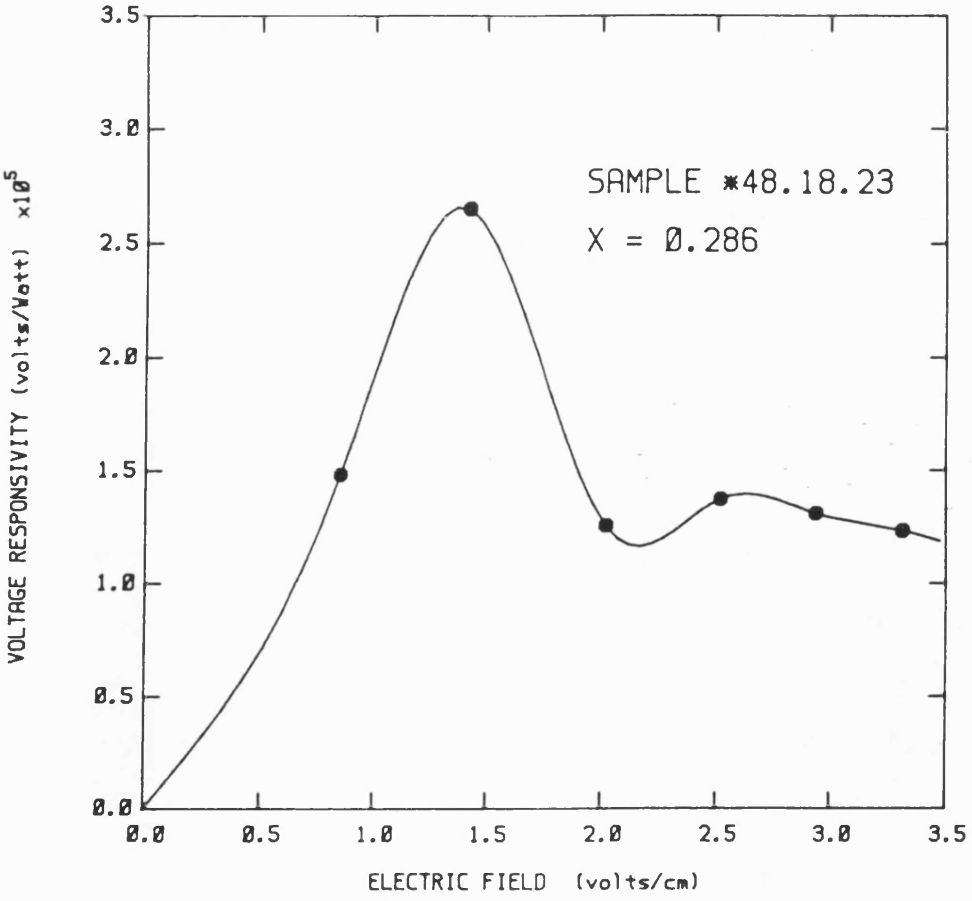

figure 8.13c

FIGURE 8.13a-c

Calculated voltage responsivity (R) as a function of electric field (E) for $Cd_xHg_{1-x}Te$, with (a) x=0.228, (b) x=0.245 and (c) x=0.286, at T=4.2K. The points are interpolated using a cubic spline.

TABLE 8.2

x value	0.228	0.245	0.286
Bias Voltage (V)	0.98	0.76	0.57
Bias Field ($V.cm^{-1}$)	1.33	1.79	1.36
Resistance (kΩ)	1.96	1.53	1.21 MΩ
σ ($\Omega^{-1}.cm^{-1}$)	0.24	0.036	5.8×10^{-4}
β ($cm^2.V^{-2}$)	0.08	0.04	0.10
R ($V.Watt^{-1}$)	219	286	2.66×10^5
τ (μS)	0.017	0.039	8.705

Calculated values of resistance, conductivity (σ), hot electron parameter (β), voltage responsivity (R) and response time (τ) for $Cd_xHg_{1-x}Te$, for x=0.228, 0.245 and 0.286 at T=4.2K. All values are calculated at the bias voltage which gives the maximum value of R.

Both the x=0.228 and x=0.245 samples on the other hand do show a marked reduction in response time, and hence may well have an increased bandwidth as compared to n-InSb when used as detectors.

One more problem exists in the use of the x=0.286 sample as a useful detector. Because of the very low conductivity, the fraction of the incident radiation absorbed by the electrons will be very small. In the classical limit, the free carrier absorption coefficient (α) is given by

$$\alpha = 4\pi\sigma/cK^{1/2} \qquad (8.2)$$

where c is the velocity of light, and K is the high frequency dielectric constant. Taking a value of K for the x=0.286 sample as 11.92 (Baars and Sorger 1972) gives $\alpha=2.4\times10^{-6}$ cm^{-1}, making the sample virtually transparent to the radiation. A similar calculation for the x=0.228 and x=0.245 samples gives $\alpha=9.6\times10^{-4}$ cm^{-1} and $\alpha=1.5\times10^{-4}$ cm^{-1} respectfully, whereas n-InSb has a value of $\alpha=0.3$ cm^{-1}. Thus n-InSb is far more absorbing than any of the three samples of CMT. The x=0.228 and x=0.245 samples, however, do have values of α which would allow them to be used as detectors, especially when the possibility of an increased bandwidth is taken into account.

8.5 SUMMARY AND FURTHER WORK.

Nonlinear (non-ohmic) electrical behaviour has been shown to occur in $Cd_xHg_{1-x}Te$ alloys at liquid helium temperatures for x values of 0.228, 0.245 and 0.286. The observed behaviour has indicated a positive deviation from Ohm's law, which is thought to be due to the electron mobility being limited by ionised impurity scattering. This hypothesis is successful in qualitatively explaining the observed trends in the degree of nonlinearity observed with increasing x value. A question has arisen, however, over the electron energy loss mechanism. Comparisons with InSb suggest that the dominat mechanism should be piezoelectric (acoustic phonon) scattering. A simple energy relaxation time approximation has evidenced that this is not the case in CMT. Further theoretical work is warranted here, and a modelling of the nonlinear effects using the same approach as Sladek (1960), who has obtained theoretical expressions for the deviation from Ohm's law in n-InSb, may prove useful.

Analysis of the I-V characteristics of the three samples has shown that they have potential application as detectors and heterodyne receivers for the sub-millimeter and far infrared wavelengths. Following the work of Kogan (1963) the voltage responsivity and time response have been calculated for all three samples at a temperature of 4.2K. The results agree with those of other workers (Weber and Kulpa 1980, 1982, Kimmit *et al* 1985), in that CMT may have a detectivity comparable to the normally used material, n-InSb, but with an increased bandwidth. The results presented here show that the dramatic

increase in responsivity gained with higher x value material may well be offset by a slower response time, and poorer absorbtion of the radiation. A closer examination of the I-V characteristics in the vicinity of the peak responsivity would be desirable in order to obtained more accurate values of R and τ, and the investigation of a greater number of different samples in the range $0.2<x<0.3$ would be useful in order to assertain more precisely how the responsivity and time response vary with x. The measurement of R and τ directly by the development of a cooled detector using CMT would be the eventual aim of any such research.

In order to produce an optimum working detector, or indeed to simple obtain a more definitive understanding of the nonlinear electrical effects in CMT, more fundamental experimental work is required. For example, the effects of sample preparation and contacts must be investigated. The main problem involved in such a program is the availability of consistent material, especially at the higher x values. Until bulk grown CMT with reproducible electrical characteristics is made available, it will be difficult to make any broad based study of nonlinear electrical effects in CMT alloys. Instead, the work would be limited to the investigation of single samples prepared from the same bulk grown material, as is the case reported here.

APPENDICES

APPENDIX I

NUMERICAL CALCULATION OF GRUNEISEN PARAMETERS.

In order to calculate both the mode Gruneisen parameters (equations 2.27-31) and the low and high temperature limit mean elastic Gruneisen parameters (equations 2.32,33), it is necessary to first obtain the three velocities (v) and the corresponding polarisations (U) for a given propagation direction N. This is done by finding the eigenvalues and eigenvectors respectively of Christoffels determinant (equation 3.5). For crystals having cubic symmetry, the components of Christoffels determinant (Γ_{ij}) are given by

$$\Gamma_{11} = N_1^2 C_{11} + N_2^2 C_{44} + N_3^2 C_{44}$$

$$\Gamma_{22} = N_1^2 C_{44} + N_2^2 C_{11} + N_3^2 C_{44}$$

$$\Gamma_{33} = N_1^2 C_{44} + N_2^2 C_{44} + N_3^2 C_{11}$$

$$\Gamma_{23} = \Gamma_{32} = N_2 N_3 (C_{12} + C_{44})$$

$$\Gamma_{13} = \Gamma_{31} = N_1 N_3 (C_{12} + C_{44})$$

$$\Gamma_{12} = \Gamma_{21} = N_1 N_2 (C_{12} + C_{44}) \qquad \text{(I.1)}$$

The direction cosines (N_i) of the propagation direction are given by (figure I.1)

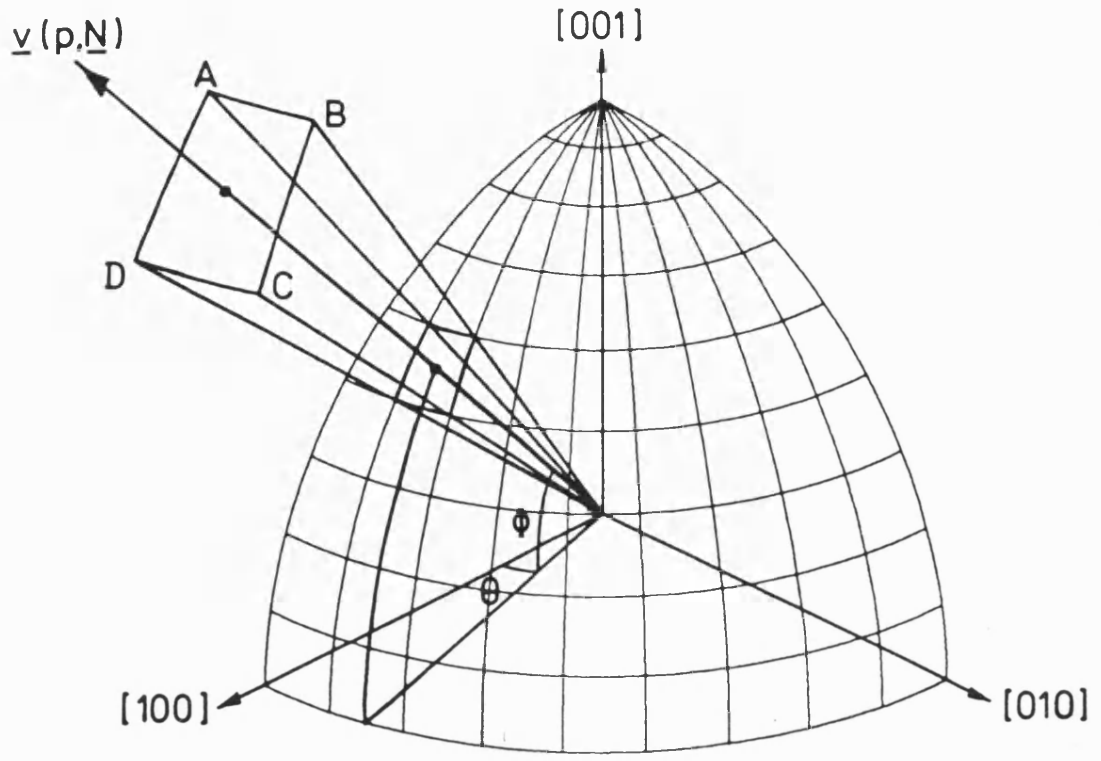

FIGURE I.1

Diagram showing the geometry of the numerical calculation of the mode and mean elastic Gruneisen parameters. Assuming a unit radius, the dimensions of trapezium ABCD are:

$$\underline{AB} = \Delta\theta\cos(\phi+\Delta\phi/2)$$

$$\underline{CD} = \Delta\theta\cos(\phi-\Delta\phi/2)$$

$$\underline{AD} = \underline{BC} = \Delta\phi$$

The spherical grid is marked out at equal angular increments $\Delta\theta$ and $\Delta\phi$.

$$N_1 = \sin(\phi)\cos(\theta)$$

$$N_2 = \sin(\phi)\sin(\theta)$$

$$N_3 = \cos(\phi) \qquad \text{(I.2)}$$

The eigenvalues and eigenvectors were found numerically by Jacobian reduction. Once the polarisation vectors (U_i) were obtained for a given propagation direction (N_i), the mode elastic Gruneisen parameters ($\gamma(p,N)$) could be calculated from equations 2.27-31. For the graphs of the mode Gruneisen parameters (figures 4.5, 5.3a-c), the first part of the angular scale on the abscissa (0-90) refers to a the variation in the angle ϕ, θ being held constant at 45°; this represents a rotation in a [110] type plane. The latter part of the scale (30-0) refers to the variation of θ, ϕ remaining constant at 90°. Hence this section of the graphs show the Gruneisen parameters in a four-fold plane ([001]).

Once the mode Gruneisen parameters have been calculated for any given direction N, it is a relatively simple step to calculate the mean elastic Gruneisen parameters. For this, the integrals in equations 2.32 and 2.33 are replaced by summations. Figure I.1 shows the geometry: assuming a unit radius to the sphere, the solid angle $\Delta\Omega$ can be approximated by the area of the trapezium ABCD. Hence

$$\Delta\Omega = \sqrt{\Delta\phi^2 - \Delta\theta^2 \sin^2(\phi)\sin^2(\Delta\phi/2)}\ .\Delta\theta\cos(\phi)\cos(\Delta\phi/2) \qquad \text{(I.3)}$$

where $\Delta\phi$ and $\Delta\theta$ are the angular steps depicted by the spherical grid in figure I.1. The summation was performed over half the octant shown in figure I.1 ($0<\theta<45°$, $0<\phi<90°$), with angular increments of 5°. Thus for each direction N, a new solid angle $\Delta\Omega$ was calculated. This method has the advantage of mapping out the surface of the sphere with the minimum of gaps, unlike previous methods, which chose values of $\Delta\phi$ and $\Delta\theta$ in order to keep the solid angle constant for each propagation direction. Reducing the angle step from 5° to 2.5° gave the same result to within three significant figures. Thus an angular step of 5° was considered sufficient to give the desired accuracy.

APPENDIX II

ESTIMATION OF THE EFFECT OF JOULE HEATING IN CMT SAMPLES AT 4.2K

For a given electric field across an arbitrary volume of material, the steady state temperature distribution T(r) within that volume is given by

$$\nabla^2 T(r) = - \frac{\sigma(T)E^2(r)}{k(T)} \quad , \qquad (II.1)$$

where $\sigma(T)$ is the electrical conductivity, E(r) the electric field and k(T) the thermal conductivity. Since both σ and k are functions of T, they will vary accordingly throughout the volume of the material.

In it's present form, equation (II.1) is impossible to solve analytically. In order to make some estimate of the Joule heating effect in the CMT samples used in the experiments described in chapter 7, several assumptions have to be made in order to simplify (II.1). The geometry of the sample is given in figure (II.1). In order to reduce the problem to one dimension, it is assumed that the only heat flow is in the x direction (i.e. the only heat loss is from the x=0 and x=a surfaces, see figure II.1); this assumption is justified by the fact that the sample thickness ($a \approx 300$-$400\mu m$) is much less than it's width or length (approximately 2mm and 5mm respectively).

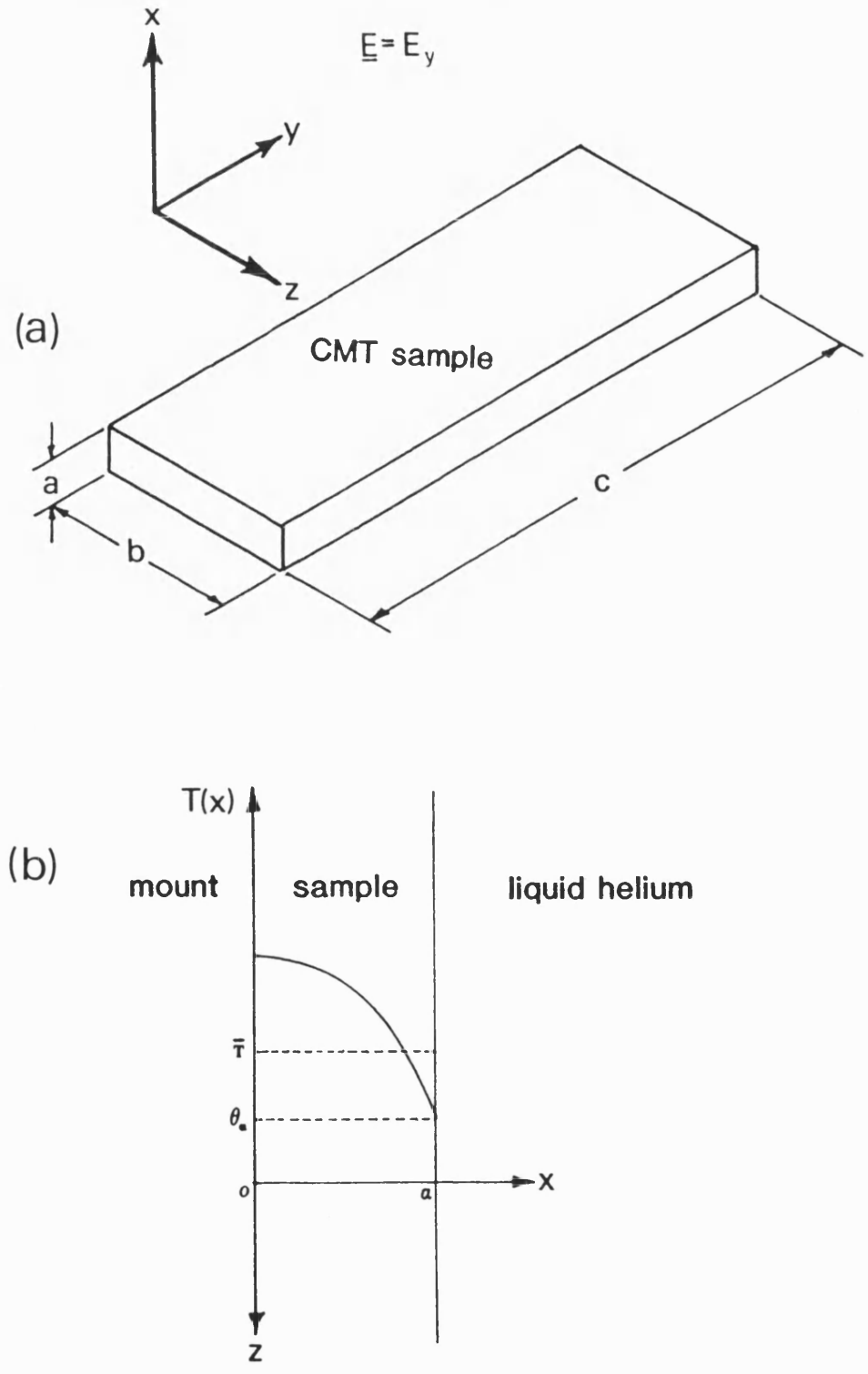

FIGURE II.1

Diagram showing (a) CMT sample dimensions and (b) Geometry of Joule heating calculation.

Hence equation (II.1) reduces to

$$\frac{d^2T(x)}{dx} = -\frac{\sigma(T)E^2}{k(T)} \quad . \qquad \text{(II.2)}$$

The electric field is assumed to be constant across the sample. Two further assumptions are now made; the surface at x=a (figure II.1) is assumed to be maintained at a fixed temperature θ_a, and the surface at x=0 is perfectly insulated by the sample mount (i.e. there is no heat flow across this surface). These assumptions lead to the following boundary conditions:

$$x = a, \quad T = \theta_a$$
$$x = 0, \quad dT/dx = 0 \quad . \qquad \text{(II.3)}$$

For a first approximation, the electrical and thermal conductivities are considered to be a constant across the sample at a value of $\sigma(\bar{T})$ and $k(\bar{T})$, where $\bar{T}$ is the average temperature given by

$$\bar{T} = \frac{1}{a}\int_0^a T(x)dx \quad . \qquad \text{(II.4)}$$

Equation (II.2) can now be written as

$$\frac{d^2T(x)}{dx} = -\frac{\sigma(\bar{T})E^2}{k(\bar{T})} = -G_o \quad , \qquad \text{(II.5)}$$

where G_o is a constant for a given electric field. Using the boundary conditions (II.3), the solution to (II.5) is given by

$$T(x) = \theta_a + \frac{G_o}{2}(a^2-x^2) \qquad \text{(II.6)}$$

The average temperature can now be calculated from (II.4);

$$\bar{T} = \theta_a + \frac{1}{3}G_o a^3$$

$$= \theta_a + \frac{1}{3}G(\bar{T})a^3 \quad . \qquad \text{(II.7)}$$

In order to calculate $\bar{T}$ self consistently from equation (II.7), it is necessary to know the form of G(T) ($=\sigma(T)E^2/k(T)$). Since the temperature of the samples is not likely to increase by more than a few degrees due to the Joule heating, the thermal conductivity is assumed to be constant ($k=k(\bar{T})$). The electrical conductivity is assumed to vary exponentially with temperature, i.e.

$$\sigma(T) = \sigma_o \exp(\alpha T) \qquad (II.8)$$

where α is a constant. Thus equation (II.7) becomes

$$T = \theta_a + \frac{1}{3}\left(\frac{\sigma_o E^2 a^3}{k}\right)\exp(\alpha T) \ . \qquad (II.9)$$

Taking the case of the x=0.286 sample, $\alpha \approx 0.4K^{-1}$, $\sigma_o \approx 10^{-5}\ \Omega^{-1}cm^{-1}$ and $a \approx 300\mu m$. Thus for moderate fields the factor $\sigma_o E^2 a^3$ is very small, and the exponential term in (II.9) can be ignored; the temperature across the sample is therefore constant at the x=a surface value, θ_a.

The main assumption in the model is that the surface at x=a is maintained at a fixed temperature θ_a. In the case of the sample being immersed in liquid helium (θ_a=4.2K), this is probably justified, and the fact that no Joule heating effects were observed at these temperatures supports this conclusion (see chapter 7). However, when the sample is at a higher temperature and cooled by helium gas, this assumption may become invalid. The surface temperature will be determined by the thermal conductivity of the gas, and may vary as the power input to the sample (σE^2) increases. The present model has shown that there is no temperature variation across the sample (and therefore no variation in electrical

conductivity or electric field). The Joule heating effects observed at T>8K are likely to be attributed to the sample heating up the surrounding gas, rather than any change in temperature within the sample itself. A more sophisticated approach, including the heat loss to the helium gas, is required in order to make an estimate of the increase in sample temperature due to Joule heating at temperatures higher than 4.2K.

APPENDIX III

PROGRAM UNITS FOR AUTOMATED I-V CHARACTERISTIC MEASUREMENT APPARATUS.

The following list contains the program units which run the low temperature I-V characteristic measurement system described in chapter 7. Each program unit will, depending on the program mode, 'chain' the next relevant program unit. All common parameters are dumped to disc before the next unit is loaded. Each program unit is written in standard BBC basic.

IVPROG1 Sets up display (figure 7.9).

IVPROG2 COMMAND MODE: allows the various operating parameters (program mode, plot mode, number of data points, current/voltage range etc.) to be altered. Sets up parameter stack on disc and initialises data file stems. Can be returned to at any time by pressing ESCAPE.

IVPROG3 MEASUREMENT MODE: makes a single measurement of an I-V characteristic. Current is increased upto the set range and then decreased to zero again. Current is then reversed to obtain the negative characteristic. Sample temperature is monitored throughout, and an average is taken at the end of the measurement cycle. If temperature varies more than ±0.2 K from initial value the measurement is aborted, and

an error message is output, either to STATUS section of display if IVPROG2 is returned to, or to the disc if a temperature run program mode is in operation. Values of voltage, current and thermocouple e.m.f. are stored as arrays and then dumped to a temporary file on disc before chaining the next program unit.

IVPROG4 TEMPERATURE SENSE MODE: continually monitors measured and desired temperatures (one measurement per second), and estimates the rate of change of temperature by retaining the last five readings, and fitting a least squares straight line to them. When the measured temperature equals the desired temperature, and the temperature drift is less than 0.2K/minute, the next program unit is chained.

IVPROG5 SAMPLE SWITCH: switches the sample relays in cyclic order 1,2,3,4.

IVPROG6 TEMPERATURE INCREMENT: increments the set temperature parameter by predefined amount, and adjusts temperature controller accordingly.

IVDUMP DATA FILE GENERATOR: loads characterisitc from temporary file generated by IVPROG3, and generates file name of the form

D.S{mount_number}/{sample_number}/{file_number}

File number for that particular sample number is then incremented. Program also searches disc

data base for sample identification and compositional x value, which is also dumped to the new file, along with the average temperature and the characteristic. When called, the program outputs the date, time, measurement temperature and file name to the printer.

IVPLOT I-V PLOT PROGRAM: this unit is only called when PLOT MODE is set to 1. It displays the I-V characteristic (figure 7.10), and generates a file name as in IVDUMP. Program then waits for user command (screen dump, save data to present file name, modify present file name, continue with no further action). This program unit cannot be called when a continuous temperature run mode is in operation.

The above program units are for the CURRENT CONTROLLED CONFIGURATION, i.e. the current is adjusted and the sample voltage measured. For the VOLTAGE CONTROLLED MODE, there are a similar set of programs with the prefix VI (e.g. VIPROG3). An initial BOOT file asks the operator which configuration is being used, and then chains the relevant start up unit. In the case of pulsed measurements, only the CURRENT CONTROLLED MODE can be used.

REFERENCES

REFERENCES

ARENBERG D.L., 1950, J. Appl. Phys. 21, 941.

BAARS J. and SORGER F., 1972, Solid State Commun., 10, 875.

BARDEEN J. and SHOCKLEY W., 1950, Phys. Rev., 80, 72.

BARRON T.H.K., COLLINS J.G. and WHITE G.K., 1980, Adv. Phys. 29, 609.

BASHKIN I.O., and PERESADA G.I., 1974, Fiz. Tverd. Tela, 16, 3166.

BERLINCOURT D., JAFFE H. and SHIOZAWA, L.R., 1963, Phys. Rev., 129, 1009.

BORG I.Y. and SMITH D.K., 1967, J. Phys. Chem. Solids, 28, 49.

BOYLE W.F. and SLADEK R.J., 1975, Phys. Rev. B, 11, 2933.

BROWDER J.S. and BALLARD S.S., 1969, Appl. Optics, 8, 793

BRASSINGTON M, 1982, PhD thesis, University of Bath.

BROOKS H., 1955, Phys. Rev., 83, 879.

BRUESCH P., 1982, *Phonons: Theory and Experiment*, (Springer, Berlin).

BRUGGER K., 1964, Phys. Rev., 133, A1611.

BRUGGER K., 1965a, J. Appl. Phys., 36, 768.

BRUGGER K., 1965b, Phys. Rev. A, 137, 1826.

BRUGGER K. and FRITZ T.C., 1967, Phys. Rev., 157, 524.

CASHMAN R.J., 1959, Proc. Inst. Radio Eng., 47, 1471.

CHATTOPADHYAY D., 1981, Phys. Letters, 81A, No.4, 241.

CHATTOPADHYAY D. and NAG B.R., 1975, Phys. Rev., B12, 5676.

COCHRAN W., 1964, Phys. Letters, 13, 193.

CONWELL E. and WEISSKOPF V.F., 1950, Phys. Rev., 77, 388.

COTTAM R.I. and SAUNDERS G.A., 1973, J. Phys. C: Solid State Phys., 6, 2105.

COTTAM R.I. and SAUNDERS G.A., 1975, J. Phys. Chem. Solids, 36, 187.

CRONIN N.J., 1977, PhD Thesis, Queen Mary College, University of London.

DEMEREST H.H., OTA R. and ANDERSON, O.L., 1977, *High pressure research applications in Geophysics*, ed. by M.H. Manghani and S.I. Akimoto (Academic Press, New York), 281.

DORHAUS R. and NIMTZ G., 1976, in *Tracks in Modern Physics*, 78, (Springer-Verlag, Berlin), 1.

DRABBLE J.R. and BRAMMER A.J., 1967, Proc. Phys. Soc., 91, 959.

ENDERS P., 1983, Phys. Stat. Sol. (b), 120, 735.

ENDERS P., 1984a, Phys. Stat. Sol. (b), 121, 39.

ENDERS P., 1984b, Phys. Stat. Sol. (b), 121, 461.

FINKMAN E. and NEMIROVSKY Y., 1979, J. Appl. Phys., 50, 4356.

FORD P.J., MILLER A.J., SAUNDERS G.A., YOGURTCU Y.K., FURDYNA J.K., JACZYNSKI M., 1982, J. Phys. C: Solid State Phys., 15, 657.

GERLICH D., 1973, *Proc. 6th Symp. of Thermophysical Properties*, Atlanta, 305.

GREENOUGH R.D. and PALMER S.B., 1973, J. Phys. D: Appl. Phys., 6, 587.

HANSON G.L., SCHMIT J.L. and CASSELMAN T.N., 1982, J. Appl. Phys, 53, 7099.

HESS K., 1980, in *Physics of Nonlinear Transport in Semiconductors*, ed. by D. Ferry, J. Barker and C. Jacoboni (Plenum Press, New York and London), 1.

HOLDER J., 1970, J. Rev. Sci. Instrum. 41, 1355.

HOUSTON B., STRAKNA R.E. and BELSON H.S., 1968, J. Appl. Phys., 39, 3913.

HUNTINGDON H.B., 1947, Phys. Rev. 72, 321.

KANE E.O., 1966, in *Semiconductors and Semimetals*, 1, (Academic Press, New York).

KAWAMURA H., 1980, *Lecture notes in Physics*, 133, 470.

KEATING P.N., 1966a, Phys. Rev., 149, 674.

KEATING P.N., 1966b, Phys. Rev., 152, 774.

KIMMIT M.F., LOPEZ G.C., GILES J.C., TAKAI M., ROSER H.P., MCgUCKIN B.T. and BLACK A., 1985, Infrared Phys., 25, No.6, 767.

KOGAN S.M., 1963a, Sov. Phys. Solid state, 4, 1813.

KOGAN S.M., 1963b, Sov. Phys. Solid State, 4, 1386.

KRASILMIKOV O.M., VEKILOV Y.K., BEZBORODOVA V.M. and YUSHIN A.U., 1970, Fiz. Teh. Poluprovdn., 4, 2122.

KUMAZAKI K., 1975, Phys. Status Solidi a, 29, k55.

KUSAKOV V.I., RUSAKOV A.P. and MENSTER A.N., 1972, Fiz. Tverd. Tela., 14, 2161.

KUSHAWA M.S. and KUSHAWA S.S., 1980, Can. J. Phys., 58, 351.

LANDAU L.D. and LIFSHITZ E.M., 1970, *Theory of Elasticity*, (Pergamon Press, Oxford).

LEE B.H., 1970a, J. Appl. Phys., 41, 2984.

LEE B.H., 1970b, J. Appl. Phys., 41, 2988.

LEHOCZKY A., NELSON D.A. and WHITSETT C.R., 1969, Phys. Rev., 188, 1069.

LEIBFRIED G. and LUDWIG W., 1961, Solid State Phys., 12, 275.

LIFSHITS T.M., KOGAN S.M., VYSTAVKIN A.N. and MEL'NIK P.G., 1962, Sov. Phys. JETP, 15, 661.

LIPPMANN G., KASTNER P. and WANNINGER W., 1981, J. Phys. C., 14, 1569.

LITTLEWOOD P.B., 1980, J. Phys. C., 13, 4855.

MARTIN R.M., 1970, Phys. Rev. B, 1, 4005.

MASON W.P. and McSKIMIN H.J., 1947, J. Acoust. Soc. Am. 19, 464.

MAY J.R., 1958, IRE Nat. Conv. Rec., 6, 134.

MILLER A.J., SAUNDERS G.A., YOGURTCU Y.K. and ABEY A.E., 1981a, Phil. Mag., 43, 1447.

MILLER A.J., SAUNDERS G.A. and YOGURTCU Y.K., 1981b, J.Phys. C., 14, 1569.

MITCHEL D.L., PALIK E.D. and ZEMEL J.N., 1964, in *Physics of Semiconductors Seventh International Conference, Paris*, ed. by M. Hulin, (Academic Press, New York), 325.

MOSS T.S., 1961, in *Proceedings of the International Conference on Photoconductivity*, Ithaca, USA.

MOSS T.S., BURRELL G.J. and ELLIS B., 1973, in *Semiconductor Optioelectronics*, (Butterworths, London), 178.

MURNAGHAN F.D., 1951, *Finite Deformation of an Elastic Solid*, (Dover publications, Inc., New York).

MUSGRAVE M.J.P, 1970, *Crystal Acoustics*, (Holden-Day, San-francisco, Cambridge, London, Amsterdam).

McSKIMIN H.J., 1953, J. Appl. Phys., 24, 988

McSKIMIN H.J., 1961, J. Acoust. Soc. Am. 33, 12.

McSKIMIN H.J., 1965, J. Acoust. Soc. Am. 37, 864.

McSKIMIN H.J. and ANDREATCH P., 1963, J. Appl. Phys., 34, 651.

McSKIMIN H.J. and ANDREATCH P., 1964, J. Appl. Phys., 35, 3312.

McSKIMIN H.J. and ANDREATCH P., 1965, J. Acoust. Soc. Am. 41, 1053.

McSKIMIN H.J. and ANDREATCH P., 1967, J. Appl. Phys., 38, 2610.

McSKIMIN H.J. and ANDREATCH P., 1972, J. Appl. Phys., 43, 2944.

McSKIMIN H.J. and THOMAS D.G., 1962, J. Appl. Phys, 33, 56.

McSKIMIN H.J., JAYARAMAN A. and ANDREATCH P., 1967, J. Appl. Phys., 38, 2362.

McSKIMIN H.J., JAYARAMAN A., ANDREATCH P. and BATEMAN T.B., 1968, J. Appl. Phys., 39, 4127.

NAKAMSHI A. and MATSUBARA T., 1980, Proc. Theor. Phys. (Kyoto), 63, 1.

NIMTZ G., BAUER G., DORNHAUS R. and MULLER K.H., 1974, Phys. Rev., B10, 3302.

NOVIKOVA S.I., 1961, Sov. Phys. -Solid St., 2, 2087.

NYE J.F., 1957, *Physical Properties of Crystals*, (Clarendon Press, Oxford).

OVERHOF H., 1971, Phys. Stat. Solidi, B45, 315.

PAPADAKIS E.P., 1964, J. Appl. Phys., 35, 1474.

PAPADAKIS E.P., 1966, J. Acoust. Soc. Am. 40, 863.

PAPADAKIS E.P., 1967, J. Acoust. Soc. Am. 42, 1045.

PAWLEY G.S., COCHRAN R.A., Cowley R.A and Dolling G., 1966, Phys. Rev. Lett., 17, 735.

PERESADA G.I., PONYATOVSKII E.G. and SOKOLOVSKAYA Zh.D., 1976, Phys. Stat. Sol. (a), 35, K177.

PHILLIPS J.C., 1973, *Bonds and Bands in Semiconductors*, (Academic Press, New York).

PUTLEY E.H., 1966, in *Semiconductors and Semimetals*, vol.1, chap.3. (Academic Press, New York).

RABII S., 1968, Phys. Rev., 167, 801.

RAMAI D.S. and SLADEK R.J., 1979, Solid State Commun., 30, 591.

RODERICK R.L. and TRUELL R., 1952, J. Appl. Phys., 23, 267.

ROLLIN B.V., 1961, Proc. Phys. Soc., 77, No.5, 1102.

RUSAKOV A.P., VEKILOV Y.K. and KADYSHEVICH A.E., 1971, Sov. Phys -Solid St., 12, 2618.

RYDER E.J., 1953, Phys. Rev., 90, 766.

SAMARA G.A. and DRICKAMER H.G., 1962, J. Phys. Chem. Solids, 23, 457.

SCOTT M.W., 1969, J. Appl. Phys., **40**, 4077.

SCOTT M.W., 1972, J. Appl. Phys., **43**, 6055.

SEEGER K., 1982, *Semiconductor Physics*, (Springer, New York).

SEDDON T., FARLEY J.M. and SAUNDERS G.A., 1975, Sol. Stat. Commun., 17, 55.

SLADEK R.J., 1960, Phys. Rev., **120**, No.5, 1589.

SLUTSKY L.J. and GARLAND C.W., 1959, Phys. Rev., **113**, 167.

SMITH T.F., BIRCH J.A. and COLLINS J.G., 1976, J. Phys. C., 9, 4375.

STANKEIWICZ J. AND GIRIAT W., 1972, J. Appl. Phys., **B49**, 397.

SUGAI S., MURASE K., KATAYAMA S., TAKAOKA S., NISHI S. and KAWAMURA H., 1977, Sol. Stat. Commun., 24, 407.

THAKUR K.P., 1980, J. Phys. Chem. Solids, 41, 465.

THURSTON R.N., 1964, in *Physical Acoustics*, vol. 1A, ed. by Mason (Academic Press, New York).

THURSTON R.N., 1965, Proc. IEEE., **53**, 1320.

THURSTON R.N. and BRUGGER K., 1964, Phys. Rev., **133**, A1604.

TRUELL R., ELBAUM C. and CHICK B.B., 1969, *Ultrasonic Methods in Solid State Physics*, (Academic Press, New York).

TRUESDELL C. and TOUPIN R.A., 1960, in *Handbuch der Physik*, vol III/I, ed. by S. Flugge, 226, (Springer, Berlin).

VEKILOV Y.K. and RUSAKOV A.P., 1971, Sov. Phys. -Solid St., 13, 956.

WEBER B.A. and KULPA S.M., 1980, Jap. J. Appl. Phys., **19**, 345.

WEBER B.A. and KULPA S.M., 1982, Int. J. Infrared Millimetre Waves, 3, 235.

WILLARDSON R.K and BEER A.C., (1981), *Semiconductors and Semimetals*, 18, (Academic Press, New York).

YOGURTCU Y.K., 1980, PhD thesis, University of Bath.

YOGURTCU Y.K., LAMBSON E.F., MILLER A.J. and SAUNDERS G.A., 1980, Ultrasonics 18, 155.

YOGURTCU Y.K., MILLER A.J. and SAUNDERS G.A., 1981, J. Phys. Chem. Solids, 42, 49.

ZANIO K., 1978, *Semiconductors and Semimetals*, 13, (Academic Press, New York).

ZIMAN J.M., 1962, *Electrons and Phonons*, (Clarendon Press, Oxford).